Available online at www.sciencedirect.com
ScienceDirect
Comput. Methods Appl. Mech. Engrg. 384 (2021) 113998
Computer methods in applied mechanics and engineering
www.elsevier.com/locate/cma

Optimal local truncation error method for solution of wave and heat equations for heterogeneous materials with irregular interfaces and unfitted Cartesian meshes

A. Idesman[a,*], B. Dey[b]

[a] *Department of Mechanical Engineering, Texas Tech University, Lubbock, TX 79409-1021, USA*
[b] *Department of Mechanical Engineering, University of Utah, Salt Lake City, UT 84112, USA*

Received 13 March 2021; received in revised form 28 May 2021; accepted 9 June 2021
Available online xxxx

Abstract

Recently we have developed the optimal local truncation error method (OLTEM) for PDEs with constant coefficients on irregular domains and unfitted Cartesian meshes. However, many important engineering applications include domains with different material properties (e.g., different inclusions, multi-material structural components, etc.) for which this technique cannot be directly applied. In the paper OLTEM is extended to a much more general case of PDEs with discontinuous coefficients and can treat the above-mentioned applications. We show the development of OLTEM for the 1-D and 2-D scalar wave equation as well as the heat equation using compact 3-point (in the 1-D case) and 9-point (in the 2-D case) stencils that are similar to those for linear quadrilateral finite elements. Trivial unfitted Cartesian meshes are used for OLTEM with complex interfaces between different materials. The interface conditions on the interfaces where the jumps in material properties occur are added to the expression for the local truncation error and do not change the width of the stencils. The calculation of the unknown stencil coefficients is based on the minimization of the local truncation error of the stencil equations and yields the optimal order of accuracy of the new technique at a given width of stencil equations. In contrast to the second order of accuracy for linear finite elements, OLTEM provides the fourth order of accuracy in the 1-D case and in the 2-D case for horizontal interfaces as well as the third order of accuracy for the general geometry of smooth interfaces. The numerical results for the domains with complex smooth interfaces show that at the same number of degrees of freedom, OLTEM is even much more accurate than quadratic finite elements and yields the results close to those for cubic finite elements with much wider stencils. The wave and heat equations are uniformly treated with OLTEM. OLTEM can be directly applied to other partial differential equations.

Keywords: Wave and heat equations with discontinuous coefficients; Local truncation error; Irregular interfaces; Cartesian meshes; Optimal accuracy

1. Introduction

The finite element method, the finite volume method, the isogeometric elements, the spectral elements and similar techniques represent very powerful tools for the solution of partial differential equations (PDEs) for a complex

* Corresponding author.
E-mail address: alexander.idesman@ttu.edu (A. Idesman).

https://doi.org/10.1016/j.cma.2021.113998

geometry. However, the generation of non-uniform meshes for a complex geometry is not simple and may lead to the decrease in accuracy of these techniques if 'bad' elements (e.g., elements with small angles) appear in the mesh. Moreover, the conventional derivation of discrete equations for these techniques (e.g., based on the Galerkin approaches) does not lead to the optimal accuracy. For example, it has been shown in many publications on wave propagation that at the same width of the stencil equations of a semi-discrete system for regular rectangular domains with uniform meshes, the accuracy of conventional linear finite elements can be improved from order two to order four (e.g., see [1–8] and others), the accuracy of conventional high-order finite and isogeometric elements in the L^2 norm can be improved from order $2p$ to order $2p+2$ (e.g., see [9–13]) where p is the element order. These improvements are based on the use of the averaged mass matrix or on the use of the special locations of the integration points for the calculation of the elemental mass and stiffness matrices. However, the increase in accuracy of these techniques is limited to the wave equation with constant coefficients, zero loading term and rectangular domains. Moreover, the increase in the order of accuracy for the high-order elements in [9–13] is not optimal. In [14–16] the order of accuracy of the high-order elements on rectangular domains has been improved to $4p$ and this order is optimal at a given width of stencil equations. We should also mention different techniques based on the discontinuous Galerkin method that also improve the accuracy of numerical solutions; e.g., see [17–22] and many others.

There is a significant number of publications related to the numerical solution of different PDEs on irregular domains with uniform embedded meshes. For example, we can mention the following fictitious domain numerical methods that use uniform embedded meshes: the embedded finite difference method, the cut finite element method, the finite cell method, the Cartesian grid method, the immersed interface method, the virtual boundary method, the embedded boundary method, etc. The main objective of these techniques is to simplify the mesh generation for irregular domains as well as to mitigate the effect of 'bad' elements. For example, the techniques based of the finite element formulations (such as the cut finite element method, the finite cell method, the virtual boundary method and others) yield the $p+1$ order of accuracy in the L^2 norm even with small cut cells generated due to complex irregular boundaries (e.g., see [23–29] and many others). The main advantage of the embedded boundary method developed in [30–34] is the use of simple Cartesian meshes. The boundary conditions or fluxes in this technique are interpolated using the Cartesian grid points and this leads to the increase in the stencil width for the grid points located close to the boundary (the numerical techniques developed in [30–34] provide just the second order of accuracy for the global solution). A stable generalized finite element method for the Poisson equation was developed in [35] for heterogeneous materials with curved interfaces and unfitted uniform meshes (the uniform meshes are not matched with curved interfaces). The second order of accuracy in the energy norm (that includes partial derivatives) was achieved in [35] with 2-D quadratic finite elements that form 25-point stencils.

The development of robust numerical techniques for the solution of PDEs on irregular domains that provide an optimal and high order of accuracy is still a challenging problem. Recently in our papers [36–41] we have developed a new numerical technique for the solution of PDEs with constant coefficients on regular and irregular domains with Cartesian meshes. We called this approach the optimal local truncation error method. At the same structure of the semidiscrete or discrete equations, OLTEM provides the optimal order of accuracy that exceeds the order of accuracy of many known numerical approaches on regular and irregular domains. Here, we extend it to a much more general case of PDEs with discontinuous coefficients that have numerous engineering applications; e.g., the modeling of composite materials, wave propagation and heat transfer in heterogeneous materials and many others. The focus of this paper is the development of compact high-order stencils affected by irregular interfaces between different materials (these stencils can be used for regular and irregular domains).

Section 2 introduces the wave and heat equations for heterogeneous materials and the local truncation error. In Section 3, OLTEM with 3-point stencils is uniformly derived for the 1-D wave and heat equations with discontinuous coefficients. Its extension to the 2-D case for uniform and non-uniform 9-point stencils with horizontal and complex interfaces is considered in Section 4. 1-D and 2-D numerical examples with horizontal interfaces and the general geometry of interfaces as well as the comparison with FEM are presented in Section 5. The approach developed in the paper reduces PDEs to ODEs. Any known time-integration method can be used for the time integration of ODEs. For the derivation of many analytical expressions presented below we use the computational program "Mathematica".

2. The wave and heat equations for heterogeneous materials and the local truncation error

Wave propagation in a composite domain $\Omega = \cup\Omega_l$ ($l = 1, 2, \ldots, \bar{N}$ where $\bar{N}$ is the total number of subdomains) is described by the following scalar wave equation in each subdomain Ω_l:

$$\frac{\partial^2 u_l}{\partial t^2} - c_l^2 \nabla^2 u_l = f_l \,. \tag{1}$$

Similarly, the heat equation in each subdomain Ω_l can be written as:

$$\frac{\partial u_l}{\partial t} - a_l \nabla^2 u_l = f_l \,. \tag{2}$$

For each subdomain Ω_l we use the following notations in Eqs. (1)–(2): c_l is the wave velocity, a_l is the thermal diffusivity, $f_l(\boldsymbol{x}, t)$ is the loading or source term, u_l is the field variable. Eqs. (1)–(2) can be uniformly written down in subdomain Ω_l as:

$$\frac{\partial^n u_l}{\partial t^n} - \bar{c}_l \nabla^2 u_l = f_l \,, \tag{3}$$

where $n = 2$ and $\bar{c}_l = c_l^2$ for the wave equation and $n = 1$ and $\bar{c}_l = a_l$ for the heat equation. We also assume that the functions u_l and f_l are sufficiently smooth in each subdomain Ω_l. At the smooth interface G (G a point in the 1-D case and a curve in the 2-D case) between any two subdomains, the following interface conditions (the continuity of the function and the flux across the interface; e.g., see [42–44]) are applied:

$$u_G^* = u_G^{**} \,, \qquad e_*(n_x \frac{\partial u_G^*}{\partial x} + n_y \frac{\partial u_G^*}{\partial y}) = e_{**}(n_x \frac{\partial u_G^{**}}{\partial x} + n_y \frac{\partial u_G^{**}}{\partial y}) \,, \tag{4}$$

where n_x and n_y are the x and y-components of the normal vector at the interface, e is the corresponding material constant, the symbols $*$ and $**$ correspond to the quantities on the opposite sides from the interface for the corresponding subdomains Ω_l. This means that the functions u_l are continuous across the interfaces but can have the discontinuous spatial derivatives across the interfaces. The functions f_l can be discontinuous across the interfaces.

Remark 1. The second condition in Eq. (4) for the flux continuity corresponds to isotropic materials with one material parameter for the flux calculation (e.g., e_* and e_{**} are the thermal conductivity coefficients on opposite sides from the interface in the case of the heat equation). However, the approach considered in the paper can be also extended to anisotropic materials with the modified second condition in Eq. (4) (e.g., for the heat equation, the thermal conductivity tensors should be used for the flux calculation instead of material parameters e_* and e_{**}).

Remark 2. Numerical examples (e.g., Section 5.2 for the impact problem) show that the numerical approach developed in the paper can be also applied to the problems with reduced regularity (smoothness) of the functions u_l.

In this paper the Dirichlet boundary conditions $u = g_1$ are applied along the boundary Γ. However, the Neumann boundary conditions can be also used with the proposed approach; e.g., see our papers [41,45]. The initial conditions are $u_l(\boldsymbol{x}, t = 0) = g_2$, $v_l(\boldsymbol{x}, t = 0) = g_3$ in Ω_l for the wave equation and $u_l(\boldsymbol{x}, t = 0) = g_4$ in Ω_l for the heat equation where g_i ($i = 1, 2, 3, 4$) are the given functions and $l = 1, 2, \ldots, \bar{N}$. According to OLTEM, the semidiscrete system for the wave and heat equations after the space discretization with a Cartesian rectangular mesh can be represented as a system of ordinary differential equations in time. The ordinary differential equation of this system for each internal grid point of the domain is called the stencil equation and can be written down as follows:

$$\sum_{i=1}^{M} [h^2 m_i \frac{d^n u_i^{num}}{dt^n} + k_i u_i^{num}] = \bar{f} \,, \tag{5}$$

where u_i^{num} and $\frac{d^n u_i^{num}}{dt^n}$ are the numerical solution for function u and its time derivative at the grid points, m_i and k_i are the unknown stencil coefficients to be determined, $\bar{f}(t)$ is the discretized loading (source) term (see the next Sections), M is the number of the grid points included into the stencil equation, $n = 2$ for the wave equation and $n = 1$ for the heat equation, h is the mesh size along the x-axis. Many numerical techniques such as the finite difference method, the finite element method, the finite volume method, the isogeometric elements, the spectral

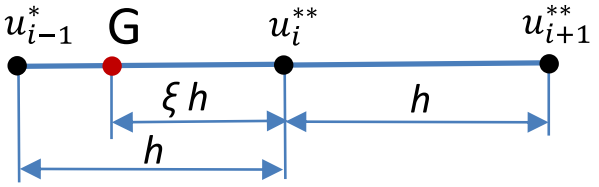

Fig. 1. The spatial locations of the degrees of freedom u^*_{i-1}, u^{**}_i, u^{**}_{i+1} $(i = 2, 3, 4, \ldots)$ and the interface G between two materials for the 3-point stencil.

elements, different meshless methods and others can be finally reduced to Eq. (5) with some specific coefficients m_i and k_i for the wave and heat equations. In the derivations below, we will assume 3-point stencils ($M = 3$) in the 1-D case and 9-point stencils ($M = 9$) in the 2-D case that are similar to the 3-point and 9-point stencils of the 1-D and 2-D linear quadrilateral finite elements on Cartesian meshes. Generally, the stencils with any number of points M can be used with the suggested approach. We should also mention that the stencil width can be used for the approximate estimation of computational costs because numerical techniques with similar stencils require approximately the same computational costs.

Let us introduce the local truncation error used with OLTEM. The replacement of the numerical values of function u_i^{num} and its time derivatives $\frac{d^n u_i^{num}}{dt^n}$ at the grid points in Eq. (5) by the exact solution u_i and $\frac{d^n u_i}{dt^n}$ to the wave or heat equation, Eq. (1) or (2), leads to the residual e of this equation called the local truncation error of the semidiscrete equation, Eq. (5):

$$e \,=\, \sum_{i=1}^{M} [h^2 m_i \frac{d^n u_i}{dt^n} + k_i u_i] - \bar{f}\,. \tag{6}$$

Calculating the difference between Eqs. (5) and (6) we can get

$$e \,=\, \sum_{i=1}^{M} \{h^2 m_i [\frac{d^n u_i}{dt^n} - \frac{d^n u_i^{num}}{dt^n}] + k_i [u_i - u_i^{num}]\} \,=\, \sum_{i=1}^{M} [h^2 m_i \bar{e}_i^v + k_i \bar{e}_i^u]\,, \tag{7}$$

where $\bar{e}_i^u = u_i - u_i^{num}$ and $\bar{e}_i^v = \frac{d^n u_i}{dt^n} - \frac{d^n u_i^{num}}{dt^n}$ are the errors of function u and its time derivatives at the grid points i. As can be seen from Eq. (7), the local truncation error e is a linear combination of the errors of the function u_i and its time derivatives at the grid points i which are included into the stencil equation.

3. OLTEM for the 1-D wave and heat equations with discontinuous coefficients (with zero loading (source) term $f_l = 0$ in Eqs. (1) and (2))

For OLTEM in the 1-D case, we consider a uniform mesh with 3-point stencils (similar to those for linear finite elements). We assume that the mesh is sufficiently fine in order to include only one interface between different materials within any 3-point stencil; see Fig. 1. The case of the 3-point stencil inside the homogeneous material follows from this stencil when point G coincides with the end point $i - 1$ of the 3-point stencil; see Fig. 1 for $\xi = 1$. The coordinates x_{i-1} and x_{i+1} of the points $i - 1$ and $i + 1$ of the 3-point stencil and the coordinate x_G of the interface point G are (see Fig. 1):

$$x_{i+1} \,=\, x_i + h\,, \qquad x_{i-1} \,=\, x_i - h\,, \qquad x_G \,=\, x_i - \xi h\,, \tag{8}$$

where $0 \le \xi \le 1$. For the exact solution, the interface conditions at the interface point G can be written down as follows:

$$u^*_G \,=\, u^{**}_G\,, \qquad e_* \frac{\partial u^*_G}{\partial x} \,=\, e_{**} \frac{\partial u^{**}_G}{\partial x}\,, \tag{9}$$

where symbols $*$ and $**$ correspond to different materials from the left and right sides of the interface point G (of course, the domain under consideration can include any number of different materials).

For the 3-point stencil in Fig. 1, the stencil equation Eq. (5) can be explicitly rewritten as follows:

$$h^2 (m_1 \frac{d^n u^{*,num}_{i-1}}{dt^n} + m_2 \frac{d^n u^{**,num}_i}{dt^n} + m_3 \frac{d^n u^{**,num}_{i+1}}{dt^n}) + (k_1 u^{*,num}_{i-1} + k_2 u^{**,num}_i + k_3 u^{**,num}_{i+1}) \,=\, 0\,, \tag{10}$$

where the case of zero loading $f_l = \bar{f} = 0$ is considered, $i = 2, \dots, N-1$ (N is the total number of the grid points), $n = 2$ for the wave equation and $n = 1$ for the heat equation, the coefficients m_j and k_j ($j = 1, 2, 3$) are to be determined from the minimization of the local truncation error, the index l related to subdomain Ω_l is replaced by the corresponding symbol $*$ or $**$. For convenience, we use the local numeration of the stencil coefficients k_j, m_j with $j = 1, 2, 3$ instead of the global numeration with $j = i-1, i, i+1$.

Remark 3. Only 5 out of the 6 coefficients m_i, k_i ($i = 1, 2, 3$) in Eq. (10) can be considered as unknown coefficients. This can be explained as follows. Eq. (10) can be rescaled by the division of the left- and right-hand sides of Eq. (10) by any scalar; i.e., one of the stencil coefficients can be selected as unity and there will be only 5 unknown rescaled coefficients. For convenience, we will scale the stencil coefficients in such a way that the coefficient k_2 is $k_2 = 1$.

Remark 4. Conventional linear finite elements used for the wave (heat) equation have the stencil given by Eq. (10) with the stencils coefficients m_i, k_i ($i = 1, 2, 3$) calculated in terms of the elemental mass and stiffness matrices.

The local truncation error e follows from Eq. (10) by the replacement of the numerical solution $u_{i-1}^{*,num}$, $u_i^{**,num}$ and $u_{i+1}^{**,num}$ by the exact solution u_{i-1}^{*}, u_i^{**} and u_{i+1}^{**}:

$$e = h^2(m_1\frac{d^n u_{i-1}^{*}}{dt^n} + m_2\frac{d^n u_{i}^{**}}{dt^n} + m_3\frac{d^n u_{i+1}^{**}}{dt^n}) + (k_1 u_{i-1}^{*} + k_2 u_i^{**} + k_3 u_{i+1}^{**}). \tag{11}$$

One of the ideas of the new approach is to include the interface conditions for the exact solution in the expression for the local truncation error (Eq. (11)):

$$\begin{aligned} e &= h^2(m_1\frac{d^n u_{i-1}^{*}}{dt^n} + m_2\frac{d^n u_{i}^{**}}{dt^n} + m_3\frac{d^n u_{i+1}^{**}}{dt^n}) + (k_1 u_{i-1}^{*} + k_2 u_i^{**} + k_3 u_{i+1}^{**}) \\ &+[q_1(u_G^{*} - u_G^{**}) + hq_2(e_*\frac{\partial u_G^{*}}{\partial x} - e_{**}\frac{\partial u_G^{**}}{\partial x}) + h^2 q_3(\frac{\partial^n u_G^{*}}{\partial t^n} - \frac{\partial^n u_G^{**}}{\partial t^n}) + h^3 q_4(e_*\frac{\partial^{n+1} u_G^{*}}{\partial t^n \partial x} - e_{**}\frac{\partial^{n+1} u_G^{**}}{\partial t^n \partial x}) \\ &+ h^4 q_5(\frac{\partial^{2n} u_G^{*}}{\partial t^{2n}} - \frac{\partial^{2n} u_G^{**}}{\partial t^{2n}})], \end{aligned} \tag{12}$$

where the coefficients q_i ($i = 1, 2, \dots, 5$) will be used for the minimization of the local truncation error in Eq. (12), the expressions in parenthesis after q_1 and q_2 are the interface conditions, Eq. (9), the expressions in parenthesis after q_3, q_4 and q_5 are the time derivative of the interface conditions (the time derivative of the left- and right-hand sides of Eq. (9)). Therefore, the expression in the square brackets in Eq. (12) is zero and Eqs. (11) and (12) yield the same local truncation error e.

To derive the coefficients m_i and k_i ($i = 1, 2, 3$) in Eq. (12), let us expand the exact solution u_i at the grid points $i-1$, i and $i+1$ into a Taylor series in the vicinity of the interface point G at small $h \ll 1$ as follows (see Fig. 1 for the locations of u_i and u_G):

$$v_{i-1}^{*} = v_G^{*} - \frac{\partial v_G^{*}}{\partial x}(1-\xi)h + \frac{\partial^2 v_G^{*}}{\partial x^2}\frac{((1-\xi)h)^2}{2!} - \frac{\partial^3 v_G^{*}}{\partial x^3}\frac{((1-\xi)h)^3}{3!} + \frac{\partial^4 v_G^{*}}{\partial x^4}\frac{((1-\xi)h)^4}{4!} - \cdots, \tag{13}$$

$$v_{i}^{**} = v_G^{**} + \frac{\partial v_G^{**}}{\partial x}(\xi h) + \frac{\partial^2 v_G^{**}}{\partial x^2}\frac{(\xi h)^2}{2!} + \frac{\partial^3 v_G^{**}}{\partial x^3}\frac{(\xi h)^3}{3!} + \frac{\partial^4 v_G^{**}}{\partial x^4}\frac{(\xi h)^4}{4!} + \cdots, \tag{14}$$

$$v_{i+1}^{**} = v_G^{**} + \frac{\partial v_G^{**}}{\partial x}(1+\xi)h + \frac{\partial^2 v_G^{**}}{\partial x^2}\frac{((1+\xi)h)^2}{2!} + \frac{\partial^3 v_G^{**}}{\partial x^3}\frac{((1+\xi)h)^3}{3!} + \frac{\partial^4 v_G^{**}}{\partial x^4}\frac{((1+\xi)h)^4}{4!} + \cdots, \tag{15}$$

where the function v in Eqs. (13)–(15) is u and $\frac{\partial^n u}{\partial t^n}$.

The exact solution to Eq. (3) also meets the following equations at point G:

$$\frac{\partial^n u_G^{*}}{\partial t^n} = \bar{c}_*\frac{\partial^2 u_G^{*}}{\partial x^2}, \qquad \frac{\partial^n u_G^{**}}{\partial t^n} = \bar{c}_{**}\frac{\partial^2 u_G^{**}}{\partial x^2}, \tag{16}$$

$$\frac{\partial^{j+ln} u_G^{*}}{\partial x^j \partial t^{ln}} = \bar{c}_*\frac{\partial^{j+2+(l-1)n} u_G^{*}}{\partial x^{j+2}\partial t^{(l-1)n}}, \qquad \frac{\partial^{j+ln} u_G^{**}}{\partial x^j \partial t^{ln}} = \bar{c}_{**}\frac{\partial^{j+2+(l-1)n} u_G^{**}}{\partial x^{j+2}\partial t^{(l-1)n}} \tag{17}$$

where the case of zero loading (source) term $f^{*} = f^{**} = 0$ is considered, $l = 1, 2$ and $j = 1, 2, 3, 4, \dots$. Eq. (17) is obtained by the differentiation of Eq. (16) with respect to x^j and t^n. Inserting Eqs. (13)–(17) into Eq. (12) we

get the following local truncation error in space for OLTEM:

$$e = b_1 u_G^* + b_2 u_G^{**} + h[b_3 \frac{\partial u_G^*}{\partial x} + b_4 \frac{\partial u_G^{**}}{\partial x}] + h^2[b_5 \frac{\partial^2 u_G^*}{\partial x^2} + b_6 \frac{\partial^2 u_G^{**}}{\partial x^2}] + h^3[b_7 \frac{\partial^3 u_G^*}{\partial x^3} + b_8 \frac{\partial^3 u_G^{**}}{\partial x^3}]$$
$$+h^4[b_9 \frac{\partial^4 u_G^*}{\partial x^4} + b_{10} \frac{\partial^4 u_G^{**}}{\partial x^4}] + h^5[b_{11} \frac{\partial^5 u_G^*}{\partial x^5} + b_{12} \frac{\partial^5 u_G^{**}}{\partial x^5}] + h^6[b_{13} \frac{\partial^6 u_G^*}{\partial x^6} + b_{14} \frac{\partial^6 u_G^{**}}{\partial x^6}] + O\left(h^7\right), \tag{18}$$

where the coefficients b_p ($p = 1, 2, \ldots$) are expressed in terms of the coefficients m_l, k_l, q_j ($l = 1, 2, 3$ and $j = 1, 2, \ldots, 5$) and the distance ξ; see Appendix A. We should mention that by the use of the wave (heat) equation, Eqs. (16)–(17), the time derivatives for the local truncation error in Eq. (18) are excluded. In order to minimize the order of the local truncation error, we will zero the first 10 coefficients $b_p = 0$ ($p = 1, 2, \ldots, 10$) for the smallest power of h. From these 10 algebraic equations and the condition $k_2 = 1$ (see Remark 3 after Eq. (10)) we can find the 11 coefficients m_l, k_l, q_j ($l = 1, 2, 3$ and $j = 1, 2, \ldots, 5$):

$$m_1 = \frac{e_*(\bar{c}_*^2(e_*\xi(\xi^3+2\xi^2-1)+e_{**}(-4\xi^4-2\xi^3+6\xi^2+\xi-1))+2\bar{c}_*\bar{c}_{**}(\xi-1)^2(3e_*\xi(\xi+1)+e_{**}(-2\xi^2+\xi+1))+\bar{c}_{**}^2e_*(\xi-1)^4)}{12\bar{c}_*\bar{c}_{**}(e_*\xi+e_*-e_{**}\xi+e_{**})(\bar{c}_*e_*\xi(\xi+1)+\bar{c}_*e_{**}(-2\xi^2+\xi+1)+\bar{c}_{**}e_*(\xi-1)^2)},$$
$$m_2 = \frac{1}{12\bar{c}_*\bar{c}_{**}(e_*\xi+e_*-e_{**}\xi+e_{**})(\bar{c}_*e_*\xi(\xi+1)+\bar{c}_*e_{**}(-2\xi^2+\xi+1)+\bar{c}_{**}e_*(\xi-1)^2)}[\bar{c}_*^2(e_*^2\xi(\xi+1)^2(\xi^2+3\xi+1)$$
$$+e_*e_{**}(-5\xi^5-15\xi^4-4\xi^3+14\xi^2+9\xi+1)+e_{**}^2(8\xi^3+24\xi^2+20\xi+5)(\xi-1)^2)-2\bar{c}_*\bar{c}_{**}e_*(\xi-1)^2(e_{**}(5\xi^3+5\xi^2-6\xi-4)$$
$$-e_*\xi(\xi^2+3\xi+2))+\bar{c}_{**}^2e_*(\xi-1)^4(5e_*(\xi+1)+e_{**}(-\xi)+e_{**})],$$
$$m_3 = -\frac{1}{12\bar{c}_*\bar{c}_{**}(e_*\xi+e_*-e_{**}\xi+e_{**})(\bar{c}_*e_*\xi(\xi+1)+\bar{c}_*e_{**}(-2\xi^2+\xi+1)+\bar{c}_{**}e_*(\xi-1)^2)}[(\bar{c}_*^2(e_*^2\xi^2(\xi^3-2\xi-1)$$
$$+e_*e_{**}\xi(-5\xi^4+5\xi^3+6\xi^2-4\xi-2)+e_{**}^2(8\xi^3-4\xi-1)(\xi-1)^2)+2\bar{c}_*\bar{c}_{**}e_*(\xi-1)^3(e_*(\xi+1)\xi-5e_{**}\xi^2+e_{**})$$
$$+\bar{c}_{**}^2e_*(\xi-1)^4(5e_*\xi+e_{**}(-\xi)+e_{**}))],$$
$$k_1 = -\frac{e_*}{e_*\xi+e_*-e_{**}\xi+e_{**}}, \qquad k_2 = 1, \qquad k_3 = -\frac{(e_*\xi+e_{**}(-\xi)+e_{**})}{e_*\xi+e_*-e_{**}\xi+e_{**}}, \tag{19}$$

Here we show the stencil coefficients m_l and k_l ($l = 1, 2, 3$) only because the coefficients q_j ($j = 1, 2, \ldots, 5$) are not used in the global system of equations.

Inserting the coefficients m_i and k_i ($i = 1, 2, 3$) for OLTEM (see Eq. (19)) into Eq. (18) we get the following local truncation error:

$$e = \frac{h^5}{xx}[(\xi-1)(\bar{c}_*e_*\frac{\partial^5 u_G^*}{\partial x^5}(-5\bar{c}_*^2(\xi-1)^2(e_{**}(4\xi^4+2\xi^3-6\xi^2-\xi+1)-e_*\xi(\xi^3+2\xi^2-1))-\bar{c}_*\bar{c}_{**}(\xi-1)^4(7e_{**}(2\xi^2-\xi-1)$$
$$-27e_*\xi(\xi+1))+2\bar{c}_{**}^2e_*(\xi-1)^6)-\bar{c}_{**}\frac{\partial^5 u_G^{**}}{\partial x^5}(\bar{c}_*^2(e_*^2\xi^2(\xi+1)^2(2\xi^2+5\xi+2)+e_*e_{**}\xi(-14\xi^5-42\xi^4-25\xi^3+20\xi^2+21\xi+4)$$
$$+e_{**}^2(30\xi^6+45\xi^5-35\xi^4-55\xi^3+\xi^2+12\xi+2))+\bar{c}_*\bar{c}_{**}e_*(e_*\xi(12\xi^5+18\xi^4-20\xi^3-25\xi^2+8\xi+7)$$
$$+e_{**}(-65\xi^6+145\xi^4-15\xi^3-73\xi^2+\xi+7))+5\bar{c}_{**}^2e_*(\xi-1)^3(5e_*\xi(2\xi^2+3\xi+1)+e_{**}(-3\xi^3+2\xi+1))))]$$
$$+\frac{h^6}{4xx}[(\bar{c}_{**}\frac{\partial^6 u_G^{**}}{\partial x^6}(\bar{c}_*^2(e_*^2\xi^2(3\xi^6+8\xi^5-10\xi^3+8\xi+3)+2e_*e_{**}\xi(-12\xi^7-16\xi^6+28\xi^5+25\xi^4-25\xi^3-12\xi^2+9\xi+3)$$
$$+e_{**}^2(56\xi^6+108\xi^5-60\xi^3+16\xi+3)(\xi-1)^2)+4\bar{c}_*\bar{c}_{**}e_*(\xi-1)^2(e_*\xi(7\xi^5+15\xi^4-10\xi^2+2)$$
$$+e_{**}(-37\xi^6-23\xi^5+60\xi^4+20\xi^3-20\xi^2-2\xi+2))+5\bar{c}_{**}^2e_*(\xi-1)^4(5e_*\xi(5\xi^3+6\xi^2-1)$$
$$+e_{**}(-8\xi^4+2\xi^3+6\xi^2+\xi-1)))-\bar{c}_*e_*\frac{\partial^6 u_G^*}{\partial x^6}(-5\bar{c}_*^2(3\xi+1)(\xi-1)^3(e_{**}(4\xi^4+2\xi^3-6\xi^2-\xi+1)-e_*\xi(\xi^3+2\xi^2-1))$$
$$+4\bar{c}_*\bar{c}_{**}(\xi-1)^5(e_*\xi(20\xi^2+27\xi+7)+e_{**}(-10\xi^3+\xi^2+7\xi+2))+\bar{c}_{**}^2e_*(5\xi+3)(\xi-1)^7))]+O(h^7) \tag{20}$$
$$with$$
$$xx = 360\bar{c}_*\bar{c}_{**}(e_*\xi+e_*-e_{**}\xi+e_{**})(\bar{c}_*e_*\xi(\xi+1)+\bar{c}_*e_{**}(-2\xi^2+\xi+1)+\bar{c}_{**}e_*(\xi-1)^2).$$

In case of a homogeneous material with $\xi = 1$, the following stencil coefficients m_l and k_l ($l = 1, 2, 3$) and the local truncation error e_{homog} follow from Eqs. (19) and (20):

$$m_1 = \frac{1}{24c_{**}}, \qquad m_2 = \frac{5}{12c_{**}}, \qquad m_3 = \frac{1}{24c_{**}}, \qquad k_1 = -\frac{1}{2}, \qquad k_2 = 1, \qquad k_3 = -\frac{1}{2} \tag{21}$$

and

$$e_{homog} = \frac{h^6}{480}\frac{\partial^6 u_G^{**}}{\partial x^6} + O(h^8). \tag{22}$$

The global semidiscrete system of equations includes the 3-point stencils for homogeneous materials inside each subdomain Ω_l with the stencil coefficients given by Eq. (21) and the sixth order of the local truncation error (see Eq. (22)) as well as the 3-point stencils intersected by the interface (with the stencil coefficients given by Eq. (19)) that provide the fifth order of the local truncation error (see Eq. (20)). This global semidiscrete system provides the 4th order of accuracy of the entire numerical solution at mesh refinement; see the numerical examples below.

Remark 5. In order to simplify the explanation of the idea of the imposition of the interface conditions for OLTEM, in this section we have considered a uniform stencil shown in Fig. 1. A more general case of non-uniform stencils for the grid points close to irregular boundary is considered in the next section for the 2-D case (see also the treatment of 1-D non-uniform stencils for homogeneous materials in our paper [36]).

4. OLTEM for the 2-D wave and heat equations with discontinuous coefficients

In this section we first introduce the local truncation error for 9-point stencils with the interface conditions in the 2-D case. Then, we derive OLTEM with 9-point stencils for heterogeneous materials in the case of zero load (source) term. Finally, we take into account nonzero load (source) term.

4.1. Zero load (source) term $f_l = 0$ in Eqs. (1) and (2)

Here, we extend OLTEM described in the previous Section for the 1-D case to the 2-D case. In contrast to the 1-D case, the interface between different materials in the 2-D case is a curve and the interface conditions also include the components of the unit normal to the interface; see Eq. (4). Let us consider a 2-D bounded domain and a Cartesian rectangular mesh with a mesh size h where h is the size of the mesh along the x-axis, $b_y h$ is the size of the mesh along the y-axis (b_y is the aspect ratio of the mesh). Similar to OLTEM for a homogeneous material (see [36–38]), 9-point uniform stencils are used for the internal grid points located far from the boundary and 9-point non-uniform stencils are used for the grid points located close to the boundary in the 2-D case. The 9-point stencil considered here is similar to that for 2-D linear quadrilateral finite elements. The spatial locations of the 8 degrees of freedom that are close to the internal degree of freedom u_5 and contribute to the 9-point stencil for this degree of freedom are shown in Fig. 2a for the case when the boundary and the Cartesian mesh are matched or when the degree of freedom u_5 is located far from the boundary. In the case of non-matching grids when the grid points do not coincide with the boundary, the neighboring grid points for the internal grid point u_5 that are located outside the physical domain are moved to the boundary of the physical domain as shown in Fig. 2b. In order to find the boundary points that are included into the stencil for the degree of freedom u_5 (see Fig. 2b) we join the central point u_5 with the 8 closest grid points; i.e., we have eight straight lines along the $x-$ and $y-$axes and along the diagonal directions (the dashed lines) of the grid; see Fig. 2b. If any of these lines intersects the boundary of the domain then the corresponding grid point (designated as $\circ$) should be moved to the boundary (the new location is designated as $\bullet$). This means that for all internal points located within the domain we use a 9-point uniform (see Fig. 2a) or non-uniform (see Fig. 2b) stencil. For convenience, the local numeration of the grid points from 1 to 9 is used in Figs. 2a and 2b as well as in the derivations below for the 9-point uniform and non-uniform stencils.

The interface in Fig. 3a divides the 9-point uniform stencil into two parts with different material properties. In order to impose the interface condition at the interface, first we select one point at the interface with the coordinates $x_G = x_{G,3}$ and $y_G = y_{G,3}$. This point can be selected as follows. We join the central point u_5 with the 8 closest grid points; i.e., we have eight straight lines along the $x-$ and $y-$axes and along the diagonal directions of the grid; see Fig. 3a. If several these straight lines intersect the interface then we select the intersection point closest to the grid points u_5. Then, for the procedure described below, we select four additional points at the interface located at the same distances $\bar{h} = \sqrt{(x_{G,i+1} - x_{G,i})^2 + (y_{G,i+1} - y_{G,i})^2}$ $(i = 1, 2, 3, 4)$ from each other (the numerical experiments show that small distances $\bar{h} = h/10$ yield accurate results). In the case of the intersection of the 9-point non-uniform stencil in Fig. 2b by the interface, the selection of five points on the interface for the 9-point non-uniform stencil in Fig. 2b is similar to that for the uniform stencil in Fig. 3a.

To describe the coordinates of the boundary points for non-uniform stencils (see Fig. 2b) we introduce 9 coefficients $0 \le d_p \le 1$ $(p = 1, 2, \ldots, 9)$ as follows:

$$x_p = x_5 + (i-2)d_p h\,, \qquad y_p = y_5 + (j-2)d_p b_y h\,, \tag{23}$$

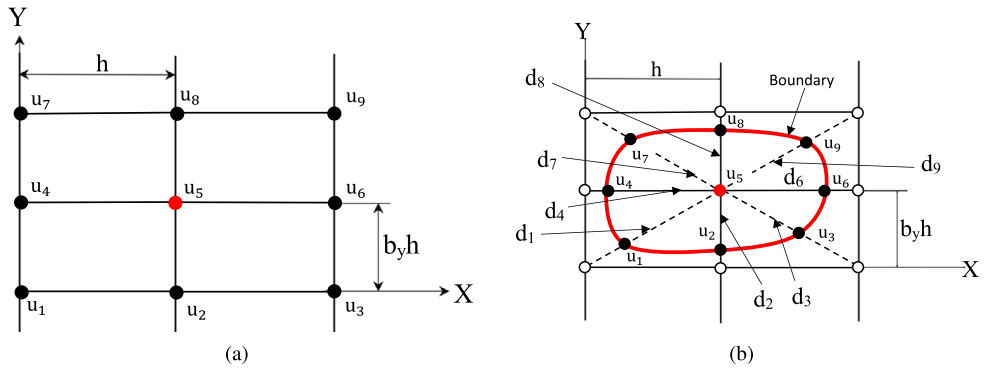

Fig. 2. The spatial locations of the degrees of freedom u_p $(p = 1, 2, \ldots, 9)$ that contribute to the 9-point uniform (a) and nonuniform (b) stencils for the internal degree of freedom u_5.

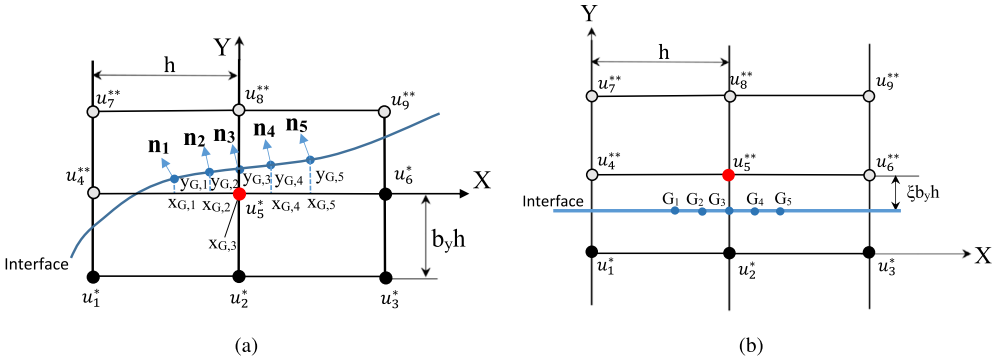

Fig. 3. The spatial locations of the degrees of freedom u_p $(p = 1, 2, \ldots, 9)$ and the five interface points G_i $(i = 1, 2, \ldots, 5)$ on the general (a) and horizontal (b) interface that contribute to the 9-point uniform stencils for the internal degree of freedom u_5.

where $d_5 = 0$, $p = 3(j-1)+i$ with $i, j = 1, 2, 3$. Eq. (23) can be also used for the coordinates of the grid points inside the domain with the corresponding coefficients d_p equal to unity ($d_p = 1$).

To describe the coordinates of the five points on the interface (see Fig. 3a) we introduce 10 coefficients $d_{x,p}$ and $d_{y,p}$ $(p = 1, 2, \ldots, 5)$ as follows (see also Fig. 3a):

$$x_{G,j} = x_G + d_{x,j}h\,, \qquad y_{G,j} = y_G + d_{y,j}b_y h\,, \qquad j = 1, 2, \ldots, 5\,, \tag{24}$$

where $d_{x,3} = d_{y,3} = 0$ for the central interface point $G = G_3$ with the coordinates $x_G = x_{G,3}$ and $y_G = y_{G,3}$; see Fig. 3.

Remark 6. Some of the four interface points G_1, G_2, G_4, G_5 can be located slightly outside the 9-point cell. The derivations presented below are also valid for this case.

Eq. (5) for the 9-point stencils for the grid point u_5 (see Fig. 2, Fig. 3) will be assumed in the following form:

$$h^2 \sum_{p=1}^{9} m_p[a_p \frac{d^n u_p^{*,num}}{dt^n} + (1-a_p)]\frac{d^n u_p^{**,num}}{dt^n} + \sum_{p=1}^{9} k_p[a_p u_p^{*,num} + (1-a_p)u_p^{**,num}] = \bar{f}_5\,, \tag{25}$$

where $\bar{f}_5 = 0$ in the case of zero load (source) $f_l = 0$ in Eqs. (1) and (2), the 18 unknown stencil coefficients m_p, k_p $(p = 1, 2, \ldots, 9)$ are to be determined from the minimization of the local truncation error, the coefficients $a_p = 1$ if point u_p belongs to material $*$ and $a_p = 0$ if point u_p belongs to another material $**$ (i.e., only one variable $u_p^{*,num}$ or $u_p^{**,num}$ is included into Eq. (25) for each grid point; see Fig. 3a with $a_1 = a_2 = a_3 = a_5 = a_6 = 1$ and $a_4 = a_7 = a_8 = a_9 = 0$), the superscript n in the time derivative in Eq. (25) is $n = 1$ for the heat equation

and $n = 2$ for the wave equation. The local truncation error e follows from Eq. (25) by the replacement of the numerical solution $u_p^{*,num}$ and $u_p^{**,num}$ by the exact solution u_p^* and u_p^{**}:

$$e = h^2 \sum_{p=1}^{9} m_p[a_p \frac{d^n u_p^*}{dt^n} + (1-a_p)\frac{d^n u_p^{**}}{dt^n}] + \sum_{p=1}^{9} k_p[a_p u_p^* + (1-a_p)u_p^{**}] - \bar{f}_5\,. \tag{26}$$

One of the ideas of the new approach is to include the interface conditions for the exact solution in the expression for the local truncation error in Eq. (26) as follows:

$$\begin{aligned} e = {} & h^2 \sum_{p=1}^{9} m_p[a_p \frac{d^n u_p^*}{dt^n} + (1-a_p)\frac{d^n u_p^{**}}{dt^n}] + \sum_{p=1}^{9} k_p[a_p u_p^* + (1-a_p)u_p^{**}] + \{\sum_{j=1}^{5} q_{1,j}(u_{G,j}^* - u_{G,j}^{**}) \\ & + \sum_{j=1}^{5} h q_{2,j}[e_*(n_{x,j}\frac{\partial u_{G,j}^*}{\partial x} + n_{y,j}\frac{\partial u_{G,j}^*}{\partial y}) - e_{**}(n_{x,j}\frac{\partial u_{G,j}^{**}}{\partial x} + n_{y,j}\frac{\partial u_{G,j}^{**}}{\partial y})] + \sum_{j=2}^{4} h^2 q_{3,j}(\frac{\partial^n u_{G,j}^*}{\partial t^n} - \frac{\partial^n u_{G,j}^{**}}{\partial t^n}) \\ & + h^3 q_4[e_*(n_{x,3}\frac{\partial^{n+1} u_{G,3}^*}{\partial t^n \partial x} + n_{y,3}\frac{\partial^{n+1} u_{G,3}^*}{\partial t^n \partial y}) - e_{**}(n_{x,3}\frac{\partial^{n+1} u_{G,3}^{**}}{\partial t^n \partial x} + n_{y,3}\frac{\partial^{n+1} u_{G,3}^{**}}{\partial t^n \partial y})] + h^4 q_5(\frac{\partial^{2n} u_{G,3}^*}{\partial t^{2n}} - \frac{\partial^{2n} u_{G,3}^{**}}{\partial t^{2n}})\} - \bar{f}_5\,, \end{aligned} \tag{27}$$

where $n_{x,j}$ and $n_{y,j}$ are the x and y-components of the normal vectors at the five selected interface points (see Fig. 3a), the coefficients $q_{1,i}$, $q_{2,i}$, $q_{3,j}$, q_4 and q_5 ($i = 1, 2, \ldots, 5$, $j = 2, 3, 4$) will be used for the minimization of the local truncation error in Eq. (27), the expressions in parenthesis after $q_{1,j}$ and $q_{2,j}$ are the interface conditions at the five selected interface points, Eq. (9), the expressions in parenthesis after $q_{3,j}$, q_4 and q_5 are the time derivative of the interface conditions (similar to those in the previous Section 3 for the 1-D case). Therefore, the expression in the curled brackets in Eq. (27) is zero and Eqs. (26) and (27) yield the same local truncation error e. The expression in the curled brackets in Eq. (27) is the generalization of the interface conditions in Eq. (12) for the 1-D case to the 2-D case when the interface is a curve. The addition of the interface conditions at five points in Eq. (27) with the coefficients $q_{1,j}$, $q_{2,j}$, $q_{3,i}$, q_4 and q_5 allows us to obtain the analytical expressions for the stencil coefficients for the horizontal interface as well as to get a high accuracy for general geometry of interfaces; see below.

Remark 7. Only 32 out of the 33 coefficients m_p, k_p, $q_{1,j}$, $q_{2,j}$, $q_{3,i}$, q_4 and q_5 ($p = 1, 2, \ldots, 9$, $i = 2, 3, 4$, $j = 1, 2, 3, 4, 5$) in Eq. (27) can be considered as unknown coefficients. This can be explained as follows. In the case of zero load (source) term $f_l = 0$ and $\bar{f}_5 = 0$, Eq. (27) can be rescaled by the division of the left- and right-hand sides of Eq. (27) by any scalar; i.e., one of the coefficients can be selected as unity and there will be only 32 unknown rescaled coefficients. The case of nonzero load (source) term $\bar{f}_5 \neq 0$ can be similarly treated because the term $\bar{f}_5$ is a linear function of the stencil coefficients; see below. For convenience, we will scale the stencil coefficients in such a way that k_5 is $k_5 = 1$.

In order to represent the local truncation error e as a Taylor series, let us expand the exact solution at the grid points and the five selected interface points in Eq. (27) into a Taylor series in the vicinity of the central interface point $G = G_3$ with the coordinates $x_G = x_{G,3}$ and $y_G = y_{G,3}$ (see Fig. 3) at small $h \ll 1$ as follows:

$$\begin{aligned} v_p = {} & v_G + \frac{\partial v_G}{\partial x}[((i-2)d_p - dx_G)h] + \frac{\partial v_G}{\partial y}[((l-2)d_p - dy_G)b_y h] + \frac{\partial^2 v_G}{\partial x^2}\frac{[((i-2)d_p - dx_G)h]^2}{2!} \\ & + \frac{\partial^2 v_G}{\partial y^2}\frac{[((l-2)d_p - dy_G)b_y h]^2}{2!} + 2\frac{\partial^2 v_G}{\partial x \partial y}\frac{[((i-2)d_p - dx_G)h][((l-2)d_p - dy_G)b_y h]}{2!} + \cdots\,, \end{aligned} \tag{28}$$

$$\begin{aligned} w_j = {} & v_G + \frac{\partial w_G}{\partial x}[d_{x,j}h] + \frac{\partial w_G}{\partial y}[d_{y,j}b_y h] + \frac{\partial^2 v_G}{\partial x^2}\frac{[d_{x,j}h]^2}{2!} \\ & + \frac{\partial^2 w_G}{\partial y^2}\frac{[d_{y,j}b_y h]^2}{2!} + 2\frac{\partial^2 w_G}{\partial x \partial y}\frac{[d_{x,j}h][d_{y,j}b_y h]}{2!} + \cdots\,, \end{aligned} \tag{29}$$

where $p = 3(l-1) + i$ with $i, l = 1, 2, 3$ and $j = 1, 2, \ldots, 5$ (see Fig. 3a), $dx_G = \frac{x_G - x_5}{h}$ and $dy_G = \frac{y_G - y_5}{b_y h}$. The function v_p in Eq. (28) is u_p^*, u_p^{**}, $\frac{\partial^n u_p^*}{\partial t^n}$ and $\frac{\partial^n u_p^{**}}{\partial t^n}$, the function w_j in Eq. (29) is $u_{G,j}^*$, $u_{G,j}^{**}$, $\frac{\partial u_{G,j}^*}{\partial x}$, $\frac{\partial u_{G,j}^{**}}{\partial x}$, $\frac{\partial u_{G,j}^*}{\partial y}$, $\frac{\partial u_{G,j}^{**}}{\partial y}$, $\frac{\partial^n u_{G,j}^*}{\partial t^n}$, $\frac{\partial^n u_{G,j}^{**}}{\partial t^n}$, $\frac{\partial^{n+1} u_{G,j}^*}{\partial t^n \partial x}$, $\frac{\partial^{n+1} u_{G,j}^{**}}{\partial t^n \partial x}$, $\frac{\partial^{n+1} u_{G,j}^*}{\partial t^n \partial y}$, $\frac{\partial^{n+1} u_{G,j}^{**}}{\partial t^n \partial y}$, $\frac{\partial^{2n} u_{G,j}^*}{\partial t^{2n}}$, $\frac{\partial^{2n} u_{G,j}^{**}}{\partial t^{2n}}$. The exact solution u_G^* and u_G^{**} to the wave and heat equations, Eqs. (1) and (2), at the central interface point $G = G_3$ with the coordinates $x_G = x_{G,3}$

and $y_G = y_{G,3}$ meets the following equations:

$$\frac{\partial^n u_G^*}{\partial t^n} - \bar{c}_* \nabla^2 u_G^* = f_G^*, \qquad \frac{\partial^n u_G^{**}}{\partial t^n} - \bar{c}_{**} \nabla^2 u_G^{**} = f_G^{**}, \tag{30}$$

$$\frac{\partial^{(i+j+ln)} u_G^*}{\partial t^{ln} \partial x^i \partial y^j} - \bar{c}_* \frac{\partial^{(i+j+(l-1)n)} \nabla^2 u_G^*}{\partial x^i \partial y^j \partial t^{(l-1)n}} = \frac{\partial^{(i+j+(l-1)n)} f_G^*}{\partial x^i \partial y^j \partial t^{(l-1)n}}, \qquad \frac{\partial^{(i+j+ln)} u_G^{**}}{\partial t^{ln} \partial x^i \partial y^j} - \bar{c}_{**} \frac{\partial^{(i+j+(l-1)n)} \nabla^2 u_G^{**}}{\partial x^i \partial y^j \partial t^{(l-1)n}} = \frac{\partial^{(i+j+(l-1)n)} f_G^{**}}{\partial x^i \partial y^j \partial t^{(l-1)n}} \tag{31}$$

with $l = 1, 2$ and $i, j = 0, 1, 2, 3, 4, \ldots$. Here, Eq. (31) is directly obtained by the differentiation of Eq. (30) with respect to t^n, x^i and y^j. Inserting Eqs. (28)–(29) and Eqs. (30)–(31) with zero load (source) term $\bar{f}_5 = 0$ into Eq. (27) we will get the following local truncation error in space e:

$$\begin{aligned}
e = {} & b_1 u_G^* + b_2 u_G^{**} + h(b_3 \frac{\partial u_G^*}{\partial x} + b_4 \frac{\partial u_G^{**}}{\partial x} + b_5 \frac{\partial u_G^*}{\partial y} + b_6 \frac{\partial u_G^{**}}{\partial y}) \\
& + h^2(b_7 \frac{\partial^2 u_G^*}{\partial x^2} + b_8 \frac{\partial^2 u_G^{**}}{\partial x^2} + b_9 \frac{\partial^2 u_G^*}{\partial x \partial y} + b_{10} \frac{\partial^2 u_G^{**}}{\partial x \partial y} + b_{11} \frac{\partial^2 u_G^*}{\partial y^2} + b_{12} \frac{\partial^2 u_G^{**}}{\partial y^2}) \\
& + h^3(b_{13} \frac{\partial^3 u_G^*}{\partial x^3} + b_{14} \frac{\partial^3 u_G^{**}}{\partial x^3} + b_{15} \frac{\partial^3 u_G^*}{\partial x^2 \partial y} + + b_{16} \frac{\partial^3 u_G^{**}}{\partial x^2 \partial y} + b_{17} \frac{\partial^3 u_G^*}{\partial x \partial y^2} + b_{18} \frac{\partial^3 u_G^{**}}{\partial x \partial y^2} + b_{19} \frac{\partial^3 u_G^*}{\partial y^3} + b_{20} \frac{\partial^3 u_G^{**}}{\partial y^3}) \\
& + h^4(b_{21} \frac{\partial^4 u_G^*}{\partial x^4} + b_{22} \frac{\partial^4 u_G^{**}}{\partial x^4} + b_{23} \frac{\partial^4 u_G^*}{\partial x^3 \partial y} + b_{24} \frac{\partial^4 u_G^{**}}{\partial x^3 \partial y} + b_{25} \frac{\partial^4 u_G^*}{\partial x^2 \partial y^2} \\
& + b_{26} \frac{\partial^4 u_G^{**}}{\partial x^2 \partial y^2} + b_{27} \frac{\partial^4 u_G^*}{\partial x \partial y^3} + b_{28} \frac{\partial^4 u_G^{**}}{\partial x \partial y^3} + b_{29} \frac{\partial^4 u_G^*}{\partial y^4} + b_{30} \frac{\partial^4 u_G^{**}}{\partial y^4}) \\
& + h^5(b_{31} \frac{\partial^5 u_G^*}{\partial x^5} + b_{32} \frac{\partial^5 u_G^{**}}{\partial x^5} + b_{33} \frac{\partial^5 u_G^*}{\partial x^4 \partial y} + b_{34} \frac{\partial^5 u_G^{**}}{\partial x^4 \partial y} + b_{35} \frac{\partial^5 u_G^*}{\partial x^3 \partial y^2} + b_{36} \frac{\partial^5 u_G^{**}}{\partial x^3 \partial y^2} \\
& + b_{37} \frac{\partial^5 u_G^*}{\partial x^2 \partial y^3} + b_{38} \frac{\partial^5 u_G^{**}}{\partial x^2 \partial y^3} + b_{39} \frac{\partial^5 u_G^*}{\partial x \partial y^4} + b_{40} \frac{\partial^5 u_G^{**}}{\partial x \partial y^4} + b_{41} \frac{\partial^5 u_G^*}{\partial y^5} + b_{42} \frac{\partial^5 u_G^{**}}{\partial y^5}) \\
& + h^6(b_{43} \frac{\partial^6 u_G^*}{\partial x^6} + b_{44} \frac{\partial^6 u_G^{**}}{\partial x^6} + b_{45} \frac{\partial^6 u_G^*}{\partial x^5 \partial y} + b_{46} \frac{\partial^6 u_G^{**}}{\partial x^5 \partial y} + b_{47} \frac{\partial^6 u_G^*}{\partial x^4 \partial y^2} + b_{48} \frac{\partial^6 u_G^{**}}{\partial x^4 \partial y^2} + b_{49} \frac{\partial^6 u_G^*}{\partial x^3 \partial y^3} + b_{50} \frac{\partial^6 u_G^{**}}{\partial x^3 \partial y^3} \\
& + b_{51} \frac{\partial^6 u_G^*}{\partial x^2 \partial y^4} + b_{52} \frac{\partial^6 u_G^{**}}{\partial x^2 \partial y^4} + b_{53} \frac{\partial^6 u_G^*}{\partial x \partial y^5} + b_{54} \frac{\partial^6 u_G^{**}}{\partial x \partial y^5} + b_{55} \frac{\partial^6 u_G^*}{\partial y^6} + b_{56} \frac{\partial^6 u_G^{**}}{\partial y^6}) + O(h^7),
\end{aligned} \tag{32}$$

where the coefficients b_p ($p = 1, 2, \ldots, 56$) are expressed in terms of the coefficients m_i, k_i, $q_{1,j}$, $q_{2,j}$, $q_{3,l}$, q_4 and q_5; see Appendix B. We should mention that by the use of the wave (heat) equation, Eqs. (30)–(31), the time derivatives for the local truncation error in Eq. (32) are excluded.

For the uniform stencil with the horizontal (or vertical) interface in Fig. 3b with $d_p = 1$ ($p = 1, 2, \ldots, 9$), with the distance $\xi b_y h$ between the central grid point u_5^{**} and the horizontal interface, with the components of the normal vectors to the interface $n_{x,j} = 0$ and $n_{y,j} = 1$ ($j = 1, 2, 3, 4, 5$), the expressions for coefficients b_p ($p = 1, 2, \ldots, 56$) are simplified and the stencil coefficients can be analytically obtained. For example, equating to zero coefficients $b_p = 0$ ($p = 1, 2, \ldots, 26, 29, 30, 38$), $q_{2,1} = q_{3,2} = q_{3,4} = 0$ and using the scaling equation $k_5 = 1$ we get 33 algebraic equations with the 33 unknown stencil coefficients m_i, k_i ($i = 1, 2, \ldots, 9$) and $q_{1,j}$, $q_{2,j}$, $q_{3,l}$, q_4 and q_5 ($j = 1, 2, \ldots, 5$, $l = 2, 3, 4$). Solving this system we can analytically find the 18 unknown stencil coefficients m_i and k_i ($i = 1, 2, \ldots, 9$); see Appendix C. Because some of the coefficients b_p in Eq. (32) are linearly dependent, the analytical solution given in Appendix C zeros the first 30 coefficients b_p in Eq. (32); i.e., for uniform stencils with the horizontal interface we can get the fifth order of the local truncation error in Eq. (32) (see Appendix C). It is also necessary to mention that for the uniform distribution of the five interface points G_i ($i = 1, 2, \ldots, 5$) (see Fig. 3b), the stencil coefficients in Appendix C are independent of the distance $\bar{h}$ between the interface points G_i.

Some analytical results for the stencil coefficients can be also obtained for the uniform stencil and the interface represented by an inclined line. In this case, if we zero the coefficients $b_p = 0$ ($p = 1, 2, \ldots, 30$) up to the fourth order in Eq. (32) then the stencil coefficients $k_i = 0$ ($i = 1, 2, \ldots, 9$) are zero; i.e., this solution is unacceptable and we cannot zero all coefficients $b_p = 0$ ($p = 1, 2, \ldots, 26, 29, 30$) up to the fourth order.

Therefore, we will use the following procedure in order to minimize the order of the local truncation error in Eq. (32) for uniform and non-uniform stencils for the general geometry of the interface. First, we will zero the first

20 coefficients b_p in Eq. (32) up to the third order with respect to h; i.e.,

$$b_p = 0\,, \qquad p = 1, 2, \ldots, 20\,. \tag{33}$$

Then, in order to have a sufficient number of equations for the calculation of the 33 stencil coefficients including m_i, k_i $(i = 1, 2, \ldots, 9)$ and $q_{1,j}$, $q_{2,j}$, $q_{3,l}$, q_4, q_5 $(j = 1, 2, \ldots, 5,\ l = 2, 3, 4)$, we use the least square method for the minimization of coefficients b_p related to the fourth and higher orders of the local truncation error with the following residual R:

$$R = \sum_{p=21}^{30} b_p^2 + h_1 \sum_{p=31}^{42} b_p^2 + h_2 \sum_{p=43}^{56} b_p^2\,, \tag{34}$$

where h_1 and h_2 are the weighting factors to be selected (e.g., the numerical experiments show that $h_1 = h_2 = 0.1$ yields accurate results). In order to minimize the residual R with the constraints given by Eq. (33), we can form a new residual $\bar{R}$ with the Lagrange multipliers λ_l:

$$\bar{R} = \sum_{l=1}^{20} \lambda_l b_l + \sum_{p=21}^{30} b_p^2 + h_1 \sum_{p=31}^{42} b_p^2 + h_2 \sum_{p=43}^{56} b_p^2\,. \tag{35}$$

The residual $\bar{R}$ is a quadratic function of the stencil coefficients m_i, k_i $(i = 1, 2, \ldots, 9)$ and $q_{1,j}$, $q_{2,j}$, $q_{3,r}$, q_4, q_5 $(j = 1, 2, \ldots, 5,\ r = 2, 3, 4)$ and a linear function of the Lagrange multipliers λ_l; i.e., $\bar{R} = \bar{R}(m_i, k_i, q_{1,j}, q_{2,j}, q_{3,r}, q_4, q_5, \lambda_l)$. In order minimize the residual $\bar{R} = \bar{R}(m_i, k_i, q_{1,j}, q_{2,j}, q_{3,r}, q_4, q_5, \lambda_l)$, the following equations based on the least square method for the residual $\bar{R}$ can be written down:

$$\begin{aligned}
&\frac{\partial \bar{R}}{\partial m_i} = 0\,, \quad \frac{\partial \bar{R}}{\partial k_i} = 0\,, \quad \frac{\partial \bar{R}}{\partial q_{1,j}} = 0\,, \quad \frac{\partial \bar{R}}{\partial q_{2,j}} = 0\,,\\
&\frac{\partial \bar{R}}{\partial q_{3,r}} = 0\,, \quad \frac{\partial \bar{R}}{\partial q_4} = 0\,, \quad \frac{\partial \bar{R}}{\partial q_5} = 0\,, \quad \frac{\partial \bar{R}}{\partial \lambda_l} = 0\,,\\
&i = 1, 2, \ldots, 9\,, \quad j = 1, 2, \ldots, 5\,, \quad r = 2, 3, 4\,, \quad l = 1, 2, \ldots, 20\,,
\end{aligned} \tag{36}$$

where equation $\frac{\partial \bar{R}}{\partial k_5} = 0$ should be replaced by $k_5 = 1$; see Remark 7 after Eq. (27). Eq. (36) forms a system of 53 linear algebraic equations with respect to 33 unknown coefficients m_i, k_i $(i = 1, 2, \ldots, 9)$ and $q_{1,j}$, $q_{2,j}$, $q_{3,r}$, q_4 and q_5 $(j = 1, 2, \ldots, 5,\ r = 2, 3, 4)$ and 20 Lagrange multipliers λ_l $(l = 1, 2, \ldots, 20)$. Solving these linear algebraic equations numerically, we can find the coefficients m_i, k_i $(i = 1, 2, \ldots, 9)$ for the 9-point non-uniform and uniform stencils. As can be seen, the presented procedure provides the fifth order of the local truncation error for the 9-point uniform stencils with a horizontal interface and the fourth order of the local truncation error for the 9-point uniform and non-uniform stencils with the general geometry of the interface. The 9-point uniform stencils of OLTEM for a homogeneous material (with no interface) provide the sixth order of the local truncation error. This leads to the fourth order of accuracy of global solutions; see the numerical examples below. Moreover, due to the minimization of the leading high-order terms of the local truncation error in Eq. (35) for uniform and nonuniform stencils, at the same numbers of degrees of freedom OLTEM on irregular domains yields more accurate results than those obtained by high-order finite elements (up to the third order) with much wider stencils; see the numerical examples below.

Remark 8. To estimate the computational costs of the solution of 53 linear algebraic equations formed by Eq. (36) we solved 10^6 such systems with a general MATLAB solver on a simple student laptop computer (Processor: Intel (R) Core(TM) i5-4210U CPU @ 1.70 GHz 2.40 GHz). The computation 'wall' time was $T = 5658$ s for 10^6 systems or the average time for one system was 0.005658 s. Because the coefficients m_i, k_i $(i = 1, 2, \ldots, 9)$ are independently calculated for different grid points, the computation time of their calculation for different grid points can be significantly reduced on modern parallel computers. This means that for large global systems of equations, the computation time for the calculation of the coefficients m_i, k_i $(i = 1, 2, \ldots, 9)$ is very small compared to

that for the solution of the global system of equations. We should mention that the coefficients $q_{1,j}$, $q_{2,j}$, $q_{3,r}$, q_4 and q_5 ($j = 1, 2, \ldots, 5$, $r = 2, 3, 4$) are used for the calculation of non-zero load (source) term $\bar{f}_5$ only (see the next section) while the Lagrange multipliers λ_l in the local system of equations, Eq. (36), are only used for the calculation of the unknown coefficients m_i, k_i ($i = 1, 2, \ldots, 9$), $q_{1,j}$, $q_{2,j}$, $q_{3,r}$, q_4 and q_5 ($j = 1, 2, \ldots, 5$, $r = 2, 3, 4$) and are not used in the global system of equations.

The global semi-discrete system of equations includes the 9-point uniform and nonuniform stencils with and without interfaces between different materials (see Figs. 2–3) for all internal grid points located inside the domain. The difference between the 9-point uniform and nonuniform (for the grid points located close to curved boundary; see Fig. 2b) stencils is in the values of the d_p ($p = 1, 2, \ldots, 9$) coefficients in Eq. (23). These d_p coefficients contribute to the calculations of the b_p coefficients in Eq. (32); see also Appendix B. Numerical examples with the application of nonuniform stencils to curved boundary can be found in our recent papers [38,41,45] for PDEs with constant coefficients.

Remark 9. In the presented approach we use the non-diagonal mass matrix with 9 m_p ($p = 1, 2, \ldots, 9$) coefficients contributing to the mass matrix. In this case we can get a high order of accuracy. Therefore, in the numerical examples considered below we use implicit time integration methods. In our paper [16] we have shown that the 9-point stencils with the diagonal mass matrix ($m_5 \neq 0$ and $m_p = 0$ ($p = 1, \ldots, 4, 6, \ldots, 9$)) can provide only the second order of accuracy (similar to that for linear finite elements) for the wave (heat) equation with constant coefficients.

Remark 10. Here we considered the derivation of the stencils coefficients of the 9-point stencils for the 2-D wave and heat equations with heterogeneous materials that include interfaces. The derivation of the stencils coefficients of the 9-point stencils for the 2-D wave and heat equations with homogeneous materials that are also used for numerical simulations is presented in our paper [36]. It is interesting to mention that the stencil coefficients can be also derived by using the central grid point with the coordinates x_5 and y_5 in Eqs. (28)–(32) instead of the interface point with the coordinates x_G and y_G.

4.2. Nonzero load (source) term $f_l \neq 0$ in Eqs. (1) and (2)

The inclusion of non-zero loading (source) term f_l in the partial differential equations, Eqs. (1) and (2), leads to the non-zero term $\bar{f}_5$ in the stencil equation, Eq. (25) (similar to Eq. (5)). As we mentioned after Eq. (4), the functions f_l can be discontinuous across the interfaces. The expression for the term $\bar{f}_5$ can be calculated from the procedure used for the derivation of the local truncation error in the case of zero loading (source) term as follows. In the case of non-zero loading (source) term $f_l(\boldsymbol{x}, t) \neq 0$ and $f_5 \neq 0$, the insertion of Eqs. (28)–(29) and Eqs. (30)–(31) into Eq. (27) yields the following local truncation error in space e_f:

$$\begin{aligned} e_f = e - [\bar{f}_5 - \mathbf{h}^2((a_1m_1 + a_2m_2 + a_3m_3 + a_4m_4 + a_5m_5 + a_6m_6 + a_7m_7 + a_8m_8 + a_9m_9 + q_{3,2} + q_{3,3} + q_{3,4})f_G^* \\ +(-a_1m_1 + m_1 - a_2m_2 + m_2 - a_3m_3 + m_3 - a_4m_4 + m_4 - a_5m_5 + m_5 - a_6m_6 + m_6 - a_7m_7 + m_7 - a_8m_8 + m_8 \\ -a_9m_9 + m_9 - q_{3,2} - q_{3,3} - q_{3,4})f_G^{**}) + \mathbf{h}^3 \ldots], \end{aligned} \tag{37}$$

where e is the local truncation error in space given by Eq. (32) for zero loading (source) term, f_G^* and f_G^{**} designate functions $f^*(x, y, t)$ and $f^{**}(x, y, t)$ calculated at the central interface point with the coordinates $x = x_G$ and $y = y_G$. Equating to zero the expression in the square brackets on the right-hand side of Eq. (37), we will get the expression for $\bar{f}_5$:

$$\begin{aligned} \bar{f}_5 = \mathbf{h}^2((a_1m_1 + a_2m_2 + a_3m_3 + a_4m_4 + a_5m_5 + a_6m_6 + a_7m_7 + a_8m_8 + a_9m_9 + q_{3,2} + q_{3,3} + q_{3,4})f_G^* \\ +(-a_1m_1 + m_1 - a_2m_2 + m_2 - a_3m_3 + m_3 - a_4m_4 + m_4 - a_5m_5 + m_5 - a_6m_6 + m_6 - a_7m_7 + m_7 - a_8m_8 + m_8 \\ -a_9m_9 + m_9 - q_{3,2} - q_{3,3} - q_{3,4})f_G^{**}) + \mathbf{h}^3 \ldots, \end{aligned} \tag{38}$$

as well as we will get the same local truncation errors $e_f = e$ for zero and non-zero loading (source) term (see Appendix D for the detailed expression of $\bar{f}_5$). This means that the coefficients m_i, k_i ($i = 1, 2, \ldots, 9$) of the stencil equations are first calculated for zero loading (source) term $f_l = 0$ as described in Section 4.1. Then, the nonzero loading (source) term $\bar{f}_5$ given by Eq. (38) is used in the stencil equation, Eq. (25).

5. Numerical examples

In this Section the computational efficiency of OLTEM developed for the solution of the wave and heat equations with discontinuous coefficients will be demonstrated and compared with conventional linear (Q2, T3, Q4) and high order (quadratic Q3, T6, Q9 and cubic T10, Q16) finite elements. 'T' and 'Q' designate the triangular and quadrilateral finite elements in the 1-D (Q2, Q3) and 2-D (T3, Q4, T6, Q9, T10, Q16) cases. For finite element calculations, the commercial finite element software 'COMSOL' with isoparametric finite elements is used. Similar to the finite element terminology, a grid point of a Cartesian mesh will be called a node. In order to compare the accuracy of OLTEM with FEM, the following errors are considered in this Section. The relative errors e_u^j for the function u and e_v^j for its first time derivative at the jth node are defined as:

$$e_u^j = \frac{\mid u_j^{num} - u_j^{exact} \mid}{u_{max}^{exact}} \qquad \text{and} \qquad e_v^j = \frac{\mid v_j^{num} - v_j^{exact} \mid}{v_{max}^{exact}}, \qquad j = 1, 2, \dots, N. \tag{39}$$

The maximum relative errors e_u^{max} for the function u and e_v^{max} for its first time derivative are defined as:

$$e_u^{max} = \max_j e_u^j \qquad \text{and} \qquad e_v^{max} = \max_j e_v^j, \qquad j = 1, 2, \dots, N. \tag{40}$$

In Eqs. (39)–(40) the superscripts $'num'$ and $'exact'$ correspond to the numerical and exact solutions, N is the total number of the grid points used in calculations, u_{max}^{exact} and v_{max}^{exact} are the maximum absolute value of the exact solution over the entire spatial and temporal domain for the function u and its first time derivative, respectively. We also use the L^2 error norm for finite elements (e.g., see [46]) and the l^2 error norm (e.g., see [47]) for OLTEM:

$$e_w^{l^2} = \{dx\, dy \sum_{i=0}^{N_x} \sum_{j=0}^{N_y} [w^{num}(x_i, y_j) - w^{exact}(x_i, y_j)]^2\}^{\frac{1}{2}}, \tag{41}$$

where $w = u$ for the function u and $w = v$ for the its first time derivative v; N_x and N_y are the numbers of Cartesian grid points along x- and y-axes; x_i and y_j are the coordinates of Cartesian grid points. All the above mentioned errors are evaluated at the final observation time. The errors e_v^j and e_v^{max} are used for the wave equation only. For convenience, index l related to subdomain Ω_l is dropped as well as u and v are called the displacement and the velocity for the wave equation; and u is called the temperature for the heat equation. For the time integration, the trapezoidal rule is used for the wave equation and the backward difference method is used for the heat equation. A sufficiently small size of time steps is used in calculations. Therefore, the error in time is negligible and the numerical error is related to the space-discretization error only.

Remark 11. The numerical experiments presented below show that at the same numbers of degrees of freedom, approximately the same time increments can be used for OLTEM and linear finite elements. For example, for the problems in Sections 5.3–5.4, OLTEM and linear finite elements with approximately 3300 degrees of freedom require the time increments $\Delta t = 0.00122$ for the small error in time. However, the maximum relative error in space in this case is 1.2% for OLTEM and 70% for linear finite elements. In order to have the same error in space for OLTEM and linear finite elements, a much larger number of degrees of freedom is required for linear finite elements. However, this leads to a significant decrease in the size of time increments for linear finite elements. For example, for the maximum relative error in space of 1.2%, linear finite elements requires 256895 degrees of freedom with much smaller $\Delta t = 0.0000185$ time increments. This trend was observed for all problems considered below as well as for the wave and heat equations with homogeneous materials considered in our paper [37].

Remark 12. In OLTEM presented in the paper, function u is the basic unknown in the stencil equations. Therefore, in the numerical examples in this section we plot function u. If necessary the fluxes for OLTEM can be calculated during post-processing using any approach and any approximation for fluxes. This is exactly the same procedure as that for conventional finite elements.

5.1. Traveling waves in a 1-D bi-material bar

Let us consider wave propagation in the 1-D bi-material bar; see Fig. 4. Young's modulus E, the density ρ and the corresponding wave velocity $c^2 = E/\rho$ are selected to be $E_I = 1/2$, $\rho_I = 1/2$ and $c_I = 1$ for the left half of

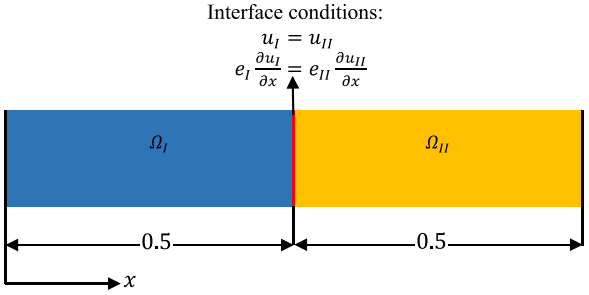

Fig. 4. Wave propagation in a 1-D bi-material bar.

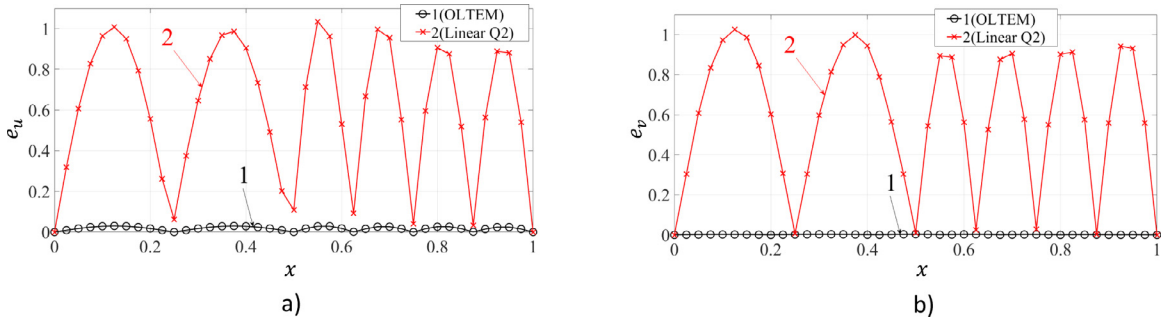

Fig. 5. The distribution of the relative errors in displacement e_u (a) and in velocity e_v (b) as a function of distance x from the left end of the bi-material bar; see Fig. 4. The numerical solutions of the 1-D wave equation are obtained by OLTEM (curve 1) and by linear $Q2$ finite elements (curve 2) on a uniform mesh of size $h = 1/40$.

the bar Ω_I and $E_{II} = 1/4$, $\rho_{II} = 1$ and $c_{II} = 1/2$ for the right half of the bar Ω_{II}. The following coefficients e_I and e_{II} are used in the interface conditions: $e_I = E_I = 1/2$ and $e_{II} = E_{II} = 1/4$. Based on the method of manufactured solutions, the following exact solution to the 1-D wave equation can be constructed:

$$u(x,t) = \begin{cases} cos\{4\pi(x+t)\} & \text{in} \quad \Omega_I \\ cos\{4\pi(2x+t)\} & \text{in} \quad \Omega_{II}. \end{cases} \tag{42}$$

It meets the interface conditions shown in Fig. 4 as well as the 1-D wave equation with zero loading term. The initial conditions at time $t = 0$ in the entire domain and the Dirichlet boundary conditions at both ends of the bar are imposed according to the exact solution given by Eq. (42). This problem is solved by linear $Q2$ finite elements and by OLTEM.

In order to compare the accuracy of the numerical results obtained by OLTEM and by linear finite elements (these two methods have the same width of the stencil equations), Fig. 5 shows the relative error in displacement e_u and in velocity e_v at the final observation time $T = 10$ as a function of the distance x along the bar for the mesh size $h = 1/40$. It can be seen that the results obtained by OLTEM are much more accurate than those obtained by linear $Q2$ finite elements; see Fig. 5. In order to compare the convergence of different numerical techniques at mesh refinement, the maximum relative errors in displacement e_u^{max} and in velocity e_v^{max} are plotted in Fig. 6 as a function of the mesh size h in the logarithmic scale. As can be seen, OLTEM yields more accurate results than those by linear $Q2$ finite elements at the same h. It can also be seen from Fig. 6 that the order of accuracy for OLTEM is close to four. This is in agreement with the theoretical results in Section 3.

In the Introduction we mentioned the finite element techniques for the wave equation (see [1–8] and other) based on the modified integration rule (MIR) or the averaged mass matrix (these techniques coincide in the 1-D case and result in 3-point stencils for linear finite elements). They improve the order of convergence of linear finite elements to four for the wave equation with constant coefficients. However, these techniques do not improve the order of convergence of linear finite elements in the case of discontinuous coefficients; see curve 2 for $Q2\_MIR$ in Fig. 6.

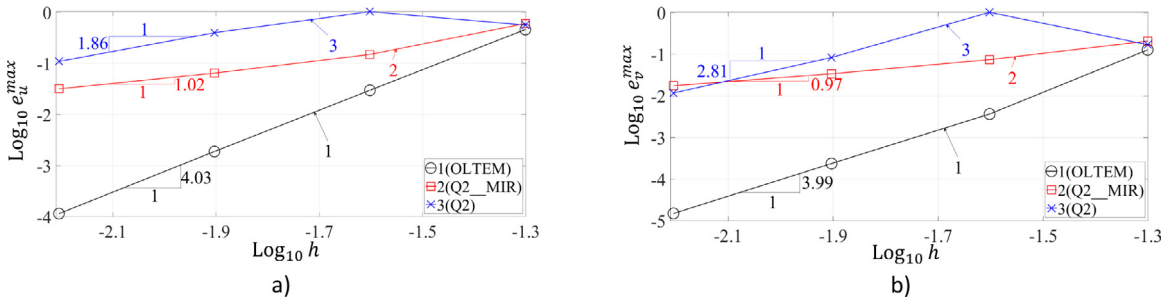

Fig. 6. The maximum relative errors in displacement e_u^{max} (a) and in velocity e_v^{max} (b) as a function of the mesh size h in the logarithmic scale at mesh refinement. The numerical solutions of the 1-D wave equation for the bi-material bar are obtained by OLTEM (curve 1), by conventional linear $Q2$ finite elements (curve 3) and by the modified linear $Q2\_MIR$ finite elements (curve 2) on uniform meshes.

It can be concluded that in contrast to the known finite element techniques with the 3-point stencils, the proposed OLTEM improves the order of accuracy to four not only for the wave equation with constant coefficients but also for the wave equation with discontinuous coefficients.

5.2. Wave propagation in a 1-D bi-material bar under impact loading

Let us consider a 1-D bi-material bar under impact loading; see Fig. 4. Young's modulus E, the density ρ and the corresponding wave velocity $c^2 = E/\rho$ are selected to be $E_I = 1$, $\rho_I = 1$ and $c_I = 1$ for the left half of the bar Ω_I and $E_{II} = 1/4$, $\rho_{II} = 1$ and $c_{II} = 1/2$ for the right half of the bar Ω_{II}. The following coefficients e_I and e_{II} are used in the interface conditions: $e_I = E_I = 1$ and $e_{II} = E_{II} = 1/4$. The boundary conditions are: the displacement $u(x = 0, t) = t$ is applied at the left end of the bar. This corresponds to the velocity $v(x = 0, t) = 1$ instantaneously applied at the left end of the bar (impact loading). The right end of the bar is free of forces. The initial displacements and velocities at time $t = 0$ are zero, the observation time is selected to be $T = 0.8$. This problem has the continuous solution for the displacement and the discontinuous solution for the velocities. The exact solution for this problem (see curves 3 in Fig. 7) can be found using the approach presented in [16].

This impact problem is solved by OLTEM and by linear and quadratic finite elements on the same mesh with 201 degrees of freedom. It is known that the accurate time integration of the semidiscrete systems for impact problems may lead to large spurious oscillations in numerical results. Therefore, the two-stage time-integration procedure with the basic computations and the filtering stage (that has been developed in our papers [48–50]) is used to obtain accurate and non-oscillatory numerical results. The basic calculations in this procedure correspond to the accurate time integration of the semidiscrete system and are equivalent to the time integration procedure used for the first test problem in Section 5.1. The velocity distributions along the bar at time $T = 0.8$ after the stage of basic computations and after the filtering stage are shown in Fig. 7 for OLTEM and for linear and quadratic finite elements on the same mesh with 201 degrees of freedom. As can be seen, two considered approaches yield large spurious oscillation after basic computations. However, it is very easy to compare the numerical results after the filtering stage. As can be seen from Fig. 7b,d, after the filtering stage OLTEM yields more accurate results compared to those obtained by linear finite elements and slightly more accurate results compared to those obtained by quadratic finite elements.

It is interesting to note that higher order isogeometric elements (with continuous high-order spatial derivatives) applied to the same 1-D impact problem yield more accurate results than lower order isogeometric elements (e.g., see [50]); i.e., the approximation of discontinuous solutions by smooth functions of high-order isogeometric elements yields accurate results.

5.3. Traveling waves in a 2-D bi-material plate with the horizontal interface

Let us consider wave propagation in a 2-D bi-material plate $ABCDEF$ consisting of two square plates $ABCF$ (domain Ω_I) and $CDEF$ (domain Ω_{II}) with the horizontal interface FC; see Fig. 8. For the horizontal interface the components of the unit normal used in the interface conditions equal $n_x = 0$ and $n_y = 1$ for all interface points.

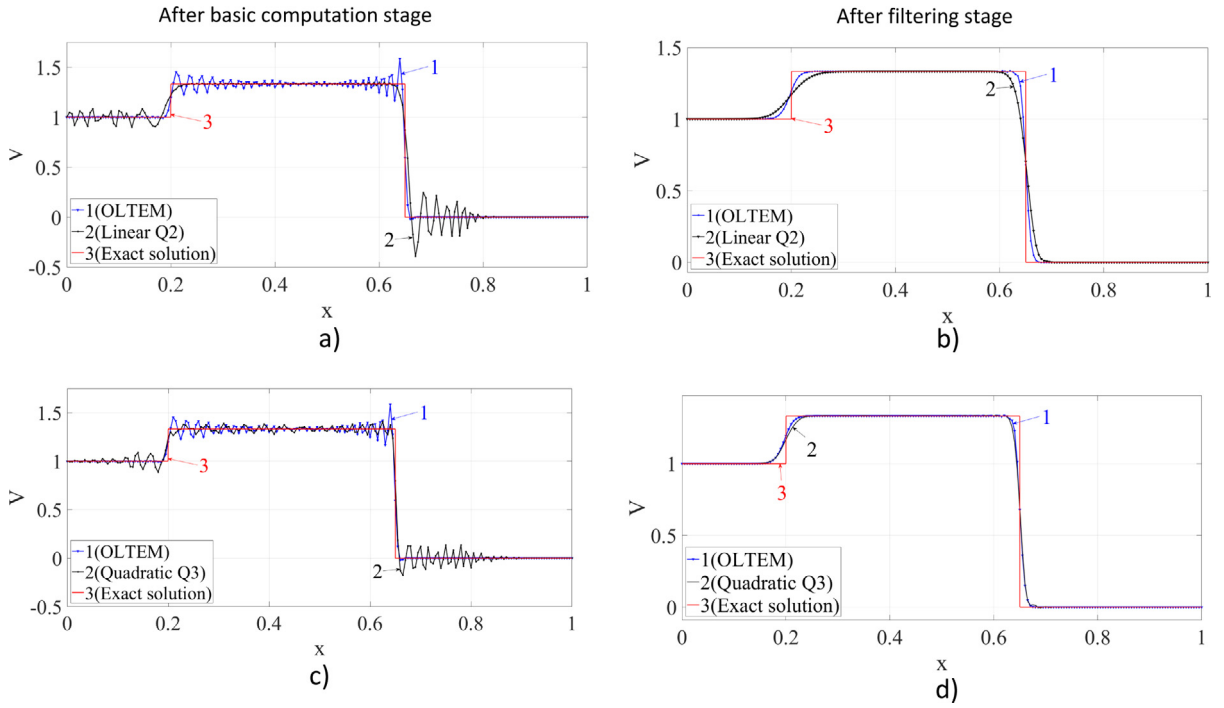

Fig. 7. The velocity distribution along the 1-D bi-material bar (see Fig. 4 for the bar) after basic computations (a, c) and after the filtering stage (b, d). The numerical solutions of the 1-D wave equation for the bi-material bar under impact loading are obtained by OLTEM (curve 1) and by conventional linear $Q2$ (curve 2(a, b)) and quadratic $Q3$ (curve 2(c, d)) finite elements with 201 degrees of freedom. Curve 3 corresponds to the exact solution.

The wave velocities are selected to be $c_I = 2/\sqrt{5}$ for $ABCF$ (domain Ω_I) and $c_{II} = 1/\sqrt{5}$ for $CDEF$ (domain Ω_{II}). The following coefficients e_I and e_{II} are used in the interface conditions: $e_I = 4/5$ and $e_{II} = 1/5$. Based on the method of manufactured solutions, the following exact solution to the 2-D wave equation can be constructed:

$$u(x, y, t) = \begin{cases} cos(4\pi x)cos\{2\pi(y + 2t)\}, & \text{in} \quad \Omega_I \\ cos(4\pi x)cos\{4\pi(2y + t)\}, & \text{in} \quad \Omega_{II} \end{cases} \tag{43}$$

It meets the interface conditions shown in Fig. 8a as well as the 2-D wave equation with zero loading term. The observation time is chosen to be $T = 5$. Fig. 9a,c shows the distribution of the displacement and the velocity of the exact solution at time $T = 5$. The initial conditions at time $t = 0$ in the entire domain and the Dirichlet boundary conditions along AB, BD, DE and EA are imposed according to the exact solution given by Eq. (43). This problem is solved by linear, quadratic and cubic finite elements as well as by OLTEM. For convenience, for OLTEM we use the Cartesian meshes for which two vertical grid lines are matched with the boundary BD and EA. Then, moving the Cartesian mesh in the vertical direction, the non-matched and matched (with the interface FC as well as with the boundaries AB and DE) meshes can be created. Fig. 8b shows examples of non-matched and matched Cartesian meshes (only matched meshes are used in finite element calculations).

First, we solve the problem by OLTEM on the matched square ($b_y = 1$) Cartesian mesh of size $h = 1/80$. Fig. 9 shows the distribution of the relative error in the numerical results for the displacement and for the velocity. As can be seen from Fig. 9b,d, the results obtained by OLTEM are accurate (the errors are small). We should also mention that the stencil coefficients obtained analytically (see Appendix C) and calculated numerically from the general procedure (see Eq. (36)) yield practically the same results.

Next, let us analyze the effect of non-matched (with the interface) meshes on the accuracy of the numerical solutions obtained by OLTEM. We start with a mesh matched with the interface FC; see Fig. 8c. Then, we move the mesh in the vertical direction by a distance ξh , $(0 \leq \xi \leq 1)$ in order to create meshes non-matched with the interface; see Fig. 8b. Fig. 10 shows the results obtained by OLTEM for different distances ξ. As can be seen from

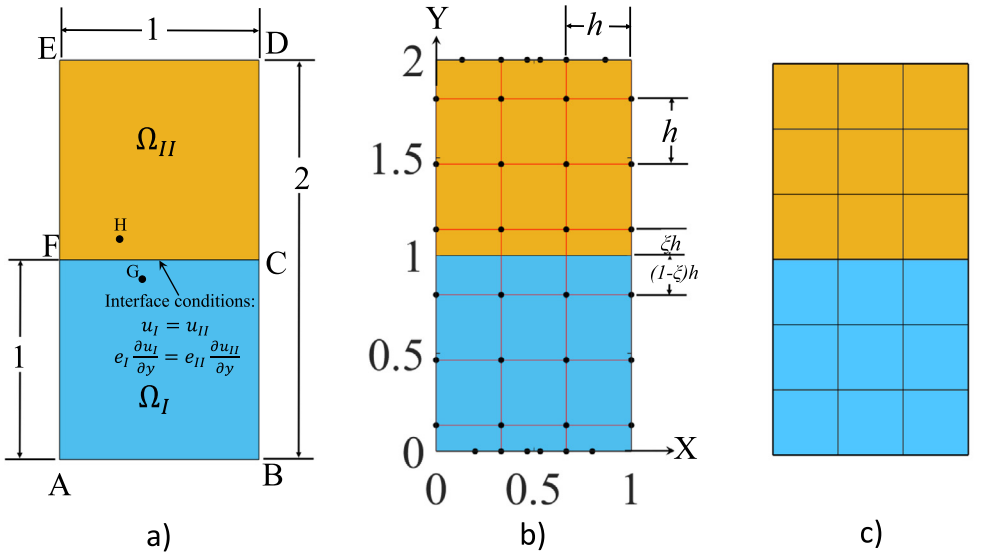

Fig. 8. A 2-D bi-material plate $ABCDEF$ with the horizontal interface FC (a). Examples of non-matched (b) and matched (c) Cartesian meshes.

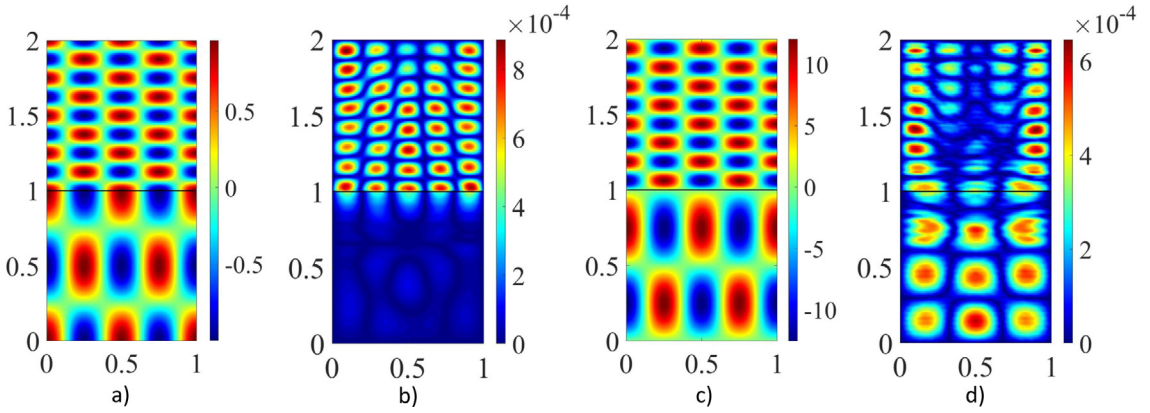

Fig. 9. The distribution of the displacement u (a) and velocity v (c) of the exact solution as well as the distribution of the relative errors in displacement e_u (b) and in velocity e_v (d) of the numerical solution for the 2-D plate with the horizontal interface; see Fig. 8a. The numerical solution for the 2-D wave equation is obtained by OLTEM on a square ($b_y = 1$) Cartesian mesh of size $h = 1/80$.

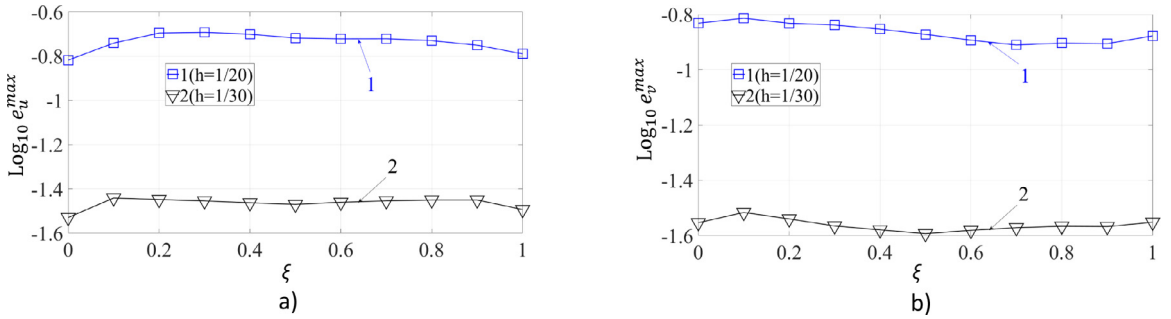

Fig. 10. The logarithm of the maximum relative errors in displacement e_u^{max} (a) and in velocity e_v^{max} (b) as a function ξ for the 2-D plate with horizontal interface (Fig. 8a). The numerical solutions of the 2-D wave equation with discontinuous properties are obtained by OLTEM on square ($b_y = 1$) Cartesian meshes with the mesh sizes $h = 1/20$ (curve 1) and $h = 1/30$ (curve 2).

Fig. 10, the maximum errors e_u^{max} and e_v^{max} are practically constant for different ξ at the constant mesh size h. This means that OLTEM yields almost the same results on matched and non-matched (with the interface) meshes.

In order to compare the accuracy of the numerical results obtained by different techniques, the errors e_u^{max} and e_v^{max} are plotted in Fig. 11 as a function of the number N of degrees of freedom in the logarithmic scale at mesh refinement. As can be seen, at the same N the numerical results obtained by OLTEM are more accurate than those obtained by linear and quadratic finite elements as well as they are close to those obtained by cubic finite elements. For the rectangular plate with Cartesian meshes, the relationship between h and N is $h = 1/\sqrt{N}$. Therefore, the slopes of the curves at large N in Fig. 11 correspond to the order of convergence. It can be also seen from Fig. 11 that the order of accuracy of OLTEM is close to four which is in agreement with the theoretical results in Section 4. A similar comparison of OLTEM with finite elements can be obtained in the L^2 error norm; see Fig. 12. At the same N the numerical results obtained by OLTEM are more accurate than those obtained by linear and quadratic finite elements and are close to those obtained by cubic finite elements. We should also mention that similar numerical results with the fourth order of convergence of OLTEM were obtained for different grid points.

Next let us compare the partial derivatives $\frac{\partial u}{\partial x}$ and $\frac{\partial u}{\partial y}$ for OLTEM and finite elements that can be calculated by post-processing the numerical results for function u. For OLTEM we will use the following simple formula that requires negligible computation time:

$$\left(\frac{\partial u}{\partial s}\right)_i \approx \frac{1}{ds}\left(\frac{1}{12}u_{i-2} - \frac{2}{3}u_{i-1} + \frac{2}{3}u_{i+1} - \frac{1}{12}u_{i+2}\right), \tag{44}$$

where $ds = dx$ for the x derivative and $ds = dy$ for the y derivative, $i = 1, 2, \ldots, 5$ correspond to five uniformly-spaced grid points with distance ds along the horizontal or vertical grid line that are located in the same subdomain. This formula provides the fourth order of the truncation error if the exact solution for u_i is used (this can be easily checked using a Taylor series for u_{i-2}, u_{i-1}, u_{i+1}, u_{i+2}):

$$\left(\frac{\partial u}{\partial s}\right)_i - \left(\frac{1}{12}u_{i-2} - \frac{2}{3}u_{i-1} + \frac{2}{3}u_{i+1} - \frac{1}{12}u_{i+2}\right) = -\frac{ds^4}{30}\left(\frac{\partial^5 u}{\partial s^5}\right)_i + O(ds^5). \tag{45}$$

We calculated the relative errors in the partial derivatives $e_{\frac{\partial u}{\partial x}} = \frac{1}{(\frac{\partial u}{\partial x})_{max}^{exact}}|(\frac{\partial u}{\partial x})^{num} - (\frac{\partial u}{\partial x})^{exact}|$ and $e_{\frac{\partial u}{\partial y}} = \frac{1}{(\frac{\partial u}{\partial y})_{max}^{exact}}|(\frac{\partial u}{\partial y})^{num} - (\frac{\partial u}{\partial y})^{exact}|$ at several grid points and obtained similar results at all points with similar orders of convergence (here $(\frac{\partial u}{\partial x})_{max}^{exact}$ and $(\frac{\partial u}{\partial y})_{max}^{exact}$ are the maximum absolute values of the partial derivatives over the entire domain). Therefore, Fig. 13 presents the numerical results of the convergence for the partial derivatives $\frac{\partial u}{\partial x}$ and $\frac{\partial u}{\partial y}$ at two points $G(0.4, 0.9)$ and $H(0.3, 1.1)$ located in different subdomains (see Fig. 8a for the locations of these points). As can be seen from Fig. 13, OLTEM yields more accurate results for $\frac{\partial u}{\partial x}$ and $\frac{\partial u}{\partial y}$ compared to those for linear, quadratic and cubic finite elements at the same number N of degrees of freedom. The fourth order of accuracy for OLTEM at mesh refinement in Fig. 13 will be studied in more detail in the future (we expected a lower order of convergence for $\frac{\partial u}{\partial x}$ and $\frac{\partial u}{\partial y}$ due to the use of numerical values of function u_i in Eq. (44)).

5.4. Traveling waves in a 2-D bi-material plate with the inclined interface

Here, we consider wave propagation in a 2-D bi-material plate $ABCDEF$ consisting of two trapezoidal plates $ABCF$ (domain Ω_I) and $CDEF$ (domain Ω_{II}) with the inclined interface FC; see Fig. 14a. For the inclined interface the components of the unit normal used in the interface conditions equal $n_x = -cos(50°)$ and $n_y = sin(50°)$ for all interface points. The same material properties as those in Section 5.3 are selected. We use a test problem with the same exact solution as Section 5.3 that is written down in the Cartesian system x' - y'; see Fig. 14a for the x' and y' axes. This solution can be rewritten in the Cartesian system x - y (see Fig. 14b for the x and y axes) as follows:

$$u(x, y, t) = \begin{cases} cos(4\pi x')cos\{2\pi(y' + 2t)\}, & \text{in} \quad \Omega_I \\ cos(4\pi x')cos\{4\pi(2y' + t)\}, & \text{in} \quad \Omega_{II} \end{cases} \tag{46}$$

with $x' = xcos(2\pi/9) + (y - 1)sin(2\pi/9)$ and $y' = -xsin(2\pi/9) + (y - 1)cos(2\pi/9)$.

Fig. 15a,c shows the distribution of the displacement and the velocity of the exact solution. The initial conditions at time $t = 0$ in the entire domain and the Dirichlet boundary conditions along AB, BD, DE and EA are imposed

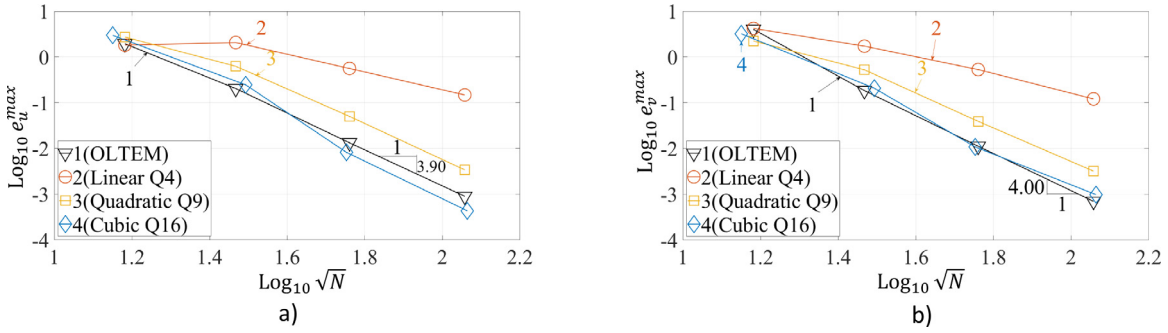

Fig. 11. The maximum relative errors in displacement e_u^{max} (a) and in velocity e_v^{max} (b) as a function of $\sqrt{N}$ in the logarithmic scale at mesh refinement for the 2-D plate with the horizontal interface (Fig. 8); N is the number of degrees of freedom. The numerical solutions of the 2-D wave equation are obtained by OLTEM (curve 1) and by linear and high-order finite elements (curves 2–4) on square ($b_y = 1$) Cartesian meshes. The Cartesian meshes of size $h = 1/10,\ 1/20,\ 1/40,\ 1/80$ are used for OLTEM and linear finite elements. The slopes of the curves 2–4 at mesh refinement are 1.93, 3.92, 4.03 in (a) and 2.16, 3.63, 3.45 in (b).

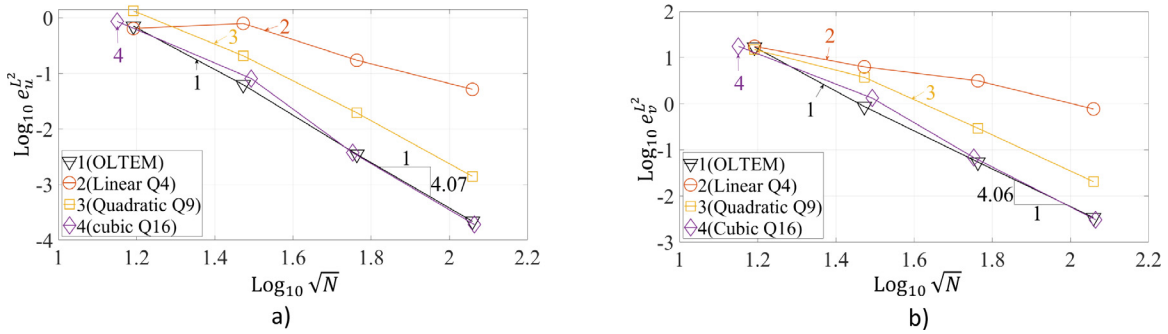

Fig. 12. The L^2 error norm for displacement $e_u^{L^2}$ (a) and for velocity $e_v^{L^2}$ (b) as a function of $\sqrt{N}$ in the logarithmic scale at mesh refinement for the 2-D plate with the horizontal interface (Fig. 8); N is the number of degrees of freedom. The numerical solutions of the 2-D wave equation are obtained by OLTEM (curve 1) and by linear, quadratic and cubic finite elements (curves 2, 3, 4) on square ($b_y = 1$) Cartesian meshes. The Cartesian meshes of size $h = 1/10,\ 1/20,\ 1/40,\ 1/80$ are used for OLTEM and linear finite elements. The slopes of the curves 2, 3, 4 at mesh refinement are 1.77, 3.87, 4.15 in (a) and 2.06, 3.91, 4.33 in (b).

according to the exact solution, Eq. (46). The observation time is chosen to be $T = 5$. The problem is solved by linear and high-order finite elements as well as by OLTEM. For convenience, Cartesian meshes used by OLTEM are always matched with the boundary AB and EA; i.e., the mesh is always non-matched with the inclined interface FC and can be non-matched or matched with the boundary BD and DE. Fig. 14b shows a typical non-matched Cartesian mesh used by OLTEM. Fig. 14c,d also shows examples of triangular and quadrilateral finite element meshes generated by COMSOL.

The distribution of the relative error of the numerical solution for the displacement and for the velocity obtained by OLTEM on the square ($b_y = 1$) Cartesian mesh of size $h = 1/80$ is shown in Fig. 15b,d. As can be seen from Fig. 15b,d, the results obtained by OLTEM are accurate (the errors are small).

In order to compare the accuracy of the numerical results obtained by different techniques, the errors e_u^{max} and e_v^{max} are shown in Fig. 16 as a function of the number N of degrees of freedom in the logarithmic scale at mesh refinement. As can be seen from Fig. 16, at the same N the numerical results obtained by OLTEM are much more accurate than those obtained by linear and quadratic finite elements (the OLTEM results are close to those for cubic elements in the considered mesh size range: they are slightly more accurate for coarse meshes and are slightly less accurate for fine meshes). For fine meshes the slopes of the curves for the cubic elements in Fig. 16a are slightly greater than those for OLTEM. It can be also seen from Fig. 16 that the order of accuracy of OLTEM exceeds three (for the problem under consideration it is close to four). This is in agreement with the theoretical results in Section 4. A similar comparison of OLTEM with finite elements can be obtained in the L^2 error norm; see Fig. 17.

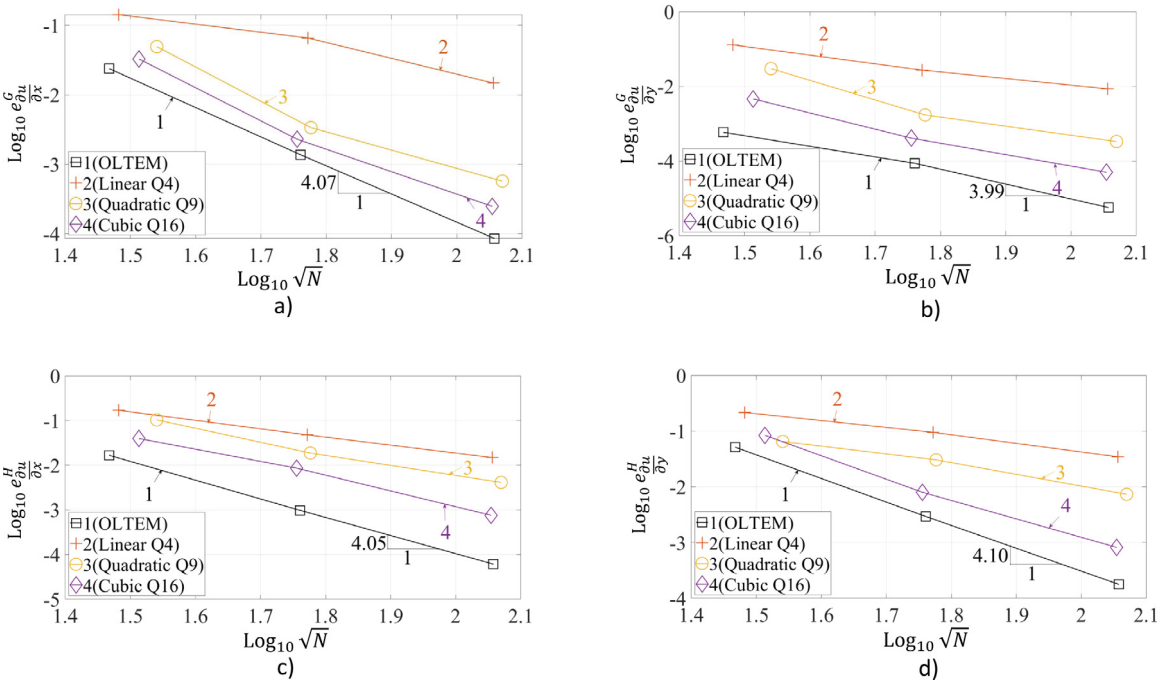

Fig. 13. The relative errors $e_{\frac{\partial u}{\partial x}}$ (a, c) and $e_{\frac{\partial u}{\partial y}}$ (b, d) in the partial derivatives $\frac{\partial u}{\partial x}$ and $\frac{\partial u}{\partial y}$ at point $G(0.4, 0.9)$ (a, b) and at point $H(0.3, 1.1)$ (c, d) (see Fig. 8) as a function of $\sqrt{N}$ in the logarithmic scale at mesh refinement; N is the number of degrees of freedom. The numerical solutions of the 2-D wave equation are obtained by OLTEM (curve 1) and by linear, quadratic and cubic finite elements (curves 2, 3, 4) on square ($b_y = 1$) Cartesian meshes. The Cartesian meshes of size $h = 1/20,\ 1/40,\ 1/80$ are used for OLTEM and linear finite elements. The slopes of the curves at mesh refinement 2–4 are 2.29, 2.63, 3.23 in (a); 1.77, 2.43, 3.05 in (b); 1.78, 2.25, 3.53 in (c) and 1.5, 2.1, 3.31 in (d).

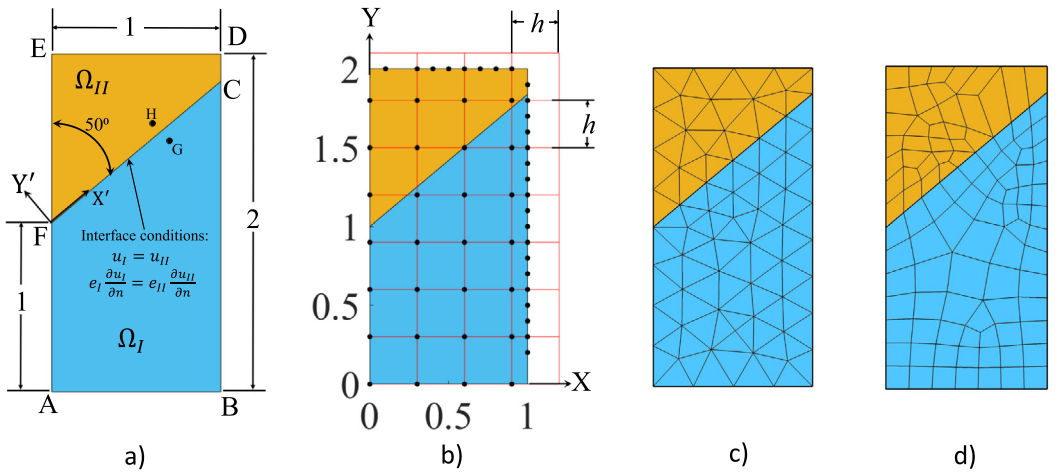

Fig. 14. A 2-D bi-material plate $ABCDEF$ with the inclined interface FC (a). Examples of a Cartesian mesh (b) for OLTEM as well as triangular (c) and quadrilateral (d) finite element meshes generated by the commercial software COMSOL.

At the same N the numerical results obtained by OLTEM are more accurate than those obtained by linear and quadratic finite elements and are close to those obtained by cubic finite elements. The order of convergence for OLTEM in the L^2 error norm is also close to four for the considered problem. The fourth order of convergence of OLTEM were also observed at different grid points.

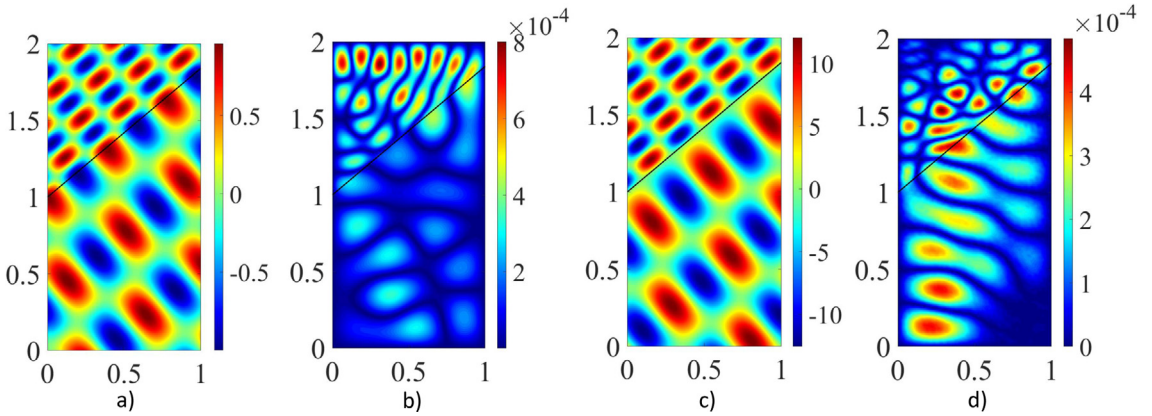

Fig. 15. The distribution of the displacement u (a) and velocity v (c) of the exact solution as well as the distribution of the relative errors in displacement e_u (b) and in velocity e_v (d) of the numerical solution for the 2-D plate with the inclined interface; see Fig. 14a. The numerical solution of the 2-D wave equation is obtained by OLTEM on the square ($b_y = 1$) Cartesian mesh of size $h = 1/80$.

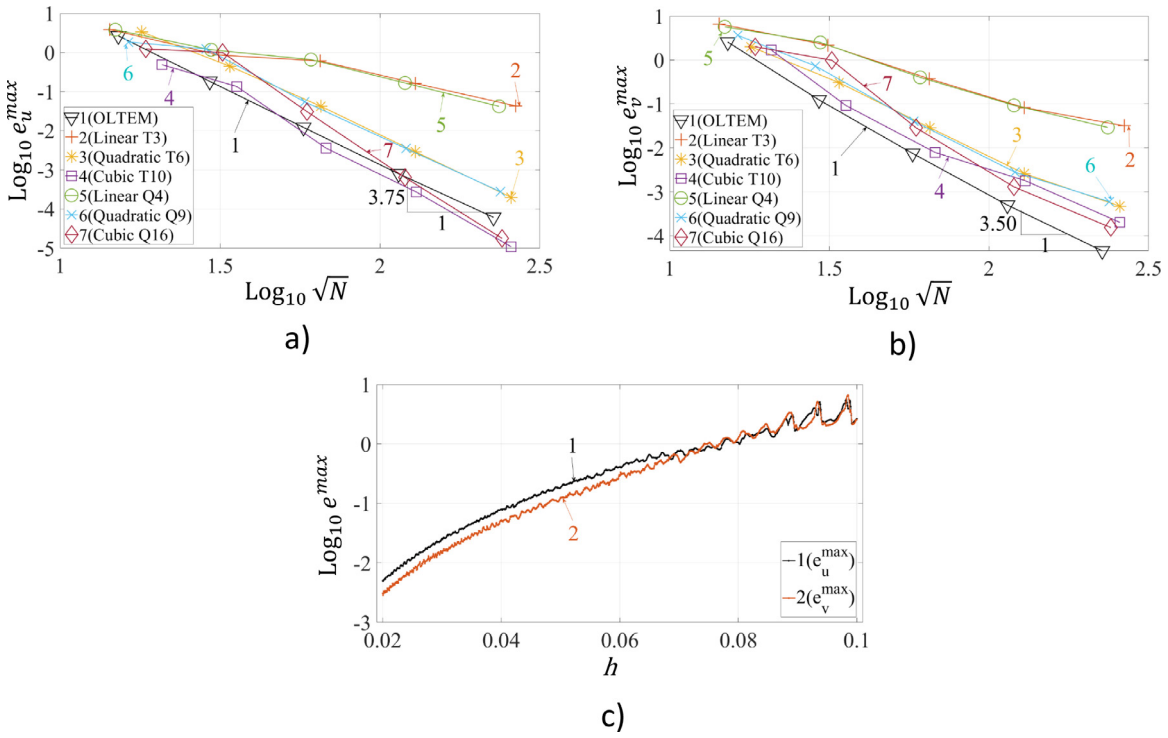

Fig. 16. The maximum relative errors in displacement e_u^{max} (a) and in velocity e_v^{max} (b) as a function of $\sqrt{N}$ (a, b) and the maximum relative errors as a function of the mesh size h (c) in the logarithmic scale at mesh refinement. N is the number of degrees of freedom. The numerical solutions of the 2-D wave equation for the 2-D plate with the inclined interface (Fig. 14a) are obtained by OLTEM (curve 1 in (a, b, c) and curve 2 in (c)) on uniform square ($b_y = 1$) Cartesian meshes and by linear (curves 2, 5 in (a, b)), quadratic (curves 3, 6 in (a, b)) and cubic (curves 4, 7 in (a, b)) finite elements on triangular (curves 2, 3, 4 in (a, b)) and quadrilateral (curves 5, 6, 7 in (a, b)) meshes. The Cartesian meshes of size $h = 1/10,\ 1/20,\ 1/40,\ 1/80,\ 1/160$ are used for OLTEM in (a, b). The slopes of the curves 2–7 at mesh refinement are 1.85 3.87, 4.67, 2.07, 3.72, 5.2 in (a) and 1.27, 2.10, 3.09, 1.03, 2.01, 3.11 in (b).

Next let us compare the partial derivatives $\frac{\partial u}{\partial x}$ and $\frac{\partial u}{\partial y}$ for OLTEM and finite elements that can be calculated by post-processing the numerical results for function u for OLTEM using Eq. (44). We calculated the relative errors

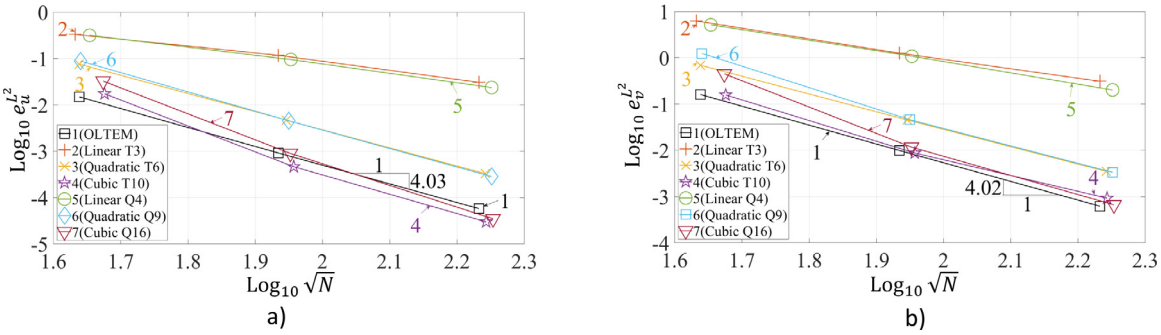

Fig. 17. The L^2 error norm for displacement $e_u^{L^2}$ (a) and for velocity $e_v^{L^2}$ (b) as a function of $\sqrt{N}$ in the logarithmic scale at mesh refinement for the 2-D plate with the inclined interface (Fig. 14); N is the number of degrees of freedom. The numerical solutions of the 2-D wave equation are obtained by OLTEM (curve 1) on square ($b_y = 1$) Cartesian meshes and by linear (curves 2, 5), quadratic (curves 3, 6) and cubic (curves 4, 7) triangular (2–4) and quadrilateral (5–7) finite elements. The Cartesian meshes of size $h = 1/30,\ 1/60,\ 1/120$ are used for OLTEM. The slopes of the curves 2–7 are 1.93, 3.83, 4.25, 2.01, 3.87, 4.73 in (a) and 2.00, 3.7, 3.46, 2.42, 3.77, 4.17 in (b).

in the partial derivatives $e_{\frac{\partial u}{\partial x}} = \frac{1}{(\frac{\partial u}{\partial x})^{exact}_{max}} |(\frac{\partial u}{\partial x})^{num} - (\frac{\partial u}{\partial x})^{exact}|$ and $e_{\frac{\partial u}{\partial y}} = \frac{1}{(\frac{\partial u}{\partial y})^{exact}_{max}} |(\frac{\partial u}{\partial y})^{num} - (\frac{\partial u}{\partial y})^{exact}|$ at several grid points and obtained similar results at all points with similar orders of convergence. Therefore, Fig. 13 presents the numerical results of the convergence for the partial derivatives $\frac{\partial u}{\partial x}$ and $\frac{\partial u}{\partial y}$ at two points $G(0.7, 1.5)$ and $H(0.6, 1.6)$ located in different subdomains (see Fig. 14a for the locations of these points). As can be seen from Fig. 18, OLTEM yields more accurate results for $\frac{\partial u}{\partial x}$ and $\frac{\partial u}{\partial y}$ compared to those for linear and quadratic finite elements and provides similar results (somewhere more accurate and somewhere less accurate) compared to those for cubic finite elements at the same number N of degrees of freedom. The fourth order of accuracy for OLTEM at mesh refinement in Fig. 18 will be studied in more detail in the future (we expected a lower order of convergence for $\frac{\partial u}{\partial x}$ and $\frac{\partial u}{\partial y}$ due to the use of numerical values of function u_i in Eq. (44)).

In order to study the convergence of the numerical results obtained by OLTEM in more detail, Fig. 16c presents curves 1 in Figs. 16a,b at small changes of the mesh size h (curves 1 and 2 in Fig. 16c correspond to curves 1 in Figs. 16a and 16b, respectively). For this study, we solve the test problem on 1001 Cartesian meshes with the mesh sizes $h_i = h_1 + \frac{(h_2 - h_1)(i-1)}{1000}$ with $h_1 = 0.1$, $h_2 = 0.02$ and $i = 1, 2, \ldots, 1001$. As can be seen from Fig. 16c, OLTEM shows convergent and stable results with small oscillations in the convergence curve at large h. At mesh refinement, these oscillations become smaller at small h. This oscillatory behavior can be explained by the complicated dependency of the leading terms of the local truncation error on the coefficients $d_{x,j}$ and $d_{y,j}$ $(1, 2, 3, 4, 5)$. It is important to mention that small oscillations in the numerical convergence curves are typical for many numerical techniques on domains with irregular interfaces at small variations of h. For example, the change in the angles of finite elements at small variations of the element size h also leads to such oscillations in the convergence curves for the finite element techniques.

5.5. Traveling waves in a 2-D bi-material plate with the circular interface

Let us consider wave propagation in a 2-D bi-material plate $ABCD$ consisting of an outer domain (domain Ω_I) and a circular inner domain centered at $O(0.5, 0.5)$ with radius $r = 0.25$ (domain Ω_{II}) with the circular interface; see Fig. 19a. For the circular interface the components of the unit normal used in the interface conditions are different for different interface points (they are calculated according to the geometry of the circular interface). The wave velocities are selected to be $c_I = 2/\sqrt{5}$ for domain Ω_I and $c_{II} = 1/\sqrt{5}$ for domain Ω_{II}; the coefficients e_I and e_{II} in the interface conditions are selected to be $e_I = 4/5$ for domain Ω_I and $e_{II} = 1/5$ for domain Ω_{II}. The loading term in the wave equation is selected to be $f_I(x, y, t) = 1$ for Ω_I and $f_{II}(x, y, t) = 0$ for Ω_{II}. The following Dirichlet boundary conditions are applied: $u(y, t) = -cos(4\pi y)sin(5\pi t)$ along the edge AD, $u(y, t) = cos(4\pi y)sin(5\pi t)$ along the edge BC, $u(x, t) = sin(2\pi x - 5\pi t)$ along the edges AB and CD. The initial displacements $u(x, y, t = 0) = sin(2\pi x)cos(4\pi y)$ and velocities $v(x, y, t = 0) = -5\pi cos(2\pi x)cos(4\pi y)$ are imposed over the entire domain. The final observation time is chosen to be $T = 5$. For these loading term,

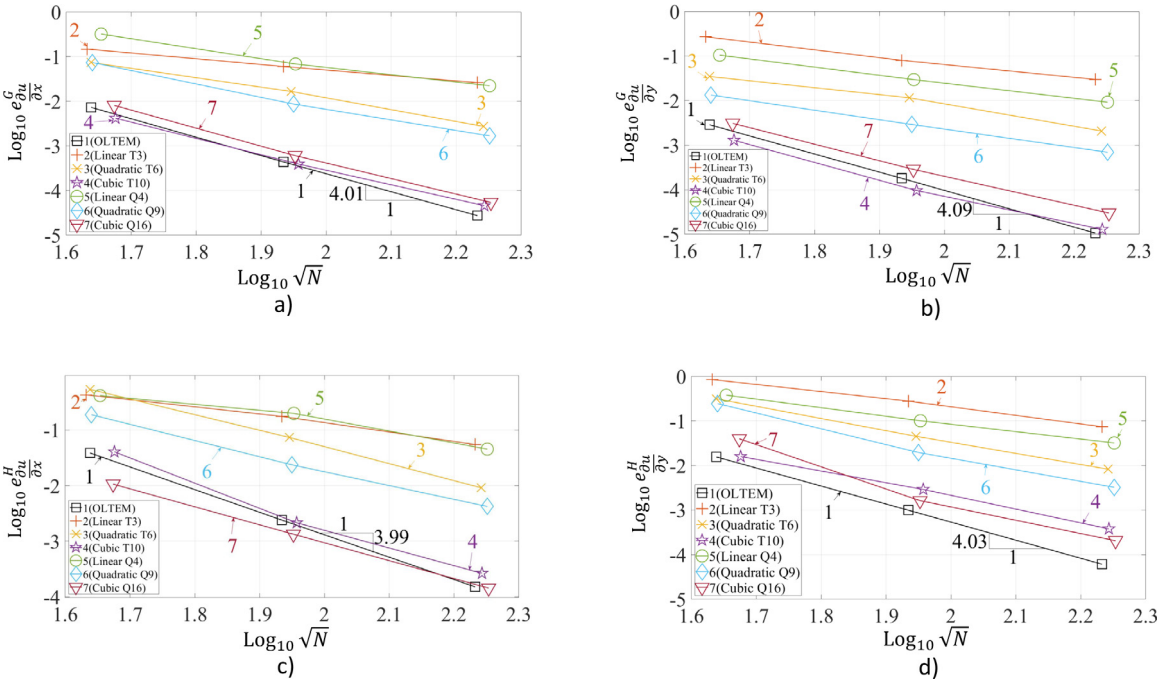

Fig. 18. The relative error in the x-derivative of the displacement $e_{\frac{\partial u}{\partial x}}$ (a, c) and in the y-derivative of the displacement $e_{\frac{\partial u}{\partial y}}$ (b, d) as a function of $\sqrt{N}$ in the logarithmic scale at mesh refinement at point $G(0.7, 1.5)$ (a, b) and at point $H(0.6, 1.6)$ (c, d) (see Fig. 14a); N is the number of degrees of freedom. The numerical solutions of the 2-D wave equation are obtained by OLTEM (curve 1) on square ($b_y = 1$) Cartesian meshes and by linear (curves 2, 5) and high-order finite elements (curves 3, 4, 6, 7). The Cartesian meshes of size $h = 1/30,\ 1/60,\ 1/120$ are used for OLTEM. The slopes of the curves 2–7 at mesh refinement are 1.2, 2.6, 3.21, 1.63, 2.32, 3.5 in (a); 1.43, 2.47, 3.01, 1.7, 2.06, 3.23 in (b); 1.67, 2.98, 3.14, 2.13, 2.42, 3.2 in (c) and 1.9, 2.43, 3.03, 1.65, 2.52, 3.02 in (d).

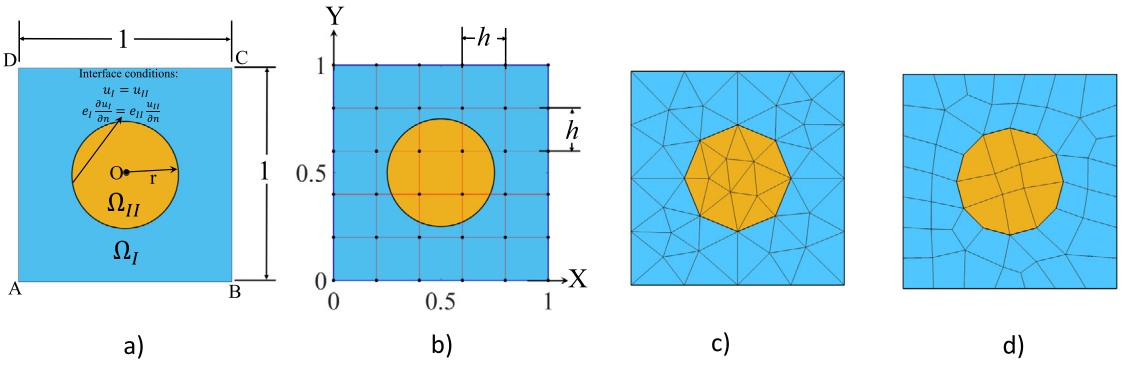

Fig. 19. A 2-D bi-material plate $ABCD$ with the circular interface centered at $O(0.5, 0.5)$ with a radius $r = 0.25$ (a). Examples of a Cartesian mesh used by OLTEM (b) as well as triangular (c) and quadrilateral (d) meshes for linear finite elements generated by the commercial software COMSOL.

boundary and initial conditions, the exact solution is unknown. Therefore, the numerical solution obtained by the 5th order finite elements on a triangular mesh with 679401 degrees of freedom is used as the reference solution for the error calculation. Fig. 20 shows the distribution of the displacement and the velocity of this reference solution at the time $T = 5$.

This problem is solved by linear, quadratic and cubic finite elements as well as by OLTEM. Fig. 19b,c,d shows examples of a Cartesian mesh used by OLTEM as well as triangular and quadrilateral finite element meshes generated by COMSOL.

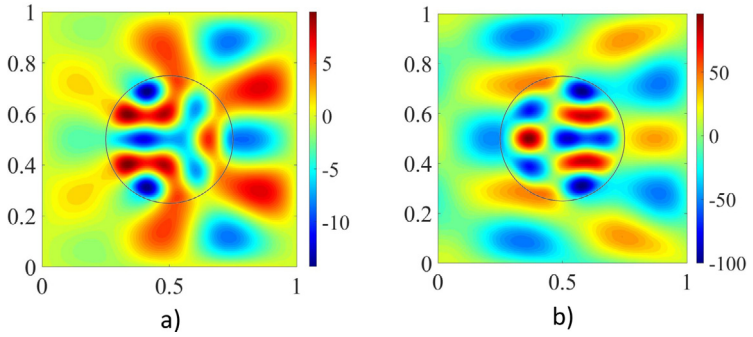

Fig. 20. The distributions of the displacement u (a) and the velocity v (b) of the reference solution for the plate with the circular interface; see Fig. 19a. The reference numerical solution of the 2-D wave equation at the time $T = 5$ is obtained by the 5th order finite elements on a triangular mesh with 679401 degrees of freedom.

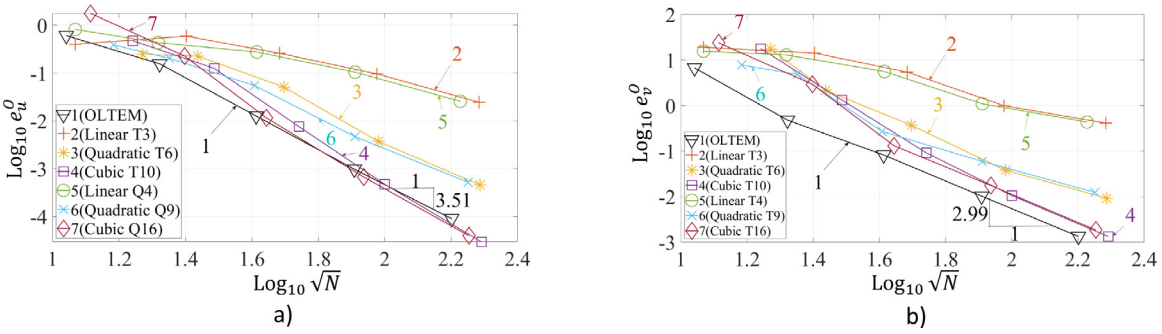

Fig. 21. The relative errors in displacement e_u^O (a) and in velocity e_v^O (b) at point $O(0.5, 0.5)$ as a function of $\sqrt{N}$ in the logarithmic scale at mesh refinement. N is the number of degrees of freedom. The numerical solutions of the 2-D wave equation for the 2-D plate with the circular interface (Fig. 19a) at the time $T = 5$ are obtained by OLTEM (curve 1) on uniform square ($b_y = 1$) Cartesian meshes and by linear (curves 2, 5), quadratic (curves 3, 6) and cubic (curves 4, 7) finite elements on triangular (curves 2–4) and quadrilateral (curves 5–7) meshes. The Cartesian meshes of size $h = 1/10, 1/20, 1/40, 1/80, 1/160$ are used for OLTEM. The slopes of the curves 2–7 at mesh refinement are 1.90, 2.95, 4.30, 1.94, 2.81, 3.84 in (a) and 2.13, 3.47, 3.07, 2.13, 3.55, 4.04 in (b).

In order to study the order of convergence of OLTEM and to compare the accuracy of the numerical solutions obtained by different techniques, we select point $O(0.5, 0.5)$ and plot the errors in displacement e_u^O and in velocities e_v^O at this point O; see Fig. 21 with the errors plotted in the logarithmic scale at mesh refinement. It can be seen from Fig. 21 that at the same number N of degrees of freedom, OLTEM yields more accurate results than linear, quadratic and cubic finite elements (the OLTEM results are close to those for cubic elements in the considered mesh size range: they are slightly more accurate for coarse meshes and are slightly less accurate for fine meshes). Similar results can be obtained at other points. It can be also seen from Fig. 21 that the order of convergence of OLTEM for the displacement and velocity exceeds three which is in agreement with the theoretical results in Section 4.

It can be concluded that for the 2-D wave equation with discontinuous coefficients, the developed OLTEM yields more accurate results than those obtained by linear and quadratic finite elements at the same numbers of degrees of freedom (it yields the results close to those for cubic finite elements with much wider stencils). It should be also mentioned that at the same number of degrees of freedom, high-order finite elements require greater computational costs compared to those for OLTEM due to a greater width of their stencil equations.

5.6. Heat transfer in a 2-D bi-material plate with the circular interface

Here, we consider heat transfer in the bi-material plate $ABCD$ shown in Fig. 19a and used in the previous Section 5.5. The thermal diffusivity of the plate are selected to be $a_I = 2/5$ for Ω_I and $a_{II} = 1/10$ for Ω_{II}; the coefficients e_I and e_{II} in the interface conditions are selected to be $e_I = 4/5$ for domain Ω_I and $e_{II} = 1/5$ for

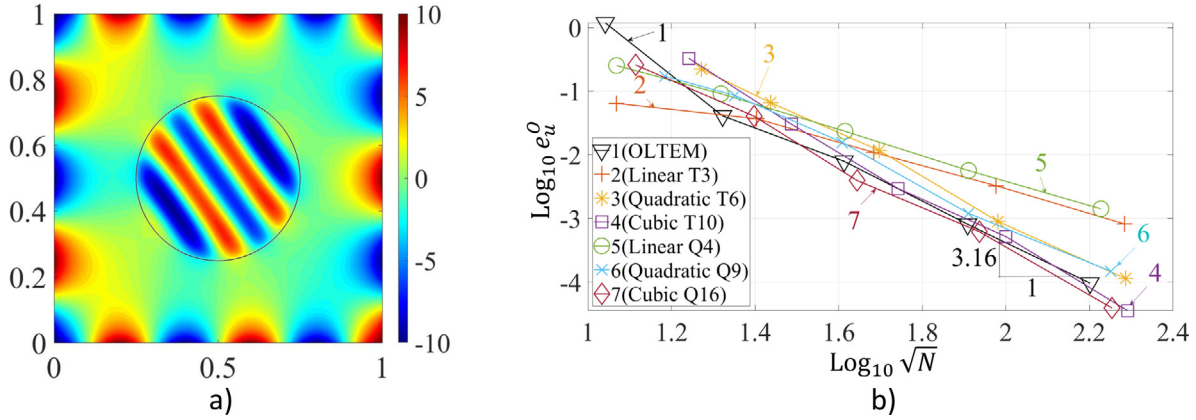

Fig. 22. The distribution of the temperature u of the reference solution obtained by the 5th order finite elements on a triangular mesh with 679401 degrees of freedom (a) as well as the relative error in temperature e_u^O at point $O(0.5, 0.5)$ as a function of $\sqrt{N}$ in the logarithmic scale at mesh refinement (b). N is the number of degrees of freedom. The numerical solutions of the 2-D heat equation for the 2-D plate (Fig. 19a) with the circular interface (b) at the time $T = 1$ are obtained by OLTEM (curve 1) on uniform square ($b_y = 1$) Cartesian meshes and by linear (curves 2, 5), quadratic (curves 3, 6) and cubic (curves 4, 7) finite elements on triangular (curves 2–4) and quadrilateral (curves 5–7) meshes. The Cartesian meshes of size $h = 1/10, 1/20, 1/40, 1/80, 1/160$ are used for OLTEM. The slopes of the curves 2–7 at mesh refinement are 2.01, 2.93, 4.00, 1.95, 2.68, 3.66.

domain Ω_{II}. The source term in the heat equation is selected to be $f_I(x, y, t) = 0$ for Ω_I and $f_{II}(x, y, t) = 20$ for Ω_{II}. The following Dirichlet boundary conditions are applied: $u(y, t) = 10cos(4\pi y)cos(3\pi t)$ along the edge AD, $u(y, t) = -10cos(4\pi y)cos(3\pi t)$ along the edge BC, $u(x, t) = 10cos(5\pi x)cos(3\pi t)$ along the edges AB and CD. The initial temperature $u(x, y, t = 0) = 10cos(5\pi x)cos(4\pi y)$ is imposed over the entire domain. The final observation time is chosen to be $T = 1$.

For these source term, boundary and initial conditions, the exact solution is unknown. Therefore, the numerical solution obtained by the 5th order finite elements on a triangular mesh with 679401 degrees of freedom is used as the reference solution for the error calculation. Fig. 22a shows the distribution of the temperature of this reference solution at the time $T = 5$.

This problem is solved by linear, quadratic and cubic finite elements as well as by OLTEM; see Fig. 19b,c,d for examples of a Cartesian mesh used by OLTEM as well as triangular and quadrilateral finite element meshes generated by COMSOL.

In order to study the order of convergence of OLTEM and to compare the accuracy of the numerical solutions obtained by different techniques, we select point $O(0.5, 0.5)$ and plot the error in temperature e_u^O; see Fig. 22b for the errors plotted in the logarithmic scale at mesh refinement. It can be seen from Fig. 22b that at the same number N of degrees of freedom, OLTEM yields more accurate results than linear, quadratic and cubic finite elements (the OLTEM results are close to those for cubic elements in the considered mesh size range: they are slightly more accurate for coarse meshes and are slightly less accurate for fine meshes). Similar results can be obtained at other points. It can be also seen from Fig. 22b that the order of convergence of OLTEM for the temperature exceeds three which is in agreement with the theoretical results in Section 4.

It can be concluded that for the 2-D heat equation with discontinuous coefficients, the developed OLTEM yields more accurate results than those obtained by linear and quadratic finite elements at the same numbers of degrees of freedom (it yields the results close to those for cubic finite elements with much wider stencils). It should be also mentioned that at the same number of degrees of freedom, high-order finite elements require greater computational costs compared to those for OLTEM due to a greater width of their stencil equations.

6. Concluding remarks

The new numerical approach developed in the paper is the extension of our approach for the wave and heat equations with constant coefficients (see [36–38]) to a much more general case of discontinuous coefficients. The main idea that allows this extension is the addition of the interface conditions at a number of the interface points

to the expression for the local truncation error. The unknown stencil coefficients can be analytically found in the 1-D case and in the 2-D case for horizontal (vertical) interfaces or can be numerically calculated from a small local system of algebraic equations for the general geometry of interfaces. This procedure does not change the width of the stencil equation; i.e., the size of the global system of equations is the same for the wave (heat) equation with constant or discontinuous coefficients. The calculation of the unknown stencil coefficients is based on the minimization of the local truncation error of the stencil equations and yields the optimal order of accuracy of the new technique at a given width of stencil equations. The increase in the computational costs for the calculation of the unknown stencil coefficients from the local system is insignificant compared to the computational costs for the time integration of the global semidiscrete system.

The main advantages of the suggested technique can be summarized as follows:

- Many difficulties of the existing numerical techniques for irregular domains (e.g., finite elements, spectral element, isogeometric elements, the finite volume method, and many other) are related to complicated mesh generators and the accuracy of 'bad' elements (e.g., the elements with small angles). In contrast to these techniques, OLTEM is based on trivial unfitted Cartesian meshes with a trivial procedure for the formation of the 9-point uniform and nonuniform stencils for 2-D domains with complex irregular interfaces.
- OLTEM has the same width of the stencil equations and the same structure of the global semidiscrete equations for the wave (heat) equations with the constant and discontinuous coefficients. There are no unknowns on the interfaces between different materials for the proposed technique; i.e., complex irregular interfaces do not affect the structure of the global system of equations (they affect just the values of the stencils coefficients).
- In contrast to the finite-difference techniques with the stencil coefficients calculated through the approximation of separate partial derivatives, the entire partial differential equation is used for the calculation of the stencil coefficients in OLTEM. This leads to the optimal accuracy of the proposed technique. For example, the 9-point uniform and nonuniform stencils of OLTEM in the 2-D case provide the optimal accuracy that cannot be improved without changing the width of stencil equations. In contrast to the 9-point stencils of linear quadrilateral finite elements, OLTEM yields a much higher order of accuracy (the increase by two orders for horizontal (vertical) interfaces and by one order for the general geometry of interfaces).
- The numerical results for domains with complex interfaces show that at the same number of degrees of freedom, OLTEM is even much more accurate than quadratic finite elements and yields the results close to those for cubic finite elements with much wider stencils. This also means that at a given accuracy, OLTEM significantly reduces the computation time compared to that for linear and high-order finite elements.
- OLTEM does not require time consuming numerical integration for finding the coefficients of the stencil equations; e.g., as for high-order finite, spectral and isogeometric elements. The stencil coefficients are calculated analytically or numerically (for the general geometry of interfaces) by the solution of small local systems of linear algebraic equations. Numerical experiments show that the solution of these small local systems of algebraic equations is fast. Moreover, these local systems are independent of each other and can be efficiently solved on a parallel computer.
- It has been shown that the wave and heat equations can be uniformly treated with OLTEM. The order of the time derivative in these equations does not affect the coefficients of the stencil equations of the semi-discrete systems because in the presented derivations the space discretization is considered independent of the time discretization without the interaction between the errors in space and time.
- Numerical examples (e.g., Section 5.2 for the impact problem) show that the numerical approach developed in the paper can be also applied to the problems with reduced regularity (smoothness) of the solutions within each subdomain with the same material properties.

In the future we plan to consider the stencils with a larger number of grid points for a higher order of accuracy (similar to high-order finite elements or to high-order finite-difference techniques) for problems with interfaces. For example, in our papers [15,16] we showed that on uniform meshes, OLTEM with 2-D 25-point stencils yields the $18-th$ order of accuracy for the Poisson equation with constant coefficients and the $8-th$ order of accuracy for the scalar wave (heat) equation with constant coefficients. Another direction is the development of OLTEM with adaptive refinement similar to $h-$ and $p-$ refinements for finite elements (e.g., in our papers [15,40] we showed that OLTEM can easily combine different stencils). We plan to use quadtrees/octrees meshes that allow a simple

refinement strategy with Cartesian meshes. The extension of OLTEM to other PDEs with discontinuous coefficients as well as to non-linear PDEs will be also considered in the future.

Declaration of competing interest

The authors declare that they have no known competing financial interests or personal relationships that could have appeared to influence the work reported in this paper.

Acknowledgments

The research of AI (theoretical developments) and BD (numerical study) has been supported in part by the NSF, USA grant CMMI-1935452, by the Army Research Office, USA (Grant Number W911NF-21-1-0267) and by Texas Tech University, USA. The views and conclusions contained in this paper are those of the authors and should not be interpreted as representing the official policies.

Appendix A. The coefficients b_p used in Eq. (18)

$b_1 = k_1 + q_1$
$b_2 = k_2 + k_3 - q_1$
$b_3 = e_* q_2 + k_1(\xi - 1)$
$b_4 = -e_{**} q_2 + k_2\xi + k_3\xi + k_3$
$b_5 = \bar{c}_*(m1 + q_3) + \frac{1}{2}k_1(\xi - 1)^2$
$b_6 = \frac{1}{2}(2\bar{c}_{**}(m2 + m\tilde{3} - q_3) + k_2\xi^2 + k_3(\xi + 1)^2)$
$b_7 = \bar{c}_* e_* q_4 + \bar{c}_* m1(\xi - 1) + \frac{1}{6}k_1(\xi - 1)^3$
$b_8 = \frac{1}{6}(6\bar{c}_{**}(-e_{**}q_4 + m2\xi + m3\xi + m3) + k_2\xi^3 + k_3(\xi + 1)^3)$
$b_9 = \frac{1}{24}(12\bar{c}_*(2\bar{c}_* q_5 + m1(\xi - 1)^2) + k_1(\xi - 1)^4)$
$b_{10} = \frac{1}{24}(-24\bar{c}_{**}^2 q_5 + 12\bar{c}_{**}(m2\xi^2 + m3(\xi + 1)^2) + k_2\xi^4 + k_3(\xi + 1)^4)$
$b_{11} = \frac{1}{6}\bar{c}_* m1(\xi - 1)^3 + \frac{1}{120}k_1(\xi - 1)^5$
$b_{12} = \frac{1}{120}(20\bar{c}_{**}m2\xi^3 + 20\bar{c}_{**}m3(\xi + 1)^3 + k_2\xi^5 + k_3(\xi + 1)^5)$
$b_{13} = \frac{1}{720}(\xi - 1)^4(30\bar{c}_* m1 + k_1(\xi - 1)^2)$
$b_{14} = \frac{1}{720}(30\bar{c}_{**}m2\xi^4 + 30\bar{c}_{**}m3(\xi + 1)^4 + k_2\xi^6 + k_3(\xi + 1)^6)$

Appendix B. The coefficients b_p used in Eq. (32)

The first ten coefficients b_i $(i = 1, 2, \ldots, 10)$ are presented below. All coefficients b_i $(i = 1, 2, \ldots, 56)$ used in the paper are given in the attached files 'b-coeff.pdf' and 'b-coeff.nb'.

$b_1 = a_1k_1 + a_2k_2 + a_3k_3 + a_4k_4 + a_5k_5 + a_6k_6 + a_7k_7 + a_8k_8 + a_9k_9 + q_{1,1} + q_{1,2} + q_{1,3} + q_{1,4} + q_{1,5}$

$b_2 = -a_1k_1 - a_2k_2 - a_3k_3 - a_4k_4 - a_5k_5 - a_6k_6 - a_7k_7 - a_8k_8 - a_9k_9 + k_1 + k_2 + k_3 + k_4 + k_5 + k_6 + k_7 + k_8 + k_9 - q_{1,1} - q_{1,2} - q_{1,3} - q_{1,4} - q_{1,5}$

$b_3 = -a_1k_1(d_1 + dx_G) - dx_G(a_2k_2 + a_3k_3 + a_4k_4 + a_5k_5 + a_6k_6 + a_7k_7 + a_8k_8 + a_9k_9) + a_3d_3k_3 - a_4d_4k_4 + a_6d_6k_6 - a_7d_7k_7 + a_9d_9k_9 + d_{x,1}q_{1,1} + d_{x,2}q_{1,2} + d_{x,4}q_{1,4} + d_{x,5}q_{1,5} + e_*(n_{x,1}q_{2,1} + n_{x,2}q_{2,2} + n_{x,3}q_{2,3} + n_{x,4}q_{2,4} + n_{x,5}q_{2,5})$

$b_4 = dx_G((a_1 - 1)k_1 + (a_2 - 1)k_2 + (a_3 - 1)k_3 + (a_4 - 1)k_4 + (a_5 - 1)k_5 + (a_6 - 1)k_6 + (a_7 - 1)k_7 + (a_8 - 1)k_8 + (a_9 - 1)k_9) + (a_1 - 1)d_1k_1 - (a_3 - 1)d_3k_3 + (a_4 - 1)d_4k_4 - (a_6 - 1)d_6k_6 + (a_7 - 1)d_7k_7 - (a_9 - 1)d_9k_9 - d_{x,1}q_{1,1} - d_{x,2}q_{1,2} - d_{x,4}q_{1,4} - d_{x,5}q_{1,5} - e_{**}(n_{x,1}q_{2,1} + n_{x,2}q_{2,2} + n_{x,3}q_{2,3} + n_{x,4}q_{2,4} + n_{x,5}q_{2,5})$

$b_5 = -a_1b_yk_1(d_1 + dy_G) - a_2b_yk_2(d_2 + dy_G) + b_y(-a_3k_3(d_3 + dy_G) - dy_G(a_4k_4 + a_5k_5 + a_6k_6 + a_7k_7 + a_8k_8 + a_9k_9) + a_7d_7k_7 + a_8d_8k_8 + a_9d_9k_9 + d_{1,2}q_{1,1} + d_{y,2}q_{1,2} + d_{y,4}q_{1,4} + d_{y,5}q_{1,5}) + e_*(n_{y,1}q_{2,1} + n_{y,2}q_{2,2} + n_{y,3}q_{2,3} + n_{y,4}q_{2,4} + n_{y,5}q_{2,5})$

$b_6 = b_y(dy_G((a_1 - 1)k_1 + (a_2 - 1)k_2 + (a_3 - 1)k_3 + (a_4 - 1)k_4 + (a_5 - 1)k_5 + (a_6 - 1)k_6 + (a_7 - 1)k_7 + (a_8 - 1)k_8 + (a_9 - 1)k_9) + (a_1 - 1)d_1k_1 + (a_2 - 1)d_2k_2 + (a_3 - 1)d_3k_3 - a_7d_7k_7 - a_8d_8k_8 - a_9d_9k_9 - d_{1,2}q_{1,1} - d_{y,2}q_{1,2} - d_{y,4}q_{1,4} - d_{y,5}q_{1,5} + d_7k_7 + d_8k_8 + d_9k_9) - e_{**}(n_{y,1}q_{2,1} + n_{y,2}q_{2,2} + n_{y,3}q_{2,3} + n_{y,4}q_{2,4} + n_{y,5}q_{2,5})$

$b_7 = \frac{1}{2}(2a_1\bar{c}_*m_1 + a_1k_1(d_1 + dx_G)^2 + 2a_2\bar{c}_*m_2 + a_2dx_G^2k_2 + 2a_3\bar{c}_*m_3 + a_3d_3^2k_3 - 2a_3d_3dx_Gk_3 + a_3dx_G^2k_3 + 2a_4\bar{c}_*m_4 + a_4d_4^2k_4 + 2a_4d_4dx_Gk_4 + a_4dx_G^2k_4 + 2a_5\bar{c}_*m_5 + a_5dx_G^2k_5 + 2a_6\bar{c}_*m_6 + a_6d_6^2k_6 - 2a_6d_6dx_Gk_6 + a_6dx_G^2k_6 + 2a_7\bar{c}_*m_7 + a_7d_7^2k_7 + 2a_7d_7dx_Gk_7 + a_7dx_G^2k_7 + 2a_8\bar{c}_*m_8 + a_8dx_G^2k_8 + 2a_9\bar{c}_*m_9 + a_9d_9^2k_9 - 2a_9d_9dx_Gk_9 + a_9dx_G^2k_9 + 2\bar{c}_*q_{3,2} + 2\bar{c}_*q_{3,3} + 2\bar{c}_*q_{3,4} + d_{x,1}^2q_{1,1} + 2d_{x,1}e_*n_{x,1}q_{2,1} + d_{x,2}^2q_{1,2} + 2d_{x,2}e_*n_{x,2}q_{2,2} + d_{x,4}^2q_{1,4} + 2d_{x,4}e_*n_{x,4}q_{2,4} + d_{x,5}^2q_{1,5} + 2d_{x,5}e_*n_{x,5}q_{2,5})$

$b_8 = \frac{1}{2}(-2\bar{c}_{**}(a_1m_1+(a_2-1)m_2+(a_3-1)m_3+(a_4-1)m_4+(a_5-1)m_5+(a_6-1)m_6+(a_7-1)m_7+(a_8-1)m_8+(a_9-1)m_9+q_{3,2}+q_{3,3}+q_{3,4})+dx_G^2(-a_1k_1-a_2k_2-a_3k_3-a_4k_4-a_5k_5-a_6k_6-a_7k_7-a_8k_8-a_9k_9+k_1+k_2+k_3+k_4+k_5+k_6+k_7+k_8+k_9)+d_1^2(k_1-a_1k_1)-2(a_1-1)d_1dx_Gk_1+2dx_G((a_3-1)d_3k_3-(a_4-1)d_4k_4+(a_6-1)d_6k_6-(a_7-1)d_7k_7+(a_9-1)d_9k_9)-(a_3-1)d_3^2k_3-(a_4-1)d_4^2k_4-(a_6-1)d_6^2k_6-(a_7-1)d_7^2k_7-(a_9-1)d_9^2k_9+2\bar{c}_{**}m_1-d_{x,1}^2q_{1,1}-2d_{x,1}e_{**}n_{x,1}q_{2,1}-d_{x,2}^2q_{1,2}-2e_{**}(d_{x,2}n_{x,2}q_{2,2}+d_{x,4}n_{x,4}q_{2,4})-d_{x,4}^2q_{1,4}-d_{x,5}(d_{x,5}q_{1,5}+2e_{**}n_{x,5}q_{2,5}))$

$b_9 = a_1b_yk_1(d_1+dx_G)(d_1+dy_G)+a_2b_ydx_Gk_2(d_2+dy_G)-a_3b_yd_3^2k_3+a_3b_yd_3dx_Gk_3-a_3b_yd_3dy_Gk_3+a_3b_ydx_Gdy_Gk_3+a_4b_yd_4dy_Gk_4+a_4b_ydx_Gdy_Gk_4+a_5b_ydx_Gdy_Gk_5-a_6b_yd_6dy_Gk_6+a_6b_ydx_Gdy_Gk_6-a_7b_yd_7^2k_7-a_7b_yd_7dx_Gk_7+a_7b_yd_7dy_Gk_7+a_7b_ydx_Gdy_Gk_7-a_8b_yd_8dx_Gk_8+a_8b_ydx_Gdy_Gk_8+a_9b_yd_9^2k_9-a_9b_yd_9dx_Gk_9-a_9b_yd_9dy_Gk_9+a_9b_ydx_Gdy_Gk_9+b_yd_{x,1}d_{1,2}q_{1,1}+b_yd_{1,2}e_*n_{x,1}q_{2,1}+b_yd_{x,2}d_{y,2}q_{1,2}+b_yd_{y,2}e_*n_{x,2}q_{2,2}+b_yd_{x,4}d_{y,4}q_{1,4}+b_yd_{y,4}e_*n_{x,4}q_{2,4}+b_yd_{x,5}d_{y,5}q_{1,5}+b_yd_{y,5}e_*n_{x,5}q_{2,5}+d_{x,1}e_*n_{y,1}q_{2,1}+d_{x,2}e_*n_{y,2}q_{2,2}+d_{x,4}e_*n_{y,4}q_{2,4}+d_{x,5}e_*n_{y,5}q_{2,5}$

$b_{10} = -b_y(dx_G(dy_G((a_1-1)k_1+(a_2-1)k_2+(a_3-1)k_3+(a_4-1)k_4+(a_5-1)k_5+(a_6-1)k_6+(a_7-1)k_7+(a_8-1)k_8+(a_9-1)k_9)+(a_2-1)d_2k_2+(a_3-1)d_3k_3-a_7d_7k_7-a_8d_8k_8-a_9d_9k_9+d_7k_7+d_8k_8+d_9k_9)+(a_1-1)d_1^2k_1+(a_1-1)d_1k_1(dx_G+dy_G)+dy_G(d_3(k_3-a_3k_3)+(a_4-1)d_4k_4-(a_6-1)d_6k_6+(a_7-1)d_7k_7-(a_9-1)d_9k_9)+d_3^2(k_3-a_3k_3)-(a_7-1)d_7^2k_7+(a_9-1)d_9^2k_9+d_{x,1}d_{1,2}q_{1,1}+d_{1,2}e_{**}n_{x,1}q_{2,1}+d_{x,2}d_{y,2}q_{1,2}+d_{y,2}e_{**}n_{x,2}q_{2,2}+d_{x,4}d_{y,4}q_{1,4}+d_{y,4}e_{**}n_{x,4}q_{2,4}+d_{x,5}d_{y,5}q_{1,5}+d_{y,5}e_{**}n_{x,5}q_{2,5})-e_{**}(d_{x,1}n_{y,1}q_{2,1}+d_{x,2}n_{y,2}q_{2,2}+d_{x,4}n_{y,4}q_{2,4}+d_{x,5}n_{y,5}q_{2,5})$

Appendix C. The coefficients k_j, m_j ($j = 1, 2, \ldots, 9$) for the 9-point uniform stencil with the horizontal interface and the corresponding local truncation error

$k_1 = -\frac{b_ye_*((e_*+e_{**})b_y^4+\xi(e_*-e_{**})b_y^3+(e_*+e_{**})b_y^2-\xi(8\xi^2+1)(e_*-e_{**})b_y+2\xi^2(4\xi^2+1)(e_*-e_{**}))}{2xx}$,

$k_2 = \frac{b_ye_*((e_*+e_{**})b_y^4+\xi(e_*-e_{**})b_y^3-5(e_*+e_{**})b_y^2-\xi(8\xi^2-5)(e_*-e_{**})b_y+2\xi^2(4\xi^2-5)(e_*-e_{**}))}{xx}$,

$k_3 = -\frac{b_ye_*((e_*+e_{**})b_y^4+\xi(e_*-e_{**})b_y^3+(e_*+e_{**})b_y^2-\xi(8\xi^2+1)(e_*-e_{**})b_y+2\xi^2(4\xi^2+1)(e_*-e_{**}))}{2xx}$,

$k_4 = \frac{-5(e_*+e_{**})^2b_y^5+10\xi(e_*^2-e_{**}^2)b_y^4+((1-13\xi^2)e_*^2+2(\xi^2+1)e_{**}e_*+(11\xi^2+1)e_{**}^2)b_y^3-4\xi^3(3e_*^2+2e_{**}e_*-5e_{**}^2)b_y^2+\xi^2(e_*-e_{**})(8e_*\xi^2+e_*+(8\xi^2+3)e_{**})b_y-2\xi^3(4\xi^2-1)(e_*-e_{**})^2}{2xx}$,

$k_5 = 1$,

$k_6 = \frac{-5(e_*+e_{**})^2b_y^5+10\xi(e_*^2-e_{**}^2)b_y^4+((1-13\xi^2)e_*^2+2(\xi^2+1)e_{**}e_*+(11\xi^2+1)e_{**}^2)b_y^3-4\xi^3(3e_*^2+2e_{**}e_*-5e_{**}^2)b_y^2+\xi^2(e_*-e_{**})(8e_*\xi^2+e_*+(8\xi^2+3)e_{**})b_y-2\xi^3(4\xi^2-1)(e_*-e_{**})^2}{2xx}$,

$k_7 = \frac{1}{2xx}[-e_{**}(e_*+e_{**})b_y^5+\xi(3e_*^2-e_{**}e_*-2e_{**}^2)b_y^4-((17e_*^2-10e_{**}e_*-7e_{**}^2)\xi^2+e_{**}(e_*+e_{**}))b_y^3+\xi(e_*-e_{**})((28\xi^2-1)e_*-4\xi^2e_{**})b_y^2-\xi^2(e_*-e_{**})((24\xi^2-1)e_*+(3-16\xi^2)e_{**})b_y+2\xi^3(4\xi^2-1)(e_*-e_{**})^2]$,

$k_8 = \frac{1}{5xx}[e_{**}(e_*+e_{**})b_y^5+\xi(-3e_*^2+e_{**}e_*+2e_{**}^2)b_y^4+(\xi^2(17e_*^2-10e_{**}e_*-7e_{**}^2)-5e_{**}(e_*+e_{**}))b_y^3+(-4(7e_*^2-8e_{**}e_*+e_{**}^2)\xi^3-5e_*(e_*-e_{**})\xi)b_y^2+\xi^2(e_*-e_{**})((24\xi^2+5)e_*-(16\xi^2+15)e_{**})b_y-2\xi^3(4\xi^2+5)(e_*-e_{**})^2]$,

$k_9 = \frac{1}{2xx}[-e_{**}(e_*+e_{**})b_y^5+\xi(3e_*^2-e_{**}e_*-2e_{**}^2)b_y^4-((17e_*^2-10e_{**}e_*-7e_{**}^2)\xi^2+e_{**}(e_*+e_{**}))b_y^3+\xi(e_*-e_{**})((28\xi^2-1)e_*-4\xi^2e_{**})b_y^2-\xi^2(e_*-e_{**})((24\xi^2-1)e_*+(3-16\xi^2)e_{**})b_y+2\xi^3(4\xi^2-1)(e_*-e_{**})^2]$,

$m_1 = \frac{1}{4\bar{c}_*\bar{c}_{**}xx}[b_y(b_y-\xi)^2e_*(-\bar{c}_*(\bar{c}_*-\bar{c}_{**})e_{**}(e_*+e_{**})b_y^6+\xi e_*((e_{**}-e_*)\bar{c}_*^2+\bar{c}_{**}(5e_*+7e_{**})\bar{c}_*+4\bar{c}_{**}^2e_*)b_y^5+(e_*(-13e_*\xi^2+3e_{**}\xi^2+e_*+e_{**})\bar{c}_{**}^2+\bar{c}_*(e_{**}(e_*+e_{**})-\xi^2(6e_*^2+e_{**}e_*+3e_{**}^2))\bar{c}_{**}+\bar{c}_*^2\xi^2(e_*^2+2e_{**}e_*+9e_{**}^2))b_y^4+\xi(e_*((11\xi^2-3)e_*-(3\xi^2+1)e_{**})\bar{c}_{**}^2+\bar{c}_*((9\xi^2+1)e_*^2+(e_{**}-27\xi^2e_{**})e_*+2(5\xi^2+1)e_{**}^2)\bar{c}_{**}+2\bar{c}_*^2\xi^2e_{**}(e_{**}-e_*))b_y^3+\xi^2(e_*((7\xi^2+5)e_*-3(3e_{**}\xi^2+e_{**}))\bar{c}_{**}^2+\bar{c}_*((e_*-3e_{**})e_{**}-8\xi^2e_*(e_*-2e_{**}))\bar{c}_{**}-\bar{c}_*^2\xi^2(e_*^2-13e_{**}e_*+18e_{**}^2))b_y^2+\xi^3(e_*-e_{**})(-5(3\xi^2+1)e_*\bar{c}_{**}^2+\bar{c}_*(-12e_*\xi^2+e_*+4(6e_{**}\xi^2+e_{**}))\bar{c}_{**}+3\bar{c}_*^2\xi^2e_*)b_y+2\xi^4(e_*-e_{**})((3\xi^2+1)e_*\bar{c}_{**}^2+\bar{c}_*(8e_*\xi^2+e_*-2(4e_{**}\xi^2+e_{**}))\bar{c}_{**}+\bar{c}_*^2\xi^2(e_*-4e_{**})))]$,

$m_2 = \frac{1}{2\bar{c}_*\bar{c}_{**}xx}[b_ye_*(\bar{c}_*(\bar{c}_*-\bar{c}_{**})e_{**}(e_*+e_{**})b_y^8+\xi((e_*^2-3e_{**}e_*-2e_{**}^2)\bar{c}_*^2+\bar{c}_{**}(-5e_*^2-5e_{**}e_*+2e_{**}^2)\bar{c}_*-4\bar{c}_{**}^2e_*^2)b_y^7+(-((3e_*^2-e_{**}e_*+8e_{**}^2)\xi^2+e_{**}(e_*+e_{**}))\bar{c}_*^2+\bar{c}_{**}(2(8e_*^2+7e_{**}e_*+e_{**}^2)\xi^2+e_{**}(e_*+e_{**}))\bar{c}_*+3\bar{c}_{**}^2\xi^2e_*(7e_*-e_{**}))b_y^6+\xi(((3\xi^2-1)e_*^2+(5e_{**}\xi^2+e_{**})e_*+16\xi^2e_{**}^2)\bar{c}_*^2+\bar{c}_{**}((5-26\xi^2)e_*^2+3(6e_{**}\xi^2+e_{**})e_*-16\xi^2e_{**}^2)\bar{c}_*+\bar{c}_{**}^2\xi^2e_*(9e_{**}-41e_*))b_y^5+\xi^2((e_*^2+(2-19\xi^2)e_{**}e_*+(13\xi^2+9)e_{**}^2)\bar{c}_*^2+\bar{c}_{**}(-69e_*e_{**}\xi^2+2(16\xi^2-5)e_*^2+(23\xi^2-6)e_{**}^2)\bar{c}_*+28\bar{c}_{**}^2\xi^2e_*^2)b_y^4+\xi^3(((-5e_*^2+31e_{**}e_*-38e_{**}^2)\xi^2+2e_{**}(e_{**}-e_*))\bar{c}_*^2+\bar{c}_{**}((10-13\xi^2)e_*^2+(23\xi^2-14)e_{**}e_*+2(7\xi^2+2)e_{**}^2)\bar{c}_*+6\bar{c}_{**}^2\xi^2e_*(3e_*-5e_{**}))b_y^3+\xi^4(((5\xi^2-1)e_*^2+(13-9\xi^2)e_{**}e_*+2(5\xi^2-9)e_{**}^2)\bar{c}_*^2+\bar{c}_{**}(-8(4e_*^2-11e_{**}e_*+8e_{**}^2)\xi^2-3(e_*-3e_{**})e_{**})\bar{c}_*+\bar{c}_{**}^2\xi^2e_*(45e_{**}-43e_*))b_y^2+\xi^5(e_*-e_{**})(((\xi^2+3)e_*-16\xi^2e_{**})\bar{c}_*^2+\bar{c}_{**}((44\xi^2-15)e_*+4(3-14\xi^2)e_{**})\bar{c}_*+27\bar{c}_{**}^2\xi^2e_*)b_y-2\xi^6(e_*-e_{**})((\xi^2-1)(e_*-4e_{**})\bar{c}_*^2+\bar{c}_{**}(8e_*\xi^2-8e_{**}\xi^2-5e_*+2e_{**})\bar{c}_*+3\bar{c}_{**}^2\xi^2e_*))]$,

$m_3 = \frac{1}{4\bar{c}_*\bar{c}_{**}xx}[b_y(b_y-\xi)^2e_*(-\bar{c}_*(\bar{c}_*-\bar{c}_{**})e_{**}(e_*+e_{**})b_y^6+\xi e_*((e_{**}-e_*)\bar{c}_*^2+\bar{c}_{**}(5e_*+7e_{**})\bar{c}_*+4\bar{c}_{**}^2e_*)b_y^5+(e_*(-13e_*\xi^2+3e_{**}\xi^2+e_*+e_{**})\bar{c}_{**}^2+\bar{c}_*(e_{**}(e_*+e_{**})-\xi^2(6e_*^2+e_{**}e_*+3e_{**}^2))\bar{c}_{**}+\bar{c}_*^2\xi^2(e_*^2+2e_{**}e_*+9e_{**}^2))b_y^4+\xi(e_*((11\xi^2-3)e_*-(3\xi^2+1)e_{**})\bar{c}_{**}^2+\bar{c}_*((9\xi^2+1)e_*^2+(e_{**}-27\xi^2e_{**})e_*+2(5\xi^2+1)e_{**}^2)\bar{c}_{**}+2\bar{c}_*^2\xi^2e_{**}(e_{**}-e_*))b_y^3+\xi^2(e_*((7\xi^2+5)e_*-3(3e_{**}\xi^2+e_{**}))\bar{c}_{**}^2+\bar{c}_*((e_*-3e_{**})e_{**}-8\xi^2e_*(e_*-2e_{**}))\bar{c}_{**}-\bar{c}_*^2\xi^2(e_*^2-13e_{**}e_*+18e_{**}^2))b_y^2+$

$\xi^3(e_*-e_{**})(-5(3\xi^2+1)e_*\bar{c}_{**}^2+\bar{c}_*(-12e_*\xi^2+e_*+4(6e_{**}\xi^2+e_{**})\bar{c}_{**}+3\bar{c}_*^2\xi^2e_*)b_y+2\xi^4(e_*-e_{**})((3\xi^2+1)e_*\bar{c}_{**}^2+\bar{c}_*(8e_*\xi^2+e_*-2(4e_{**}\xi^2+e_{**}))\bar{c}_{**}+\bar{c}_*^2\xi^2(e_*-4e_{**})))]$,

$m_4 = \frac{1}{12\bar{c}_*\bar{c}_{**}xx}[4(\bar{c}_*-\bar{c}_{**})\bar{c}_{**}e_*e_{**}(e_*+e_{**})b_y^9-4\xi e_*(2e_*e_{**}\bar{c}_*^2+\bar{c}_{**}(e_*+e_{**})^2\bar{c}_*+\bar{c}_{**}^2(5e_*^2+2e_{**}e_*-e_{**}^2))b_y^8+(2(e_{**}^2(e_*+e_{**})-\xi^2e_*(4e_*^2-7e_{**}e_*+e_{**}^2))\bar{c}_*^2+\bar{c}_{**}e_*(e_*+e_{**})((31e_*-43e_{**})\xi^2+2e_{**})\bar{c}_*+\bar{c}_{**}^2\xi^2e_*(55e_*^2+10e_{**}e_*+27e_{**}^2))b_y^7+2\xi((e_*(7e_*^2+14e_{**}e_*-3e_{**}^2)\xi^2+2e_{**}(e_*^2+2e_{**}e_*+2e_{**}^2))\bar{c}_*^2+\bar{c}_{**}e_*(12e_*e_{**}\xi^2+(1-32\xi^2)e_*^2+(14\xi^2+1)e_{**}^2)\bar{c}_*-20\bar{c}_{**}^2\xi^2e_*(e_*-e_{**})^2)b_y^6+\xi^2(((13\xi^2+2)e_*^3+(9-84\xi^2)e_{**}e_*^2+(19\xi^2+10)e_{**}^2e_*-e_{**}^3)\bar{c}_*^2+\bar{c}_{**}e_*((30\xi^2-3)e_*^2-2(13\xi^2+2)e_{**}e_*+(136\xi^2-13)e_{**}^2)\bar{c}_*-\bar{c}_{**}^2\xi^2e_*(55e_*^2+58e_{**}e_*+47e_{**}^2))b_y^5+\xi^3(((3-34\xi^2)e_*^3+(28\xi^2+5)e_{**}e_*^2+(14\xi^2+5)e_{**}^2e_*-29e_{**}^3)\bar{c}_*^2+2\bar{c}_{**}e_*((22\xi^2+1)e_*^2+4(1-3\xi^2)e_{**}e_*-(46\xi^2+1)e_{**}^2)\bar{c}_*+2\bar{c}_{**}^2\xi^2e_*(85e_*^2-98e_{**}e_*+57e_{**}^2))b_y^4-\xi^4(((2\xi^2-3)e_*^3-(82\xi^2+15)e_{**}e_*^2+7(8\xi^2+3)e_{**}^2e_*+5e_{**}^3)\bar{c}_*^2+\bar{c}_{**}e_*((73\xi^2-2)e_*^2+2(11-82\xi^2)e_{**}e_*+(159\xi^2-28)e_{**}^2)\bar{c}_*+\bar{c}_{**}^2\xi^2e_*(135e_*^2-198e_{**}e_*+19e_{**}^2))b_y^3+\xi^5(((26\xi^2+7)e_*^3+(3-64\xi^2)e_{**}e_*^2+(26\xi^2-43)e_{**}^2e_*+37e_{**}^3)\bar{c}_*^2+2\bar{c}_{**}e_*((20\xi^2-3)e_*^2+(8-58\xi^2)e_{**}e_*+(60\xi^2-7)e_{**}^2)\bar{c}_*-4\bar{c}_{**}^2\xi^2e_*(15e_*^2-30e_{**}e_*+23e_{**}^2))b_y^2-\xi^6e_*(e_*-e_{**})((3e_*\xi^2+15e_{**}\xi^2-7e_*+17e_{**})\bar{c}_*^2-\bar{c}_{**}(12e_*\xi^2-54e_{**}\xi^2+e_*+9e_{**})\bar{c}_*+15\bar{c}_{**}^2\xi^2(5e_{**}-9e_*))b_y-2\xi^7(e_*-e_{**})(((3\xi^2-1)e_*^2-5(\xi^2-1)e_{**}e_*-6e_{**}^2)\bar{c}_*^2+\bar{c}_{**}e_*((8\xi^2-1)e_*+(3-22\xi^2)e_{**})\bar{c}_*+\bar{c}_{**}^2\xi^2e_*(25e_*-9e_{**}))]$,

$m_5 = \frac{1}{6\bar{c}_*\bar{c}_{**}xx}[-4(\bar{c}_*-\bar{c}_{**})\bar{c}_{**}e_*e_{**}(e_*+e_{**})b_y^9+4\xi e_*(2e_*e_{**}\bar{c}_*^2+\bar{c}_{**}(e_*+e_{**})^2\bar{c}_*+\bar{c}_{**}^2(5e_*^2+2e_{**}e_*-e_{**}^2))b_y^8+((2e_*(4e_*^2-7e_{**}e_*+e_{**}^2)\xi^2+e_{**}(3e_*^2+16e_{**}e_*+13e_{**}^2))\bar{c}_*^2-\bar{c}_{**}e_*(\xi^2(31e_*-43e_{**})-22e_{**})(e_*+e_{**})\bar{c}_*+\bar{c}_{**}^2e_*((15-55\xi^2)e_*^2-2(5\xi^2-9)e_{**}e_*+3(1-9\xi^2)e_{**}^2))b_y^7+\xi(((3-14\xi^2)e_*^3+(23-28\xi^2)e_{**}e_*^2+(6\xi^2+37)e_{**}^2e_*+37e_{**}^3)\bar{c}_*^2+2\bar{c}_{**}e_*((32\xi^2+5)e_*^2-12(\xi^2+1)e_{**}e_*+(5-14\xi^2)e_{**}^2)\bar{c}_*+4\bar{c}_{**}^2e_*(5(2\xi^2-3)e_*^2-4(5\xi^2+3)e_{**}e_*+(10\xi^2-3)e_{**}^2))b_y^6+\xi^2(((10-13\xi^2)e_*^3+6(14\xi^2+5)e_{**}e_*^2+(20-19\xi^2)e_{**}^2e_*-32e_{**}^3)\bar{c}_*^2-\bar{c}_{**}e_*(15(2\xi^2+1)e_*^2+(8-26\xi^2)e_{**}e_*+(136\xi^2+125)e_{**}^2)\bar{c}_*+\bar{c}_{**}^2e_*(5(11\xi^2+21)e_*^2+2(29\xi^2+3)e_{**}e_*+(47\xi^2+9)e_{**}^2))b_y^5+2\xi^3(((17\xi^2+6)e_*^3-14(\xi^2-1)e_{**}e_*^2+(2-7\xi^2)e_{**}^2e_*-62e_{**}^3)\bar{c}_*^2+\bar{c}_{**}e_*((5-22\xi^2)e_*^2+4(3\xi^2+8)e_{**}e_*+(46\xi^2+7)e_{**}^2)\bar{c}_*+\bar{c}_{**}^2e_*(-5(17\xi^2+9)e_*^2+2(49\xi^2+15)e_{**}e_*+3(5-19\xi^2)e_{**}^2))b_y^4+\xi^4((2(\xi^2+9)e_*^3+(45-82\xi^2)e_{**}e_*^2+2(28\xi^2-51)e_{**}^2e_*+35e_{**}^3)\bar{c}_*^2+\bar{c}_{**}e_*((73\xi^2+10)e_*^2-2(82\xi^2+85)e_{**}e_*+(159\xi^2+224)e_{**}^2)\bar{c}_*+\bar{c}_{**}^2e_*(15(9\xi^2-1)e_*^2-6(33\xi^2-5)e_{**}e_*+(19\xi^2-75)e_{**}^2))b_y^3+\xi^5(((29-26\xi^2)e_*^3+(64\xi^2-27)e_{**}e_*^2-(26\xi^2+113)e_{**}^2e_*+131e_{**}^3)\bar{c}_*^2-2\bar{c}_{**}e_*(5(4\xi^2+3)e_*^2-2(29\xi^2+26)e_{**}e_*+(60\xi^2+59)e_{**}^2)\bar{c}_*+4\bar{c}_{**}^2e_*(15(\xi^2+2)e_*^2-6(5\xi^2+7)e_{**}e_*+(23\xi^2+18)e_{**}^2))b_y^2+\xi^6(e_*-e_{**})(((3\xi^2+20)e_*^2+(15\xi^2-58)e_{**}e_*+24e_{**}^2)\bar{c}_*^2+\bar{c}_{**}e_*((5-12\xi^2)e_*+27(2\xi^2+3)e_{**})\bar{c}_*+3\bar{c}_{**}^2e_*((25\xi^2+11)e_{**}-5(9\xi^2+7)e_*))b_y+2\xi^7(e_*-e_{**})(((3\xi^2+2)e_*^2-5(\xi^2+2)e_{**}e_*+18e_{**}^2)\bar{c}_*^2+\bar{c}_{**}e_*((8\xi^2+5)e_*-(22\xi^2+27)e_{**})\bar{c}_*+\bar{c}_{**}^2e_*(5(5\xi^2+3)e_*-3(3e_{**}\xi^2+e_{**})))]$,

$m_6 = \frac{1}{12\bar{c}_*\bar{c}_{**}xx}[4(\bar{c}_*-\bar{c}_{**})\bar{c}_{**}e_*e_{**}(e_*+e_{**})b_y^9-4\xi e_*(2e_*e_{**}\bar{c}_*^2+\bar{c}_{**}(e_*+e_{**})^2\bar{c}_*+\bar{c}_{**}^2(5e_*^2+2e_{**}e_*-e_{**}^2))b_y^8+(2(e_{**}^2(e_*+e_{**})-\xi^2e_*(4e_*^2-7e_{**}e_*+e_{**}^2))\bar{c}_*^2+\bar{c}_{**}e_*(e_*+e_{**})((31e_*-43e_{**})\xi^2+2e_{**})\bar{c}_*+\bar{c}_{**}^2\xi^2e_*(55e_*^2+10e_{**}e_*+27e_{**}^2))b_y^7+2\xi((e_*(7e_*^2+14e_{**}e_*-3e_{**}^2)\xi^2+2e_{**}(e_*^2+2e_{**}e_*+2e_{**}^2))\bar{c}_*^2+\bar{c}_{**}e_*(12e_*e_{**}\xi^2+(1-32\xi^2)e_*^2+(14\xi^2+1)e_{**}^2)\bar{c}_*-20\bar{c}_{**}^2\xi^2e_*(e_*-e_{**})^2)b_y^6+\xi^2(((13\xi^2+2)e_*^3+(9-84\xi^2)e_{**}e_*^2+(19\xi^2+10)e_{**}^2e_*-e_{**}^3)\bar{c}_*^2+\bar{c}_{**}e_*((30\xi^2-3)e_*^2-2(13\xi^2+2)e_{**}e_*+(136\xi^2-13)e_{**}^2)\bar{c}_*-\bar{c}_{**}^2\xi^2e_*(55e_*^2+58e_{**}e_*+47e_{**}^2))b_y^5+\xi^3(((3-34\xi^2)e_*^3+(28\xi^2+5)e_{**}e_*^2+(14\xi^2+5)e_{**}^2e_*-29e_{**}^3)\bar{c}_*^2+2\bar{c}_{**}e_*((22\xi^2+1)e_*^2+4(1-3\xi^2)e_{**}e_*-(46\xi^2+1)e_{**}^2)\bar{c}_*+2\bar{c}_{**}^2\xi^2e_*(85e_*^2-98e_{**}e_*+57e_{**}^2))b_y^4-\xi^4(((2\xi^2-3)e_*^3-(82\xi^2+15)e_{**}e_*^2+7(8\xi^2+3)e_{**}^2e_*+5e_{**}^3)\bar{c}_*^2+\bar{c}_{**}e_*((73\xi^2-2)e_*^2+2(11-82\xi^2)e_{**}e_*+(159\xi^2-28)e_{**}^2)\bar{c}_*+\bar{c}_{**}^2\xi^2e_*(135e_*^2-198e_{**}e_*+19e_{**}^2))b_y^3+\xi^5(((26\xi^2+7)e_*^3+(3-64\xi^2)e_{**}e_*^2+(26\xi^2-43)e_{**}^2e_*+37e_{**}^3)\bar{c}_*^2+2\bar{c}_{**}e_*((20\xi^2-3)e_*^2+(8-58\xi^2)e_{**}e_*+(60\xi^2-7)e_{**}^2)\bar{c}_*-4\bar{c}_{**}^2\xi^2e_*(15e_*^2-30e_{**}e_*+23e_{**}^2))b_y^2-\xi^6e_*(e_*-e_{**})((3e_*\xi^2+15e_{**}\xi^2-7e_*+17e_{**})\bar{c}_*^2-\bar{c}_{**}(12e_*\xi^2-54e_{**}\xi^2+e_*+9e_{**})\bar{c}_*+15\bar{c}_{**}^2\xi^2(5e_{**}-9e_*))b_y-2\xi^7(e_*-e_{**})(((3\xi^2-1)e_*^2-5(\xi^2-1)e_{**}e_*-6e_{**}^2)\bar{c}_*^2+\bar{c}_{**}e_*((8\xi^2-1)e_*+(3-22\xi^2)e_{**})\bar{c}_*+\bar{c}_{**}^2\xi^2e_*(25e_*-9e_{**}))]$,

$m_7 = -\frac{1}{12\bar{c}_*\bar{c}_{**}xx}[(b_y-\xi)((\bar{c}_*-\bar{c}_{**})\bar{c}_{**}e_*e_{**}(e_*+e_{**})b_y^8+\xi e_*(4e_*e_{**}\bar{c}_*^2+\bar{c}_{**}(5e_*^2+2e_{**}e_*+3e_{**}^2)\bar{c}_*-\bar{c}_{**}^2(5e_*^2+6e_{**}e_*+3e_{**}^2))b_y^7+((\xi^2e_*(4e_*^2-9e_{**}e_*+7e_{**}^2)-e_{**}^2(e_*+e_{**}))\bar{c}_*^2-\bar{c}_{**}e_*(2(9e_*^2+2e_{**}e_*+8e_{**}^2)\xi^2+e_{**}(e_*+e_{**}))\bar{c}_*+\bar{c}_{**}^2\xi^2e_*(-10e_*^2-11e_{**}e_*+9e_{**}^2))b_y^6+\xi(-(e_*(9e_*^2+2e_{**}e_*-e_{**}^2)\xi^2+2e_{**}(e_*^2+e_{**}e_*+e_{**}^2))\bar{c}_*^2+\bar{c}_{**}e_*((32\xi^2-1)e_*^2+(2-22\xi^2)e_{**}e_*+(1-36\xi^2)e_{**}^2)\bar{c}_*+\bar{c}_{**}^2\xi^2e_*(55e_*^2+36e_{**}e_*+17e_{**}^2))b_y^5-\xi^2(((2\xi^2+1)e_*^3+(2-46\xi^2)e_{**}e_*^2+(34\xi^2+1)e_{**}^2e_*-6e_{**}^3)\bar{c}_*^2+\bar{c}_{**}e_*((22\xi^2-2)e_*^2+(2-9\xi^2)e_{**}e_*-(61\xi^2+6)e_{**}^2)\bar{c}_*+\bar{c}_{**}^2\xi^2e_*(90e_*^2-53e_{**}e_*+45e_{**}^2))b_y^4+\xi^3(((18\xi^2-1)e_*^3-52\xi^2e_{**}e_*^2+(16\xi^2+1)e_{**}^2e_*+10e_{**}^3)\bar{c}_*^2-\bar{c}_{**}e_*(18e_*e_{**}\xi^2+(17\xi^2+2)e_*^2+(8-83\xi^2)e_{**}^2)\bar{c}_*+\bar{c}_{**}^2\xi^2e_*(65e_*^2-86e_{**}e_*-9e_{**}^2))b_y^3-\xi^4(((8\xi^2+1)e_*^3+3(7\xi^2+2)e_{**}e_*^2-(41\xi^2+16)e_{**}^2e_*+13e_{**}^3)\bar{c}_*^2+\bar{c}_{**}e_*(e_{**}(7e_{**}-11e_*)-2\xi^2(12e_*^2+19e_{**}e_*-53e_{**}^2))\bar{c}_*+\bar{c}_{**}^2\xi^2e_*(-50e_*^2+101e_{**}e_*-83e_{**}^2))b_y^2-\xi^5(e_*-e_{**})(((9\xi^2+3)e_*^2-(41\xi^2+3)e_{**}e_*-12e_{**}^2)\bar{c}_*^2+\bar{c}_{**}e_*((20\xi^2-3)e_*+(15-34\xi^2)e_{**})\bar{c}_*+23\bar{c}_{**}^2\xi^2e_*(5e_*-3e_{**}))b_y+2\xi^6(e_*-e_{**})(((3\xi^2-1)e_*^2-5(\xi^2-1)e_{**}e_*-6e_{**}^2)\bar{c}_*^2+\bar{c}_{**}e_*((8\xi^2-1)e_*+(3-22\xi^2)e_{**})\bar{c}_*+\bar{c}_{**}^2\xi^2e_*(25e_*-9e_{**}))]$,

$m_8 = \frac{1}{6\bar{c}_*\bar{c}_{**}xx}[(\bar{c}_*-\bar{c}_{**})\bar{c}_{**}e_*e_{**}(e_*+e_{**})b_y^9+\xi e_*(4e_*e_{**}\bar{c}_*^2+\bar{c}_{**}(5e_*^2+e_{**}e_*+2e_{**}^2)\bar{c}_*-\bar{c}_{**}^2(5e_*^2+5e_{**}e_*+2e_{**}^2))b_y^8+((e_*(4e_*^2-13e_{**}e_*+7e_{**}^2)\xi^2+2e_{**}^2(e_*+e_{**}))\bar{c}_*^2+\bar{c}_{**}e_*(5e_{**}(e_*+e_{**})-\xi^2(23e_*^2+6e_{**}e_*+19e_{**}^2))\bar{c}_*-\bar{c}_{**}^2e_*((5e_*^2+5e_{**}e_*-12e_{**}^2)\xi^2+3e_{**}(e_*+e_{**})))b_y^7+\xi((e_*(-13e_*^2+7e_{**}e_*-6e_{**}^2)\xi^2+4e_{**}(e_*^2+2e_{**}e_*+2e_{**}^2))\bar{c}_*^2+$

$\bar{c}_{**}e_*((50\xi^2+5)e_*^2-3(6\xi^2+5)e_{**}e_*-10(2\xi^2+1)e_{**}^2)\bar{c}_*+\bar{c}_{**}^2e_*(5(13\xi^2-3)e_*^2+(47\xi^2+3)e_{**}e_*+4(2\xi^2+3)e_{**}^2))b_y^6+\xi^2(((7\xi^2+2)e_*^3+3(16\xi^2+3)e_{**}e_*^2-(35\xi^2+2)e_{**}^2e_*-13e_{**}^3)\bar{c}_*^2+\bar{c}_{**}e_*(-3(18\xi^2+5)e_*^2+(31\xi^2+8)e_{**}e_*+(97\xi^2-37)e_{**}^2)\bar{c}_*-\bar{c}_{**}^2e_*(5(29\xi^2-15)e_*^2+(6-17\xi^2)e_{**}e_*+(62\xi^2+9)e_{**}^2))b_y^5+\xi^3(((20\xi^2+3)e_*^3-7(14e_{**}\xi^2+e_{**})e_*^2+5(10\xi^2+1)e_{**}^2e_*-41e_{**}^3)\bar{c}_*^2+\bar{c}_{**}e_*(5(\xi^2+4)e_*^2+(38-27\xi^2)e_{**}e_*+2(11\xi^2+47)e_{**}^2)\bar{c}_*+\bar{c}_{**}^2e_*(5(31\xi^2-36)e_*^2+(90-139\xi^2)e_{**}e_*+6(6\xi^2-5)e_{**}^2))b_y^4+\xi^4((e_*(-26e_*^2+31e_{**}e_*+25e_{**}^2)\xi^2+e_{**}(21e_*^2-24e_{**}e_*+55e_{**}^2))\bar{c}_*^2+\bar{c}_{**}e_*((41\xi^2-10)e_*^2+(56\xi^2-151)e_{**}e_*+(19-189\xi^2)e_{**}^2)\bar{c}_*+\bar{c}_{**}^2e_*(-15(\xi^2-18)e_*^2-15(\xi^2+17)e_{**}e_*+(92\xi^2+75)e_{**}^2))b_y^3-\xi^5(((\xi^2-7)e_*^3+(9-71\xi^2)e_{**}e_*^2+(82\xi^2+67)e_{**}^2e_*-49e_{**}^3)\bar{c}_*^2+\bar{c}_{**}e_*((44\xi^2+15)e_*^2-(16\xi^2+265)e_{**}e_*+2(103-36\xi^2)e_{**}^2)\bar{c}_*+\bar{c}_{**}^2e_*(15(11\xi^2+17)e_*^2-3(95\xi^2+101)e_{**}e_*+8(19\xi^2+9)e_{**}^2))b_y^2+\xi^6(e_*-e_{**})(((15\xi^2+4)e_*^2-(51\xi^2+38)e_{**}e_*+96e_{**}^2)\bar{c}_*^2+\bar{c}_{**}e_*((36\xi^2+25)e_*-3(26\xi^2+63)e_{**})\bar{c}_*+3\bar{c}_{**}^2e_*(5(11\xi^2+9)e_*-(29\xi^2+11)e_{**}))b_y-2\xi^7(e_*-e_{**})(((3\xi^2+2)e_*^2-5(\xi^2+2)e_{**}e_*+18e_{**}^2)\bar{c}_*^2+\bar{c}_{**}e_*((8\xi^2+5)e_*-(22\xi^2+27)e_{**})\bar{c}_*+\bar{c}_{**}^2e_*(5(5\xi^2+3)e_*-3(3e_{**}\xi^2+e_{**})))],$

$m_9 = -\frac{1}{12\bar{c}_*\bar{c}_{**}xx}[(b_y-\xi)((\bar{c}_*-\bar{c}_{**})\bar{c}_{**}e_*e_{**}(e_*+e_{**})b_y^8+\xi e_*(4e_*e_{**}\bar{c}_*^2+\bar{c}_{**}(5e_*^2+2e_{**}e_*+3e_{**}^2)\bar{c}_*-\bar{c}_{**}^2(5e_*^2+6e_{**}e_*+3e_{**}^2))b_y^7+((\xi^2e_*(4e_*^2-9e_{**}e_*+7e_{**}^2)-e_{**}^2(e_*+e_{**}))\bar{c}_*^2-\bar{c}_{**}e_*(2(9e_*^2+2e_{**}e_*+8e_{**}^2)\xi^2+e_{**}(e_*+e_{**}))\bar{c}_*+\bar{c}_{**}^2\xi^2e_*(-10e_*^2-11e_{**}e_*+9e_{**}^2))b_y^6+\xi(-(e_*(9e_*^2+2e_{**}e_*-e_{**}^2)\xi^2+2e_{**}(e_*^2+e_{**}e_*+e_{**}^2))\bar{c}_*^2+\bar{c}_{**}e_*((32\xi^2-1)e_*^2+(2-22\xi^2)e_{**}e_*+(1-36\xi^2)e_{**}^2)\bar{c}_*+\bar{c}_{**}^2\xi^2e_*(55e_*^2+36e_{**}e_*+17e_{**}^2))b_y^5-\xi^2(((2\xi^2+1)e_*^3+(2-46\xi^2)e_{**}e_*^2+(34\xi^2+1)e_{**}^2e_*-6e_{**}^3)\bar{c}_*^2+\bar{c}_{**}e_*((22\xi^2-2)e_*^2+(2-9\xi^2)e_{**}e_*-(61\xi^2+6)e_{**}^2)\bar{c}_*+\bar{c}_{**}^2\xi^2e_*(90e_*^2-53e_{**}e_*+45e_{**}^2))b_y^4+\xi^3(((18\xi^2-1)e_*^3-52\xi^2e_{**}e_*^2+(16\xi^2+1)e_{**}^2e_*+10e_{**}^3)\bar{c}_*^2-\bar{c}_{**}e_*(18e_*e_{**}\xi^2+(17\xi^2+2)e_*^2+(8-83\xi^2)e_{**}^2)\bar{c}_*+\bar{c}_{**}^2\xi^2e_*(65e_*^2-86e_{**}e_*-9e_{**}^2))b_y^3-\xi^4(((8\xi^2+1)e_*^3+3(7\xi^2+2)e_{**}e_*^2-(41\xi^2+16)e_{**}^2e_*+13e_{**}^3)\bar{c}_*^2+\bar{c}_{**}e_*(e_{**}(7e_{**}-11e_*)-2\xi^2(12e_*^2+19e_{**}e_*-53e_{**}^2))\bar{c}_*+\bar{c}_{**}^2\xi^2e_*(-50e_*^2+101e_{**}e_*-83e_{**}^2))b_y^2-\xi^5(e_*-e_{**})(((9\xi^2+3)e_*^2-(41\xi^2+3)e_{**}e_*-12e_{**}^2)\bar{c}_*^2+\bar{c}_{**}e_*((20\xi^2-3)e_*+(15-34\xi^2)e_{**})\bar{c}_*+23\bar{c}_{**}^2\xi^2e_*(5e_*-3e_{**}))b_y+2\xi^6(e_*-e_{**})(((3\xi^2-1)e_*^2-5(\xi^2-1)e_{**}e_*-6e_{**}^2)\bar{c}_*^2+\bar{c}_{**}e_*((8\xi^2-1)e_*+(3-22\xi^2)e_{**})\bar{c}_*+\bar{c}_{**}^2\xi^2e_*(25e_*-9e_{**})))],$

These coefficients provide the fifth order of the local truncation error in Eq. (32):

$e = \frac{\mathbf{h}^5}{480\bar{c}_*\bar{c}_{**}xx}[b_y(b_y-\xi)(-8\bar{c}_*e_*((e_*+e_{**})b_y^2+\xi(e_{**}-e_*)b_y+2\xi^2(e_*-e_{**}))((-5e_{**}\bar{c}_*^2+7\bar{c}_{**}e_{**}\bar{c}_*+2\bar{c}_{**}^2e_*)b_y^4+\xi(-5(e_*-e_{**})\bar{c}_*^2+\bar{c}_{**}(27e_*-7e_{**})\bar{c}_*-8\bar{c}_{**}^2e_*)b_y^3+3\xi^2(10e_{**}\bar{c}_*^2-\bar{c}_{**}(9e_*+7e_{**})\bar{c}_*+4\bar{c}_{**}^2e_*)b_y^2+\cdots]+O(\mathbf{h}^6)$

with

$xx = (5(e_*+e_{**})^2b_y^5-10\xi(e_*^2-e_{**}^2)b_y^4+((13\xi^2+5)e_*^2-2(\xi^2-5)e_{**}e_*+(5-11\xi^2)e_{**}^2)b_y^3+4\xi^3(3e_*^2+2e_{**}e_*-5e_{**}^2)b_y^2-\xi^2(e_*-e_{**})((8\xi^2-5)e_*+(8\xi^2-15)e_{**})b_y+2\xi^3(4\xi^2+5)(e_*-e_{**})^2)((\bar{c}_{**}e_*+\bar{c}_*e_{**})b_y^2+\xi(\bar{c}_*(e_*+e_{**})-2\bar{c}_{**}e_*)b_y+\xi^2(\bar{c}_{**}e_*+\bar{c}_*(e_*-2e_{**}))),$

Appendix D. The explicit expression for the term $\bar{f}_5$ in Eq. (38) in the case of nonzero loading (source) term $f_l \neq 0$ in the wave (heat) equation

The expression for $\bar{f}_5$ up to the fourth order with respect to $\boldsymbol{h}$ (see the attached files 'RHS.pdf' and 'RHS.nb' for more terms): $\bar{f}_5 = ((a_1m_1+a_2m_2+a_3m_3+a_4m_4+a_5m_5+a_6m_6+a_7m_7+a_8m_8+a_9m_9+q_{3,2}+q_{3,3}+q_{3,4})(f_G^*)+(-a_1m_1+m_1-a_2m_2+m_2-a_3m_3+m_3-a_4m_4+m_4-a_5m_5+m_5-a_6m_6+m_6-a_7m_7+m_7-a_8m_8+m_8-a_9m_9+m_9-q_{3,2}-q_{3,3}-q_{3,4})(f_G^{**}))\mathbf{h}^2$

$+((e_*n_{y,3}q_4-b_y(a_1(d_1+dy_G)m_1+a_2(d_2+dy_G)m_2+a_3d_3m_3-a_7d_7m_7-a_8d_8m_8-a_9d_9m_9+dy_G(a_3m_3+a_4m_4+a_5m_5+a_6m_6+a_7m_7+a_8m_8+a_9m_9)-d_{y,2}q_{3,2}-d_{y,4}q_{3,4}))(f_G^*)^{(0,1)}+(b_y((a_1-1)d_1m_1+(a_2-1)d_2m_2+(a_3-1)d_3m_3-a_7d_7m_7+d_7m_7-a_8d_8m_8+d_8m_8-a_9d_9m_9+d_9m_9+dy_G((a_1-1)m_1+(a_2-1)m_2+(a_3-1)m_3+(a_4-1)m_4+(a_5-1)m_5+(a_6-1)m_6+(a_7-1)m_7+(a_8-1)m_8+(a_9-1)m_9)-d_{y,2}q_{3,2}-d_{y,4}q_{3,4})-e_{**}n_{y,3}q_4)(f_G^{**})^{(0,1)}+(-a_1(d_1+dx_G)m_1+a_3d_3m_3-a_4d_4m_4+a_6d_6m_6-a_7d_7m_7+a_9d_9m_9-dx_G(a_2m_2+a_3m_3+a_4m_4+a_5m_5+a_6m_6+a_7m_7+a_8m_8+a_9m_9)+d_{x,2}q_{3,2}+d_{x,4}q_{3,4}+e_*n_{x,3}q_4)(f_G^*)^{(1,0)}+((a_1-1)d_1m_1-(a_3-1)d_3m_3+(a_4-1)d_4m_4-(a_6-1)d_6m_6+(a_7-1)d_7m_7-a_9d_9m_9+d_9m_9+dx_G((a_1-1)m_1+(a_2-1)m_2+(a_3-1)m_3+(a_4-1)m_4+(a_5-1)m_5+(a_6-1)m_6+(a_7-1)m_7+(a_8-1)m_8+(a_9-1)m_9)-d_{x,2}q_{3,2}-d_{x,4}q_{3,4}-e_{**}n_{x,3}q_4)(f_G^{**})^{(1,0)})\mathbf{h}^3$

$+\frac{1}{2}((a_1(d_1+dy_G)^2m_1b_y^2+a_2(d_2+dy_G)^2m_2b_y^2+(q_{3,2}d_{y,2}^2+a_3(d_3+dy_G)^2m_3+a_7d_7^2m_7+a_8d_8^2m_8+a_9d_9^2m_9+dy_G(dy_G(a_4m_4+a_5m_5+a_6m_6+a_7m_7+a_8m_8+a_9m_9)-2(a_7d_7m_7+a_8d_8m_8+a_9d_9m_9))+d_{y,4}^2q_{3,4})b_y^2+2\bar{c}_*q_5)(f_G^*)^{(0,2)}+2(-\frac{1}{2}((a_1-1)m_1d_1^2+2(a_1-1)dy_Gm_1d_1+(a_2-1)d_2^2m_2+(a_3-1)d_3^2m_3+(a_7-1)d_7^2m_7+(a_8-1)d_8^2m_8+(a_9-1)d_9^2m_9+dy_G(dy_G((a_1-1)m_1+(a_2-1)m_2+(a_3-1)m_3+(a_4-1)m_4+(a_5-1)m_5+(a_6-1)m_6+(a_7-1)m_7+(a_8-1)m_8+(a_9-1)m_9)+2((a_2-1)d_2m_2+(a_3-1)d_3m_3-a_7d_7m_7+d_7m_7-a_8d_8m_8+d_8m_8-a_9d_9m_9+d_9m_9))+d_{y,2}^2q_{3,2}+d_{y,4}^2q_{3,4})b_y^2-\bar{c}_{**}q_5)(f_G^{**})^{(0,2)}+2b_y(-a_3m_3d_3^2+a_3dx_Gm_3d_3-a_3dy_Gm_3d_3+a_1(d_1+dx_G)(d_1+dy_G)m_1+a_2dx_G(d_2+dy_G)m_2+a_3dx_Gdy_Gm_3+a_4d_4dy_Gm_4+a_4dx_Gdy_Gm_4+a_5dx_Gdy_Gm_5-a_6d_6dy_Gm_6+a_6dx_Gdy_Gm_6-a_7d_7^2m_7-a_7d_7dx_Gm_7+$

$a_7d_7dy_Gm_7+a_7dx_Gdy_Gm_7-a_8d_8dx_Gm_8+a_8dx_Gdy_Gm_8+a_9d_9^2m_9+a_9(dx_Gdy_G-d_9(dx_G+dy_G))m_9+d_{x,2}d_{y,2}q_{3,2}+d_{x,4}d_{y,4}q_{3,4})(f_G^*)^{(1,1)}-2b_y((a_1-1)m_1d_1^2+(a_1-1)(dx_G+dy_G)m_1d_1+d_3^2(m_3-a_3m_3)-(a_7-1)d_7^2m_7+(a_9-1)d_9^2m_9+dy_G(d_3(m_3-a_3m_3)+(a_4-1)d_4m_4-(a_6-1)d_6m_6+(a_7-1)d_7m_7-(a_9-1)d_9m_9)+dx_G((a_2-1)d_2m_2+(a_3-1)d_3m_3-a_7d_7m_7+d_7m_7-a_8d_8m_8+d_8m_8-a_9d_9m_9+d_9m_9+dy_G((a_1-1)m_1+(a_2-1)m_2+(a_3-1)m_3+(a_4-1)m_4+(a_5-1)m_5+(a_6-1)m_6+(a_7-1)m_7+(a_8-1)m_8+(a_9-1)m_9))+d_{x,2}d_{y,2}q_{3,2}+d_{x,4}d_{y,4}q_{3,4})(f_G^{**})^{(1,1)}+(q_{3,2}d_{x,2}^2+a_1(d_1+dx_G)^2m_1+a_3d_3^2m_3+a_4d_4^2m_4+a_6d_6^2m_6+a_7d_7^2m_7+a_9d_9^2m_9+dx_G(dx_G(a_2m_2+a_3m_3+a_4m_4+a_5m_5+a_6m_6+a_7m_7+a_8m_8+a_9m_9)-2(a_3d_3m_3-a_4d_4m_4+a_6d_6m_6-a_7d_7m_7+a_9d_9m_9))+d_{x,4}^2q_{3,4}+2\bar{c}_*q_5)(f_G^*)^{(2,0)}+((m_1-a_1m_1)d_1^2-2(a_1-1)dx_Gm_1d_1-(a_3-1)d_3^2m_3-(a_4-1)d_4^2m_4-(a_6-1)d_6^2m_6-(a_7-1)d_7^2m_7-(a_9-1)d_9^2m_9+dx_G^2(-a_1m_1+m_1-a_2m_2+m_2-a_3m_3+m_3-a_4m_4+m_4-a_5m_5+m_5-a_6m_6+m_6-a_7m_7+m_7-a_8m_8+m_8-a_9m_9+m_9)+2dx_G((a_3-1)d_3m_3-(a_4-1)d_4m_4+(a_6-1)d_6m_6-(a_7-1)d_7m_7+(a_9-1)d_9m_9)-d_{x,2}^2q_{3,2}-d_{x,4}^2q_{3,4}-2\bar{c}_{**}q_5)(f_G^{**})^{(2,0)})\mathbf{h}^4$
with $(f_G^*)^{(i,j)}=\frac{\partial^{i+j}f^*(x_G,y_G,t)}{\partial x^i\partial y^j}$ and $(f_G^{**})^{(i,j)}=\frac{\partial^{i+j}f^{**}(x_G,y_G,t)}{\partial x^i\partial y^j}$.

Appendix E. Supplementary data

Supplementary material related to this article can be found online at https://doi.org/10.1016/j.cma.2021.113998.

References

[1] H. Ahmadian, M. Friswell, J. Mottershead, Minimization of the discretization error in mass and stiffness formulations by an inverse method, Internat. J. Numer. Methods Engrg. 41 (2) (1998) 371–387.

[2] M.N. Guddati, B. Yue, Modified integration rules for reducing dispersion error in finite element method, Comput. Methods Appl. Mech. Engrg. 193 (2004) 275–287.

[3] V. Gyrya, K. Lipnikov, M-adaptation method for acoustic wave equation on square meshes, J. Comput. Acoust. 20 (2012) 1250022–1:23.

[4] K.J. Marfurt, Accuracy of finite difference and finite element modeling of the scalar and elastic wave equation, Geophysics 49 (1984) 533–549.

[5] R. Mullen, T. Belytschko, Dispersion analysis of finite element semidiscretizations of the two-dimensional wave equation, Internat. J. Numer. Methods Engrg. 18 (1982) 11–29.

[6] B. Yue, M.N. Guddati, Dispersion-reducing finite elements for transient acoustics, J. Acoust. Soc. Am. 118 (4) (2005) 2132–2141.

[7] Z.C. He, A.G. Cheng, G.Y. Zhang, Z.H. Zhong, G.R. Liu, Dispersion error reduction for acoustic problems using the edge-based smoothed finite element method (ES-FEM), Internat. J. Numer. Methods Engrg. 86 (11) (2011) 1322–1338.

[8] A.V. Idesman, D. Pham, Accurate finite element modeling of acoustic waves, Comput. Phys. Comm. 185 (2014) 2034–2045.

[9] M. Ainsworth, H.A. Wajid, Optimally blended spectral-finite element scheme for wave propagation and nonstandard reduced integration, SIAM J. Numer. Anal. 48 (1) (2010) 346–371.

[10] D. Wang, W. Liu, H. Zhang, Novel higher order mass matrices for isogeometric structural vibration analysis, Comput. Methods Appl. Mech. Engrg. 260 (2013) 92–108.

[11] D. Wang, W. Liu, H. Zhang, Superconvergent isogeometric free vibration analysis of Euler-Bernoulli beams and Kirchhoff plates with new higher order mass matrices, Comput. Methods Appl. Mech. Engrg. 286 (2015) 230–267.

[12] V. Puzyrev, Q. Deng, V. Calo, Dispersion-optimized quadrature rules for isogeometric analysis: Modified inner products, their dispersion properties, and optimally blended schemes, Comput. Methods Appl. Mech. Engrg. 320 (2017) 421–443.

[13] D. Wang, Q. Liang, J. Wu, A quadrature-based superconvergent isogeometric frequency analysis with macro-integration cells and quadratic splines, Comput. Methods Appl. Mech. Engrg. 320 (2017) 712–744.

[14] A. Idesman, B. Dey, The use of the local truncation error for the increase in accuracy of the linear finite elements for heat transfer problems, Comput. Methods Appl. Mech. Engrg. 319 (2017) 52–82.

[15] A. Idesman, B. Dey, New 25-point stencils with optimal accuracy for 2-D heat transfer problems. Comparison with the quadratic isogeometric elements, J. Comput. Phys. 418 (2020) 109640.

[16] A. Idesman, The use of the local truncation error to improve arbitrary-order finite elements for the linear wave and heat equations, Comput. Methods Appl. Mech. Engrg. 334 (2018) 268–312.

[17] R. Abedi, B. Petracovici, R.B. Haber, A space-time discontinuous Galerkin method for linearized elastodynamics with element-wise momentum balance, Comput. Methods Appl. Mech. Engrg. 195 (2006) 3247–3273.

[18] M. Dumbser, M. Kaeser, An arbitrary high-order discontinuous Galerkin method for elastic waves on unstructured meshes — II. The three-dimensional isotropic case, Geophys. J. Int. 167 (1) (2006) 319–336.

[19] S. Adjerid, M. Baccouch, The discontinuous Galerkin method for two-dimensional hyperbolic problems. Part I: Superconvergence error analysis, J. Sci. Comput. 33 (2007) 1573–7691.

[20] M. Baccouch, A local discontinuous Galerkin method for the second-order wave equation, Comput. Methods Appl. Mech. Engrg. 209–212 (2012) 129–143.

[21] M. Baccouch, A superconvergent local discontinuous Galerkin method for the second-order wave equation on Cartesian grids, Comput. Math. Appl. 68 (10) (2014) 1250–1278.

[22] M. Stanglmeier, N. Nguyen, J. Peraire, B. Cockburn, An explicit hybridizable discontinuous Galerkin method for the acoustic wave equation, Comput. Methods Appl. Mech. Engrg. 300 (2016) 748–769.

[23] P. Vos, R. van Loon, S. Sherwin, A comparison of fictitious domain methods appropriate for spectral/hp element discretisations, Comput. Methods Appl. Mech. Engrg. 197 (25–28) (2008) 2275–2289.
[24] E. Burman, P. Hansbo, Fictitious domain finite element methods using cut elements: I. A stabilized Lagrange multiplier method, Comput. Methods Appl. Mech. Engrg. 199 (41–44) (2010) 2680–2686.
[25] E. Rank, S. Kollmannsberger, C. Sorger, A. Duster, Shell Finite Cell Method: A high order fictitious domain approach for thin-walled structures, Comput. Methods Appl. Mech. Engrg. 200 (45–46) (2011) 3200–3209.
[26] E. Rank, M. Ruess, S. Kollmannsberger, D. Schillinger, A. Duster, Geometric modeling, isogeometric analysis and the finite cell method, Comput. Methods Appl. Mech. Engrg. 249–252 (2012) 104–115.
[27] S. May, M. Berger, An explicit implicit scheme for cut cells in embedded boundary meshes, J. Sci. Comput. 71 (3) (2017) 919–943.
[28] A. Main, G. Scovazzi, The shifted boundary method for embedded domain computations. Part I: Poisson and Stokes problems, J. Comput. Phys. (2017).
[29] T. Song, A. Main, G. Scovazzi, M. Ricchiuto, The shifted boundary method for hyperbolic systems: Embedded domain computations of linear waves and shallow water flows, J. Comput. Phys. 369 (2018) 45–79.
[30] H.-O. Kreisst, N.A. Petersson, An embedded boundary method for the wave equation with discontinuous coefficients, SIAM J. Sci. Comput. 28 (6) (2006) 2054–2074.
[31] H.-O. Kreiss, N.A. Petersson, A second order accurate embedded boundary method for the wave equation with Dirichlet data, SIAM J. Sci. Comput. 27 (4) (2006) 1141–1167.
[32] H.-O. Kreiss, N.A. Petersson, J. Ystrom, Difference approximations of the Neumann problem for the second order wave equation, SIAM J. Numer. Anal. 42 (3) (2004) 1292–1323.
[33] P. McCorquodale, P. Colella, H. Johansen, A cartesian grid embedded boundary method for the heat equation on irregular domains, J. Comput. Phys. 173 (2) (2001) 620–635.
[34] H. Johansen, P. Colella, A Cartesian grid embedded boundary method for Poisson's equation on irregular domains, J. Comput. Phys. 147 (1) (1998) 60–85.
[35] Q. Zhang, I. Babuska, A stable generalized finite element method (SGFEM) of degree two for interface problems, Comput. Methods Appl. Mech. Engrg. 363 (2020) 112889.
[36] A. Idesman, A new numerical approach to the solution of PDEs with optimal accuracy on irregular domains and cartesian meshes. Part 1: the derivations for the wave, heat and Poisson equations in the 1-D and 2-D cases, Arch. Appl. Mech. 90 (2020) 2621–2648.
[37] B. Dey, A. Idesman, A new numerical approach to the solution of PDEs with optimal accuracy on irregular domains and cartesian meshes. Part 2: numerical simulation and comparison with FEM, Arch. Appl. Mech. 90 (2020) 2649–2674.
[38] A. Idesman, B. Dey, A new 3-D numerical approach to the solution of PDEs with optimal accuracy on irregular domains and Cartesian meshes, Comput. Methods Appl. Mech. Engrg. 354 (2019) 568–592.
[39] A. Idesman, B. Dey, Compact high-order stencils with optimal accuracy for numerical solutions of 2-D time-independent elasticity equations, Comput. Methods Appl. Mech. Engrg. 360 (2020) 112699.
[40] A. Idesman, B. Dey, Accurate numerical solutions of 2-D elastodynamics problems using compact high-order stencils, Comput. Struct. 229 (2020) 106160.
[41] A. Idesman, B. Dey, A new numerical approach to the solution of the 2-D Helmholtz equation with optimal accuracy on irregular domains and Cartesian meshes, Comput. Mech. 65 (2020) 1189–1204.
[42] J.S. Sochacki, J.H. George, R.E. Ewing, S.B. Smithson, Interface conditions for acoustic and elastic wave propagation, Geophysics 56 (2) (1991) 168–181.
[43] C.-S. Chou, C. Shu, Y. Xing, Optimal energy conserving local discontinuous Galerkin methods for second-order wave equation in heterogeneous media, J. Comput. Phys. 272 (2014) 88–107.
[44] Y. Chai, K.-J. Bathe, Transient wave propagation in inhomogeneous media with enriched overlapping triangular elements, Comput. Struct. 237 (2020) 106273.
[45] A. Idesman, B. Dey, The treatment of the Neumann boundary conditions for a new numerical approach to the solution of PDEs with optimal accuracy on irregular domains and cartesian meshes, Comput. Methods Appl. Mech. Engrg. 365 (2020) 112985.
[46] K.J. Bathe, Finite Element Procedures, Prentice-Hall Inc., Upper Saddle River, New Jersey, 1996.
[47] H.P. Langtangen, S. Linge, Finite Difference Computing with PDES, Springer, 2017.
[48] A. Idesman, H. Samajder, E. Aulisa, P. Seshaiyer, Benchmark problems for wave propagation in elastic materials, Comput. Mech. 43 (6) (2009) 797–814.
[49] A. Idesman, Accurate time integration of linear elastodynamics problems, CMES Comput. Model. Eng. Sci. 71 (2) (2011) 111–148.
[50] A.V. Idesman, D. Pham, J. Foley, M. Schmidt, Accurate solutions of wave propagation problems under impact loading by the standard, spectral and isogeometric high-order finite elements. comparative study of accuracy of different space-discretization techniques, Finite Elem. Anal. Des. 88 (2014) 67–89.